Decoupling in the liquid crystals and solid state NMR of Fluorine containing organics

Antonioli, Gian Carlo

Decoupling in the Liquid Crystals and Solid State NMR of Fluorine Containing Organics

By

Gian Carlo Antonioli

Graduate Society

University of Durham

A thesis submitted in partial fulfilment of the requirements for the degree of Doctor of Philosophy

Department of Chemistry

University of Durham

2004

To my family

Abstract

The success of NMR methods in solids and liquid crystals is strongly related to more and more sophisticated strategies of spin decoupling. This is particularly true for liquid crystal samples where high resolved decoupled spectra are required. In the first part of this thesis we described the basic principles of spin decoupling and through numerical simulations based on appropriate spin modelling we provided new physical insight. Testing several decoupling schemes in fluorinated liquid crystals we found anomalous line broadenings of carbon resonances close to ^{19}F. The underlying mechanisms of these broadenings were successfully explained in terms of ^{1}H decoupling effects. We demonstrated that these broadening effects are related to the difficulty of ^{1}H decoupling in the presence of strong ^{1}H—^{19}F dipolar interactions. Employment of sophisticated decoupling methods drastically reduced or even fully eliminated the sources of these line-broadenings.

In the second part of this thesis we extended the preceding work to spinning samples (both liquid crystals and solids). Analogous line-broadenings from decoupling effects are also at work here. However additional line-broadening mechanisms, such as magic angle spinning misset and ^{19}F lifetime-broadening are also limiting factors of carbon linewidth.

Quantification and assignments of dipolar splittings are vital to understand complex molecular conformations of liquid crystalline phases. To extract this information from 1D NMR could be difficult. This difficulty arises from the complexity of 1D spectra, and so 2D NMR methods have been explored. In the last part of this work we designed Separated-Local-Field sequences, showing that this class of experiments are particularly suited to quantitative use of C—F splittings in fluorinated liquid crystals.

Contents

Chapter 1

Introduction to Nuclear Magnetic Resonance

1.1 Introduction

In 1946 nuclear magnetic resonance (NMR) in condensed matter was discovered simultaneously by Edward Purcell at Harvard and Felix Bloch at Stanford using different instrumentation and techniques. Since that time NMR has become the most important techniques for molecular structure determination. This is the case especially for Organic Chemistry where hydrogen and carbon are present in many environments and are easily detected and differentiated by NMR methods. Important applications of NMR regards studies of orientated materials, such as liquid crystals. NMR spectroscopy has proved to yield quite detailed information on the molecular ordering and dynamic in mesophase [1] of these oriented materials.

In what follows we will give a brief overview of basic principles of magnetic resonance, and also we shall try to illustrate some of the most important aspect of the technique relevant for this thesis.

1.2 Nuclear spin and nuclear magnetism

Many atomic nuclei posses in their ground quantum state a well-defined spin angular momentum [2-4] $\hbar I$, where $\hbar$ is Plank's constant and I a quantum number, which is integer or half integer. Because the atomic nuclei are charged particles these nuclei also have a dipolar magnetic moment, which gives rise to nuclear magnetism. The

nuclear spin and the magnetic moments are related by the equation: Equation Section 1

$$\vec{\mu} = \gamma \hbar \vec{I} \tag{1.1}$$

where γ is the gyromagnetic ratio.

1.3 Nuclear magnetic resonance phenomenon

The NMR signal is the voltage induced in a coil by the precession of the nuclear magnetization $\vec{M}$ around the direction of the static field $\vec{B}_0$. The precession motion, [5, 6] of such a magnetization $\vec{M}$ is described by:

$$\frac{d\vec{M}}{dt} = \vec{M} \wedge \vec{B}_0 \tag{1.2}$$

Where $\vec{M} = \sum_k \vec{\mu}_k$ and $\vec{\mu}_k$'s are the magnetic moments of each of the spins of the system (vector-model, [7]). The energy of the nuclear magnetization $\vec{M}$ in the magnetic field $\vec{B}_0$ is given by:

$$E = -\vec{B}_0 . \vec{M} = \left\| \vec{B}_0 \right\| \left\| \vec{M} \right\| \cos(\theta) \tag{1.3}$$

Since $\frac{\partial \vec{B}_0}{\partial t} = 0$, the energy E is a constant of the motion. As seen in Eq. (1.3) the energy E depends on the relative orientation between the magnetic field $\vec{B}_0$ and the magnetic moment $\vec{M}(t)$ (θ-angle). As a result precession of $\vec{M}$ must occur keeping constant the angle θ, which is determined by the initial condition $\vec{M}_0 = \vec{M}(0)$ in the linear differential equation (1.2). Outlining we can say that the motion of $\vec{M}(t)$ describes a conic surface. The precession rate of $\vec{M}(t)$ around the magnetic field $\vec{B}$

is called Larmor frequency and its expression is $\nu_L = \gamma B/2\pi$. Because the giromagnetic ratio γ is sign dependent, the Larmor frequency can be positive or negative. As a result the precession of $\vec{M}(t)$ around the magnetic field can be clock-wise or counter clock-wise according to the sign of γ. By applying an oscillating magnetic field, often denoted by the letter B_1, to the nuclear spin its energy becomes time dependent. Since the energy must be conserved, a continuous exchange of energy between the nuclear spin and the oscillating field B_1 takes place. When the frequency of B_1, say ν_1, is equal to the Larmor frequency ν_L this exchange of energy is maximum. This is the principle of nuclear magnetic resonance.

For a system of isolated spins the classical and quantum description of spin motion are equivalent, however this equivalence disappears for a system with interacting spins. Although the basic NMR phenomenon can be explained with a classical model, many NMR experiments, particularly in solids and liquid crystals, require a more complete quantum mechanical treatment. As a result we shall extend equation (1.2) for an isolated spin to a system of interacting spins.

1.4 Density operator

Consider an ensemble of spin systems (molecules) each of which evolves in time according to its Schrödinger's equation, [8, 9]; whence takes into account of possible interactions among the spins or even interactions between applied external fields and the spin system itself.

It is important to note that we are not interested in determining the quantum state of an individual spin system, but rather to general properties referring to the ensemble of systems. In other words we want to measure the expectation values of quantum observables averaged over the ensemble of spin systems. Given an observable A, its expectation value is given by:

$$\overline{\langle A \rangle} = \sum_{j=1}^{N} \frac{\langle A_j \rangle}{N} \tag{1.4}$$

The A_j observable is referring to the individual spin system, and N is the number of the systems. The quantum state of the *j-th* system is fully described by the wave function $\Psi^{(j)}$ if the internal energy of individual system is much greater than the energy between the systems (*pure quantum state*, [2]). As a result the expectation value of the observable A is given by:

$$\langle A_j \rangle = \left\langle \Psi^{(j)} \middle| A_j \middle| \Psi^{(j)} \right\rangle \tag{1.5}$$

At this point we can represent the wave function $\Psi^{(j)}$ in a basis set of Zeeman states $\{|\alpha_m\rangle\}_{m=1..P}$:

$$\Psi^{(j)} = \sum_{k=1}^{P} c_k^{(j)} |\alpha_k\rangle \tag{1.6}$$

As a result the expectation value of $\overline{\langle A \rangle}$ over the ensemble of the system is:

$$\overline{\langle A \rangle} = \frac{1}{N} \sum_{j=1}^{N} \sum_{m,n=1}^{P} \overline{c}_m^{(j)} c_n^{(j)} \langle \alpha_m | A | \alpha_n \rangle \tag{1.7}$$

Where $\overline{c}$ indicates the complex conjugation of the coefficient c. As it will be seen in Eq. (1.7) the matrix elements $\langle \alpha_m | A | \alpha_n \rangle$ of the operator A are completely independent from the wave functions $\Psi^{(j)}$. The expectation value $\overline{\langle A \rangle}$ is fully determined by the products $\overline{c}_m^{(j)} c_n^{(j)}$. This suggests that we can exploit those products to calculate any physical property of the ensemble of the system; in fact the Eq. (1.7) can be rewritten as follows:

$$\overline{\langle A \rangle} = \sum_{m,n=1}^{P} \rho_{m,n} \langle \alpha_m | A | \alpha_n \rangle = tr\{\rho A\} \tag{1.8}$$

Where the terms $\rho_{n,m}$ are the matrix elements of the so-called *density operator*. The operator $tr\{\ \}$ indicates the trace of an operator, which is the sum of their diagonal elements. The Eq. (1.8) implicitly defines the mathematical form of the elements of ρ:

$$\rho_{m,n} = \frac{1}{N}\sum_{j=1}^{N} \bar{c}_m^{(j)} c_n^{(j)} \quad \text{where} \quad m,n = 1.....P \tag{1.9}$$

From the Eq. (1.9) it is seen that the *density operator* is a hermitian operator, [10-12], by definition, and also that the $tr\{\rho\} = 1$, which is the normalization of the wave functions $\Psi^{(j)}$ (conservation of the probability).

It will be noticed that the density operator is represented in a Hilbert' space, [13], with dimensionality P, which is the dimension of the Hilbert' space associated with the individual system. This is a very powerful simplification of the problem because we avoid having to specify microscopic states $\Psi^{(j)}$ of $\sim 10^{22}$ spins we would in a full ensemble treatment.

1.5 Spin density matrix at thermal equilibrium

In a NMR experiment the nuclear spin system is embedded in an intense magnetic field $\vec{B}$ and furthermore it is in thermal contact with the lattice, with which occurs the exchange of energy indispensable to achieve the thermal equilibrium.

Such state of thermal equilibrium corresponds to a macroscopic magnetisation along the direction of the magnetic field $\vec{B}$. The process through which such a magnetisation is formed can be described by using quantum statistical mechanics approach.

The density matrix of following form describes the quantum state at thermal equilibrium:

$$\rho_{eq} = \frac{e^{-\frac{\hbar H_0}{k_B T}}}{\sum_m \langle n | e^{-\frac{\hbar H_0}{k_B T}} | n \rangle} \tag{1.10}$$

Where the summation on n-index is extended over all states of the spin system. The denominator of Eq. (1.10) often is called partition function, [14], and it is denoted by the letter Z. The symbol k_B is the Boltzmann's constant, while T is the equilibrium temperature between the spin system and the lattice.

By using the density matrix at thermal equilibrium we can calculate the expectation value of the magnetization along the magnetic field $\vec{B}$:

$$\langle M_Z \rangle = tr\{\rho_{eq} M_Z\} = \frac{1}{Z} tr\left\{ M_Z \left(\exp(-\frac{\hbar H_0}{k_B T}) \right) \right\} \tag{1.11}$$

In the high temperature approximation, the exponent $\|\hbar H_0\|/k_B T << 1$. As a result the density matrix ρ_{eq} can be approximated at first order as follows:

$$\rho_{eq} \approx \frac{I_{op} - \hbar H_0 / KT}{\tilde{Z}} \tag{1.12}$$

Where the term $\tilde{Z}$ is the partition function under high temperature approximation and I_{op} is the identity operator in the spin Hilbert space of the system. The corresponding $\langle M_Z \rangle$ expectation value becomes:

$$\langle M_Z \rangle \cong \frac{1}{\tilde{Z}} tr\left\{ \frac{\gamma^2 \hbar^2 B I_Z^2}{KT} \right\} = \frac{\gamma^2 \hbar^2 I(I+1)}{KT} B \tag{1.13}$$

In analogues way we can derive that the expectation value of $\langle M_X \rangle$ and $\langle M_Y \rangle$ are both zero.

In the Eq. (1.13) the term I is the spin quantum number, while γ is the giromagnetic ratio of nucleus. The spin Hamiltonian H_0 is assumed to be the Zeeman interaction $-\gamma B I_Z$, with I_Z the z-component of $\vec{I}$ spin-vector operator. Summarizing we can say that the density matrix of Eq. (1.13) describes the quantum state at thermal equilibrium of a spin system in interaction with the lattice. In particular here we have considered as a spin system a single spin, while in case of an ensemble of N-spins the number of spins N multiplies the resulting magnetization $\langle M_Z \rangle$.

1.6 Time evolution of density matrix: Liouville Von Neumann's equation

The equation of the motion of the density operator ρ for a given spin system is:

$$\frac{d}{dt}\rho = \frac{i}{\hbar}[\rho, H] \tag{1.14}$$

Where the term $[\rho, H] = \rho H - H\rho$ is the Lie's bracket for the operators ρ and H.

The Eq. (1.14) is the so-called Liouville Von Neumann equation, [15, 16]. This equation is the most general fashion to describe the time-evolution of a quantum system.

In the case where the Hamiltonian is time-independent the Liouville Von Neumann's equation has the simple solution:

$$\rho(t) = \exp\left(-\frac{iHt}{\hbar}\right)\rho_0 \exp\left(\frac{iHt}{\hbar}\right) = U^{\dagger}(t)\rho_0 U(t) \tag{1.15}$$

Where $\rho_0 = \rho(0)$ is the initial condition for the density operator ρ at $t = 0$, while the operator $U(t) = \exp(-iHt/\hbar)$ is termed the propagator of the quantum system. This operator is a time-dependent unitary operator and its calculation represents the central problem in quantum mechanics.

The simple form of $U(t)$ given in Eq. (1.15) it is not valid when the Hamiltonian is time-dependent. The propagator in this case is given by:

$$U(t) = T\exp\left(-\frac{i}{\hbar}\int_0^t H(t')dt'\right) \tag{1.16}$$

Where the T is the time-ordering operator (Dyson's operator). The meaning of T operator it is much clearer if we write the propagator $U(t)$ as a series expansion:

$$U(t) = \sum_{k=0}^{\infty}\frac{(-i)^k}{k!}\int_0^t dt_1\int_0^{t_1} dt_2 .... \int_0^{t_{k-1}} dt_k T\{H(t_1)H(t_2)...H(t_k)\} \tag{1.17}$$

For any set of values of the variables $t_1, t_2 .....t_k$ the action of T operator on the product $H(t_1)H(t_2)...H(t_k)$ is to place the Hamiltonians from right to the left as the time t increases.

1.7 Calculation of NMR signal

If the Hamiltonian H is piecewise time-independent in a suitable frame of reference, the calculation of the propagator is straightforward. Suppose there is a set of q time intervals with the duration $\{\tau_1, \tau_2, ...\tau_q\}$ during each of which the Hamiltonian is constant and equal to, $\{H_1, H_2, ...H_q\}$, i.e.,

$$H(t) = H_p, \qquad t_{p-1}^0 \le t < t_p^0$$

where

$$t_p^0 = \sum_{k=1}^{p}\tau_k, \qquad 1 \le p \le q$$

Then the propagator at time t_p^0 is given by an ordered cumulative product of the single propagators U_k's:

$$U\left(t_p^0,0\right)=U_pU_{p-1}....U_1 \qquad \text{and} \qquad U_k=e^{-iH_k\tau_k} \tag{1.18}$$

The corresponding density matrix at time t_p^0 is given by:

$$\rho\left(t_p^0\right)=U_p\rho(0)U_p^\dagger \tag{1.19}$$

Where $U\left(t_p^0,0\right)$ denotes adjoint of $U\left(t_p^0,0\right)^\dagger$. The NMR signal at time t_p^0 is given by the expectation value of the detection operator $S_+=S_x+iS_y$:

$$\left\langle S_+\left(t_p^0\right)\right\rangle \propto tr\left\{\rho\left(t_p^0\right)S_+\right\} \tag{1.20}$$

Where the symbol $tr\{\ \}$ denotes the trace operator. Finally Fourier transform of a series of complex data points $\left\langle S_+\left(nt_p^0\right)\right\rangle$ leads to the NMR spectrum. The data points are evenly spaced over a total time T_{tot} sufficient for the desired frequency resolution.

1.8 Liouville's Equation in interaction representation

In many instances the spin Hamiltonian can consist of a time independent part as well as time dependent part. In this case can be useful to switch the Liouville's equation in so-called interaction representation [17-19], (or interaction frame). The effect of this new representation is that of removing the time independent part of spin Hamiltonian from the Liouville' equation often leading quite to a useful simplification of its solution.

To illustrate how to obtain the interaction representation, we consider the follows spin Hamiltonian in laboratory frame:

$$H(t)=H_0+H_1(t) \tag{1.21}$$

Where H_0 and H_1 are the time-independent and time-dependent components respectively. The corresponding Liouville' equation is given by:

$$\frac{d}{dt}\rho = \frac{i}{\hbar}\left[\rho, H(t)\right] = \frac{i}{\hbar}\left[\rho, H_0 + H_1(t)\right] \tag{1.22}$$

In the interaction representation any operator O undergoes to a unitary transformation defined by:

$$\hat{O} = e^{iH_0 t} O e^{-iH_0 t} \tag{1.23}$$

Where the operator $\hat{O}$ is now the operator O in the interaction frame. Applying the transformation of Eq. (1.23) to the Liouville' equation (1.22), we obtain the corresponding equation in the interaction representation:

$$\frac{d}{dt}\hat{\rho} = \frac{i}{\hbar}\left[\hat{\rho}, \hat{H}_1(t)\right] \tag{1.24}$$

We note that the Eq. (1.24) preserves the same form as the original Liouville's equation; moreover it does not explicitly contain the time independent component H_0. Once we have solved the Eq. (1.24) we can obtain the density matrix $\hat{\rho}$ back into the laboratory frame just applying the inverse transformation defined in Eq. (1.23).

1.9 Spin interaction Hamiltonians

1.9.1 The Zeeman Hamiltonian

The dominant component of the nuclear spin Hamiltonian H_Z is the Zeeman Hamiltonian, which is the interaction energy of the magnetic moment $\vec{\mu}$ with an applied magnetic field $\vec{B}$.

$$H_Z = -\vec{\mu} \bullet \vec{B} \tag{1.25}$$

In a NMR experiment the applied magnetic field $\vec{B}$ can be distinguished in two fields: one of these is the static field $\vec{B}_0$, while the other is a time-dependent magnetic field $\vec{B}_1$. The Zeeman Hamiltonian due to static field $\vec{B}_0$ is given by:

$$H_0 = -\mu_Z B_0 = -\gamma B_0 I_Z = -\omega_0 I_Z \tag{1.26}$$

Where ω_0 is the Larmor-frequency and I_Z z-component of spin vector-operator $\vec{I}$ in the laboratory frame whose z-axis is chosen along direction of $\vec{B}_0$. The applied field $\vec{B}_1$ is a linearly polarized with a phase φ and oscillating in the laboratory frame with frequency ω_{RF}, which is at or close to the Larmor frequency $\omega_0/2\pi$:

$$\vec{B}_1(t) = 2B_1 \cos(\omega_{RF} t)\left[\vec{e}_x^{\,L} \cos\varphi + \vec{e}_y^{\,L} \sin\varphi\right] \tag{1.27}$$

B_1, is the amplitude of the field and $\vec{e}_x^{\,L}$, $\vec{e}_y^{\,L}$ are the unit vectors in x and y directions respectively of the laboratory frame. It is well known that a linearly oscillating field can be expressed as a sum of two counter-rotating components [20]. Depending on the sign of the Larmor frequency, nuclear spins will be in resonance with one of the two counter-rotating components of $\vec{B}_1$, as a result one of which can be neglected to an excellent approximation at high static field $\vec{B}_0$.

The corresponding Zeeman Hamiltonian in the laboratory frame is given by:

$$\begin{aligned} H_1 = -\gamma B_1 \left(I_x \cos(\omega_{RF} t + \varphi) + I_y \sin(\omega_{RF} t + \varphi)\right) = \\ -\omega_1 \left(I_x \cos(\omega_{RF} t + \varphi) + I_y \sin(\omega_{RF} t + \varphi)\right) \end{aligned} \tag{1.28}$$

Where $\omega_1/2\pi$ is the Rabi frequency. If the phase φ is constant in time, the time-dependence in Eq. (1.28) can be removed by transforming the laboratory frame into a coordinate system rotating (rotating-frame). This transformation is defined by the time–dependent unitary operator $U(t) = \exp(-i\omega_{RF} I_Z t)$, and the corresponding Hamiltonian H_1^R after this transformation is static:

$$H_1^R = U^{-1} H_1(t) U = -\omega_1 \left(I_x \cos\varphi + I_y \sin\varphi \right) \tag{1.29}$$

As it will be noted from Eq. (1.29) the spins are now interacting in the rotating frame with a static field $\vec{B}_1$ along the direction specified by the phase φ.

1.9.2 General form of internal spin Hamiltonians

The general form of internal spin interaction Hamiltonians [10, 16], is given by the following mathematical expression:

$$H_{\text{int}} = \hbar \vec{I} \hat{T} \vec{X} = \hbar \begin{pmatrix} I_x & I_y & I_z \end{pmatrix} \begin{pmatrix} T_{xx} & T_{xy} & T_{xz} \\ T_{yx} & T_{yy} & T_{yz} \\ T_{zx} & T_{zy} & T_{zz} \end{pmatrix} \begin{pmatrix} X_x \\ X_y \\ X_z \end{pmatrix} \tag{1.30}$$

The Eq. (1.30) specifies the internal Hamiltonians in Cartesian coordinates (x_L, y_L, z_L) of the laboratory frame; the first matrix operator is a spin nuclear operator, the second matrix defines the second-rank interaction tensor, while the third one may be a magnetic field or another nuclear spin operator. The second-rank tensor $\hat{T}$ contains the orientational dependence of the interaction between the spin vector $\vec{I}$ and the spin vector or magnetic field $\vec{X}$, and its nine components depend on the local symmetry of the nucleus and of the type of interaction. Suppose we have defined the interaction tensor $\hat{T}$ through their nine elements in an arbitrary reference system, (x, y, z) and then we can refer it to any other coordinate system, say (x', y', z'), by using a unitary transformation $R(\alpha, \beta, \gamma)$, [12, 13]. The components of the tensor $\hat{T}$ in new reference system (x', y', z') are given by:

$$\hat{T}' = R \hat{T} R^{-1} \tag{1.31}$$

The set of the angles $\Omega=(\alpha,\beta,\gamma)$, [4, 21, 22], are the Euler' angles that define the orientation of the (x',y',z') system with respect to the original coordinate system, (x,y,z). Apart in very special cases the interaction tensor $\hat{T}$ can be represented in its diagonal form by using a unitary transformation $R(\alpha,\beta,\gamma)$ starting, for example, from the laboratory frame (x_L,y_L,z_L) to the new frame (x_P,y_P,z_P), often called principal axis system (PAS). In this frame the principal components are T^P_{XX}, T^P_{YY}, T^P_{ZZ} and their ordering on the diagonal is established according to this convention, $|T^P_{ZZ}|\geq|T^P_{YY}|\geq|T^P_{XX}|$. By using the principal components T^P_{XX}, T^P_{YY}, T^P_{ZZ}, we can define some quantity related to the interaction tensor in order to specify its geometrical properties. One of these is the average of the tensor trace $\hat{T}_{iso}=\frac{1}{3}tr\{\hat{T}\}=\frac{1}{3}(T^P_{XX}+T^P_{YY}+T^P_{ZZ})$. This quantity is a tensor invariant, in the sense that it is the same in any reference system where the tensor is defined. As a consequence of that we observe the interaction in isotropic solution. We can also define the anisotropy and the asymmetry of tensor as $\delta=\hat{T}^P_{ZZ}-\hat{T}_{iso}$ and $\eta=(\hat{T}^p_{YY}-\hat{T}^P_{XX})/\hat{T}^P_{ZZ}$ respectively. The latter can assume values between one (for fully asymmetric tensors) and zero (for axially symmetric tensors).

As it well known in nuclear magnetic resonance very often we are dealing with different reference systems e.g., PAS-frame, molecular-frame (MF), laboratory-frame (LB) etc., depending upon the specific situation. As a result we need to transform the interaction tensors by using successive rotations of these reference systems. When rotations are involved it is convenient to use the interaction tensors in spherical representation rather than the Cartesian form as earlier done in this section.

The Cartesian tensors, [2], can be expressed in terms of spherical tensors. In particular a second rank Cartesian tensor T can be decomposed into a *scalar*, $\widehat{T}_0$, an

antisymmetric first rank tensor, $\bar{T}_1$ and a traceless *symmetric* second rank tensor, $\bar{T}_2$. This decomposition provides the irreducible representation of second rank Cartesian tensors, and the three tensors $\bar{T}_l$ are called *irreducible spherical tensors* of ranks $l = 0,1,2$. The corresponding Cartesian tensors T_l are related by:

$$T = \bar{T}_0 + \bar{T}_1 + \bar{T}_2 \tag{1.32}$$

In spherical representation the irreducible spherical tensors [23, 24] under rotation transform according to the irreducible representation of the rotation group D_k. Spherical tensor of rank k has $2k+1$ components, which are transformed under rotation of reference system as follows:

$$\bar{T}'_{kq} = \sum_{p=-k}^{k} \bar{T}_{kq} D^k_{pq}(\alpha,\beta,\gamma) \tag{1.33}$$

Where D^k_{pq} is the Wigner matrix [4] of order k, while α, β and γ are the Euler's angles that defines the rotation of the reference system xyz. Analogously we can express the spin operators and their functions in spherical form and under rotation of reference system they transform in the same way as the interaction tensors of Eq. (1.33). Under these circumstances we can rewrite the internal spin Hamiltonians, previously given in Cartesian coordinates, as inner product of spherical tensors:

$$H = \sum_{k=0}^{2} \sum_{q=-k}^{k} (-1)^q \bar{T}_{kq} \bar{A}_{k-q} \tag{1.34}$$

Here A_{q-k} are the spherical tensors due to spin operators, while T_{kq} the components of the spherical interaction tensor containing the lattice coordinates.

So far we have defined the spin Hamiltonian in general sense, giving it in both Cartesian and spherical coordinates. In the next sections we characterize the spin Hamiltonian by specifying the physical nature of the interaction tensor for those cases encountered in this work.

1.9.3 Interaction in high field approximation

So far we have considered the full internal spin Hamiltonians H_{int} without considering the fact that the spin system is interacting with a very large static magnetic field. This large magnetic field produces a Zeeman interaction whose Hamiltonian H_Z satisfy the condition:

$$\|H_Z\| \gg \|H_{\text{int}}\| \tag{1.35}$$

The Eq. (1.35) says that we can consider the internal Hamiltonian H_{int} as perturbation to the energy levels defined by the Zeeman Hamiltonian H_Z. At the first order in the perturbation theory the contribution to the NMR spectrum stems from those parts of H_{int} that commute with H_Z. This approximation splits the internal Hamiltonian in two parts:

$$H_{\text{int}} = H_{\text{int}}^{s} + H_{\text{int}}^{ns} \tag{1.36}$$

with, $\left[H_Z, H_{\text{int}}^{s}\right] = 0$ and $\left[H_Z, H_{\text{int}}^{ns}\right] \neq 0$. The Hamiltonian H_{int}^{s} is the so-called secular part, which determines at first order the structure of NMR spectrum, while the non-secular part H_{int}^{ns}, instead, governs the relaxation mechanism, [24].

By using the internal Hamiltonian, H_{int}, in the spherical coordinates, the secular part is given by:

$$H_{\text{int}}^{s} = T_{00}A_{00} + T_{10}A_{10} + T_{20}A_{20} \tag{1.37}$$

i.e. only the terms which commute with F_z, the z-component of the total spin operator. In Eq. (1.37) the quantities A_{00}, T_{00}, A_{10}, T_{10}, etc are the tensor components in the spherical form of the tensors A and T.

1.9.4 Chemical shift interaction

Depending on the local symmetry at the nuclear site, the magnitude of the chemical shift will vary as a function of the orientation of the molecule with respect to the external magnetic field. This orientation dependence of the chemical shift is referred to as chemical shift anisotropy (CSA). The physical origin of the chemical shift is explained in terms of the Lenz's law, [25]. The external field $\vec{B}_0$ interacting with the electrons surrounding the nucleus will induce currents $\vec{J}$, which depend upon the orientation and chemical nature of the molecule. These currents around the nucleus produce a local field $\vec{B}_{loc}$ that tends to oppose the external field $\vec{B}_0$:

$$\vec{B}_{loc} = -\sigma \vec{B}_0 \tag{1.38}$$

Where the quantity σ is the chemical shift tensor, which is mathematically described by a second-rank tensor (a 3 by 3 matrix). The interaction energy of the local field $\vec{B}_{loc}$ with the nuclear magnetism $\mu\vec{I}$ is thus:

$$H_{CS} = \vec{I} \cdot \sigma . \vec{B}_0 = \begin{pmatrix} I_x & I_y & I_z \end{pmatrix} \begin{pmatrix} \sigma_{xx} & \sigma_{xy} & \sigma_{xz} \\ \sigma_{yx} & \sigma_{yy} & \sigma_{yz} \\ \sigma_{zx} & \sigma_{zy} & \sigma_{zz} \end{pmatrix} \begin{pmatrix} 0 \\ 0 \\ B_0 \end{pmatrix} \tag{1.39}$$

In general the isotropic part of the tensor $tr\{\sigma\} \neq 0$ and σ is not necessarily symmetric. However the antisymmetric components of σ contribute to resonance shift only in second order and can be usually ignored. As a result only the symmetric part needed to be considered and the chemical shift (CS) tensor consists of six independent components. In this case, one is able to express the chemical shift tensor in a coordinate frame where all off-diagonal elements vanish. In this principal axis system, the chemical shift tensor is fully described by the three diagonal elements, the principal components, and the three eigenvectors or Euler angles describing the orientation of the principal axes with respect to an arbitrary frame. The chemical shift Hamiltonian in high field approximation is given by:

$$H_{CS}^{s} = \sigma_{zz} I_z B_0 \tag{1.40}$$

The quantity σ_{zz} is a combination of principal values of chemical shift tensor (see § 1.9.2):

$$\sigma_{zz} = \sigma_{iso} + \sigma_{zz}^{P} \frac{1}{2}\left[\left(3\cos^2\theta - 1\right) - \eta \sin^2\theta \cos 2\phi\right] \tag{1.41}$$

In isotropic solution the molecules undergo fast random motions and the angular dependence of the interaction vanishes, as a consequence the quantity σ_{zz} reduces to its isotropic value σ_{iso}.

1.9.5 Direct dipolar interaction

The direct, or through the space, dipole-dipole coupling is the interaction between nuclear magnetic moments directly through space. The interaction energy of two magnetic moments $\vec{\mu}_1 = \gamma_1 \hbar \vec{I}^{(1)}$ and $\vec{\mu}_2 = \gamma_2 \hbar \vec{I}^{(2)}$ is given by the Zeeman interaction, say of $\vec{\mu}_2$ with the magnetic field produced, say by the magnetic moment $\vec{\mu}_1$, at site of $\vec{\mu}_2$, [6]:

$$H_{dip} = \frac{\mu_0 \hbar^2 \gamma_1 \gamma_2}{4\pi r_{12}^3}\left[\vec{I}^{(1)} \cdot \vec{I}^{(2)} - 3\frac{\left(\vec{I}^{(1)} \cdot \vec{r}_{12}\right)\left(\vec{I}^{(2)} \cdot \vec{r}_{12}\right)}{r_{12}^2}\right] \tag{1.42}$$

Here μ_0 is the permeability in vacuum and $\hbar$ is the Planck's constant. If the gyromagnetic ratios γ_1 and γ_2 are equal the corresponding dipolar coupling is called *homonuclear* otherwise *heteronuclear.*

Besides fundamental constants, the direct dipole-dipole coupling depends on the inverse cube of the internuclear distance r_{12} and the orientation of the internuclear vector $\vec{r}_{12}$ with respect to the interacting magnetic moments $\vec{\mu}_1$ and $\vec{\mu}_2$.

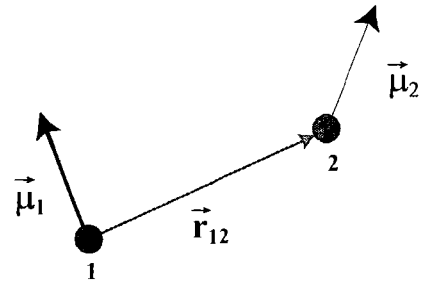

Figure 1.1 Schematic representation of two nuclei with magnetic moments $\vec{\mu}_1$ and $\vec{\mu}_2$ separated by the internuclear vector $\vec{r}_{12}$.

It is this strict geometric dependence, which makes the dipolar coupling an invaluable tool in the determination of molecular structure. The dipolar Hamiltonian of Eq. (1.42) can be represented in matrix form as follows:

$$H_{dip} = \begin{pmatrix} I_X^{(1)} & I_Y^{(1)} & I_Z^{(1)} \end{pmatrix} \begin{pmatrix} D_{xx} & D_{xy} & D_{xz} \\ D_{yx} & D_{yy} & D_{yz} \\ D_{zx} & D_{zy} & D_{zz} \end{pmatrix} \begin{pmatrix} I_X^{(2)} \\ I_Y^{(2)} \\ I_Z^{(2)} \end{pmatrix} \tag{1.43}$$

The interaction dipolar tensor $\hat{D}$ is then defined as:

$$D_{ij} = \frac{\mu_0 \hbar^2 \gamma_1 \gamma_2}{4\pi r_{12}^3} \left(\delta_{ij} - 3 e_i e_j \right) \quad \text{and} \quad \{i, j\} = x, y, z \tag{1.44}$$

Where δ_{ij} is the Kronecker's delta and e_j $(j = x, y, z)$ are x, y and z-components of a unit vector pointing from one spin to the other. From Eq. (1.44) it is straightforward to see that trace of tensor $\hat{D}$ is equal to zero ($tr\{\hat{D}\} = 0$), and that it is symmetric ($D_{ij} = D_{ji}$). This symmetry means that always the dipolar interaction tensor $\hat{D}$ has a principal axis system (PAS) in which assume the diagonal form. Moreover this tensor is always axially symmetric ($\eta = 0$) and one of the principal axes is parallel to the internuclear vector $\vec{r}_{12}$.

In high field approximation the truncated heteronuclear and homonuclear dipolar Hamiltonian are given by:

$$H_S = D_{zz} I_z^1 I_z^2 \qquad \text{(Heteronuclear case)} \qquad (1.45)$$

$$H_S = D_{zz}\left(3I_z^1 I_z^2 - \vec{I}^1 \cdot \vec{I}^2\right) \qquad \text{(Homonuclear case)} \qquad (1.46)$$

where the quantity D_{zz} is a component of the interaction tensors in the laboratory frame (LB) :

$$D_{zz} = \frac{\mu_0 \hbar^2 \gamma_1 \gamma_2}{4\pi r_{12}^3}\left(1 - 3\cos^2 \vartheta_{12}\right) \qquad (1.47)$$

where the angle ϑ_{12} is the angle between the magnetic field $\vec{B}_0$ and the inter-nuclear vector $\vec{r}_{12}$.

1.9.6 Scalar (J) interaction

J coupling is different from dipolar interaction (dipole-dipole). J-coupling works through the electrons in bonds while the dipolar interaction is a direct interaction, that is, through space. The corresponding Hamiltonian is given by:

$$H_J = 2\pi\begin{pmatrix} I_X^{(1)} & I_Y^{(1)} & I_Z^{(1)} \end{pmatrix}\begin{pmatrix} J_{xx} & J_{xy} & J_{xz} \\ J_{yx} & J_{yy} & J_{yz} \\ J_{zx} & J_{zy} & J_{zzz} \end{pmatrix}\begin{pmatrix} I_Z^{(2)} \\ I_Y^{(2)} \\ I_Z^{(2)} \end{pmatrix} \qquad (1.48)$$

Unlike the through space dipolar interaction tensor $\hat{D}$, the interaction tensor $\hat{J}$ it is not symmetric and has a non-zero trace, $J = (1/3)tr\{\hat{J}\}$ called *isotropic J-coupling*. As we know rapid and isotropic molecular tumbling over NMR time scale removes the anisotropic interaction, so that in a liquid only the trace of the interaction tensor is observable. In these circumstances the corresponding Hamiltonian is:

$$H_J^{iso} = 2\pi J \vec{I}^1 \cdot \vec{I}^2 \tag{1.49}$$

The *J-coupling* is the order of ~10^0-10^3 Hz. In high field approximation the homonuclear *J-coupling* Hamiltonian is the same as in Eq. (1.49), while for heteronuclear case we have:

$$H_J^{iso} = 2\pi J I_z^1 I_z^2 \tag{1.50}$$

In solids and in oriented systems the anisotropic part of the $\hat{J}$ tensor survives, and the corresponding heteronuclear and homonuclear Hamiltonians in high field approximation are given by:

$$H_J^{aniso} = 2\pi J^{aniso} I_z^1 I_z^2 \qquad \text{(Heteronuclear case)} \tag{1.51}$$

$$H_J^{aniso} = 2\pi J^{aniso} \left(3 I_z^1 I_z^2 - \vec{I}^1 \cdot \vec{I}^2\right) \qquad \text{(Homonuclear case)} \tag{1.52}$$

Where the term J^{aniso} is a tensor component of the interaction tensor $\hat{J}$.

J-coupling constitutes an important link between NMR and chemistry; in fact it depends, since it often depends in a systematic way, on the molecular structure parameters such as bond angles. For example, in rigid organic molecules the 3-bond ^{1}H—^{1}H *J-couplings* have a strong geometrical dependence by the *torsional angles* [26] around the central bond transmitting the coupling. This property is used in the determination of protein structure. In addition there are no *J-couplings* between different molecules, a remarkable property of great importance in liquid state NMR.

1.10 Disordered *vs.* ordered systems

As we know molecules in a liquid samples undergo rotational random motions, which can be characterized by a correlation time τ_c. These motions make the interaction tensors time dependent. Since the molecules assume all orientations with same probability and with a time scale τ_c, much shorter than the NMR time scale, the

anisotropic interactions are averaged to zero. This stochastic averaging has a strong effect on NMR spectra, leading sharp intense peaks only due to the isotropic part of the interaction tensors. Beside disordered liquid samples, single crystals also give sharp resonances because a single orientation of the interaction tensors is present. In this case the anisotropic spin interaction tensors can be determined. However very often single crystals are not available or it is very difficult to grow. In this case powdered samples have to be investigated. These are disordered solid systems with randomly orientated tiny crystallites (group of molecules). In contrast to the liquid case, now the molecular motion is strongly restricted, or even completely absent, and the anisotropic part of the interaction tensors lead to different resonance frequencies depending on the molecular orientation. Figure 1.2 shows simulated powdered spectra for the chemical shift interaction tensor in a single spin-1/2 system. The resulting broad line is due to a superposition of individual sharp peaks, which correspond to the different molecular orientations with respect to the static magnetic field $\vec{B}_0$. As seen in Figure 1.2 the line-shape depends on the value of the asymmetry parameter η. In the high-field approximation (secular Hamiltonian) in the laboratory frame is:

$$\hat{T}_{zz}(\theta,\phi) = T_{iso} + \frac{1}{2}\delta\left(3\cos^2(\theta) - 1 + \eta\sin^2(\theta)\cos(2\phi)\right) \tag{1.53}$$

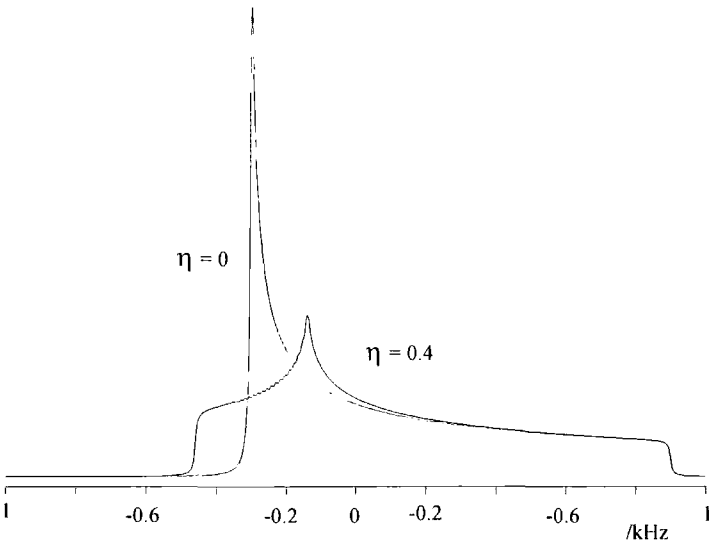

Figure 1.2 Simulated powder spectra for the second-rank chemical shift interaction as a function of asymmetry parameters η. The trace in red corresponds to an axially symmetric tensor ($\eta = 0$), while for the black trace the asymmetry parameter is $\eta = 0.4$. The simulation has been performed using a c++ code given in the appendix.

The spectral position of a resonance is proportional to the z-component $\hat{T}_{zz}$ of Eq. (1.53) and by varying the angles θ and ϕ within the ranges, $[0,\pi]$ and $[0,2\pi]$ respectively we obtain the line shapes as in Figure 1.2. It is worth nothing that the spectral sensitivity and the resolution of NMR spectra of powdered systems is very low and very often this may limit the application of the technique.

1.11 Magic angle spinning

As we mentioned in the previously section, all anisotropic interactions are averaged out by the fast molecular motion in isotropic liquids. This can also be done in powdered solids provided that the sample is rapidly rotating about a proper axis, [27-29]. This spinner axis must be tilted from the static magnetic field $\vec{B}_0$ by the so-"magic angle", which corresponds to $\arccos\left(1/\sqrt{3}\right) \approx 54.47^\circ$. The resulting refocusing

of the second rank interaction tensors improves both resolution and sensitivity of the NMR spectra of these powdered samples. In Figure 1.3 is shown a simulated spectrum of spin-1/2 with the chemical shift interaction under magic angle spinning. The rotation of the sample breaks the static line shape (see Figure 1.2) into a series of spinning sidebands spaced by the spinning speed ν_R. The case in which the strength of the spinning speed is considerably less than the size of internal Hamiltonian ($2\pi\nu_R < \|H_{\text{int}}\|$), the spinning sideband intensities mirror the profile of the static spectrum, as shown at the top of Figure 1.3. This means that within the rotor-echo, τ_R, during time interval fixed by the $\left(2\pi/\|H_{\text{int}}\|\right)$, the internal time-dependent Hamiltonian does not change dramatically and the spin system tends to evolve as if it was quasi-static. At greater spinning speeds ($2\pi\nu_R > \|H_{\text{int}}\|$), however, the influence of the interaction is increasingly attenuated, leaving on the spectrum few spinning sidebands with a predominant centerband. At very large spinning speed ($2\pi\nu_R \gg \|H_{\text{int}}\|$) an essentially complete averaging of the anisotropic part of the interaction tensor occurs. The resulting spectrum consists of a single peak (centerband) due to the isotropic part of the interaction tensor with a full suppression of the spinning sidebands.

So far we have implicitly assumed the formation of the rotor-echo [30], and corresponding sharp spinning sidebands on the spectrum, simply by rotation the sample at magic angle. It is important to note that the formation of rotor echo depends on whether or not the periodic internal Hamiltonian is self-commuting at different times. With self-commuting Hamiltonian, $\left[H(t_a), H(t_b)\right] = 0$, only the spin eigenvalues, but not the eigenvectors are perturbed during the rotor cycle. As a result the propagator U is periodic leading to rotational echoes
with narrow centerband and sidebands in the MAS spectrum. In this case we say that the Hamiltonian has an "inhomogeneous" behaviour. This is the case for the heteronuclear dipolar or chemical shift Hamiltonians. In contrast, under most

conditions, the flip-flop term [31] of the homonuclear couplings results in non-commutation of the spin Hamiltonian with itself at different times. As a result the propagator is not periodic and no full rotational echoes are observed. Efficient suppression of homonuclear interactions is only achieved by spinning the sample much faster than the magnitude of the interactions involved.

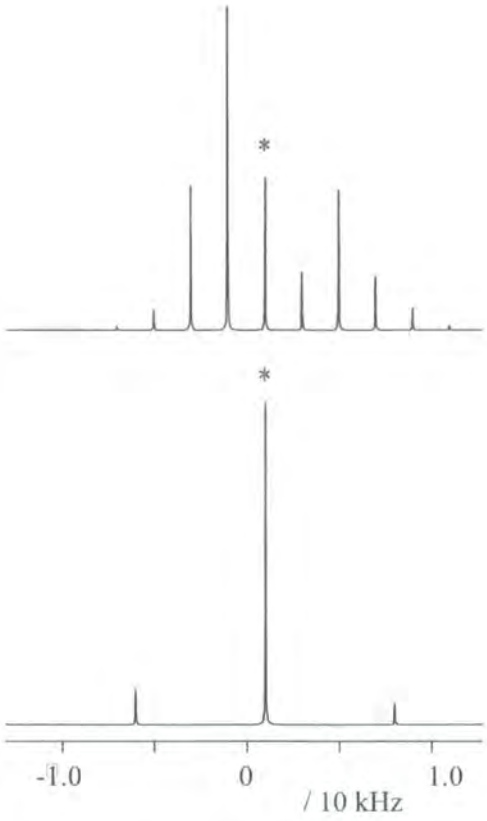

Figure 1.3 Simulation of NMR spectrum of second-rank chemical shift interaction under magic angle spinning. The anisotropy and isotropy with an asymmetry parameter $\eta = 0$ of the chemical shift are 9 kHz and 1 kHz respectively. At the top of the Figure the spinning speed is 2 kHz, while on the bottom it is 7 kHz. The stars on the spectra are mark to the centerband, whose frequency is independent of the spinning speeds. The simulation has been performed using a c++ code reported in the appendix programs.

1.12 Cross-polarization

Cross-polarisation (CP) [32] is a fundamental tool in solid state NMR of dilute spins. It allows magnetization from a spin, say *I*, with high abundance (e.g. ^{1}H, ^{19}F, and ^{31}P), to be transferred to a system of spins, say *S*, with low abundance, such as ^{13}C, ^{15}N, etc. The resulting enhancement in sensitivity of these rare nuclei S is proportional to the ratio γ_I/γ_S (which is a factor of ~ 4 for ^{13}C cross polarized by protons). In addition the rate at which *S*-spin coherence can be produced in successive transients is now determined by the relatively fast spin-lattice relaxation of abundant spins (T_{1I}) rather than by T_{1S}. This further improves the S/N per unit time.

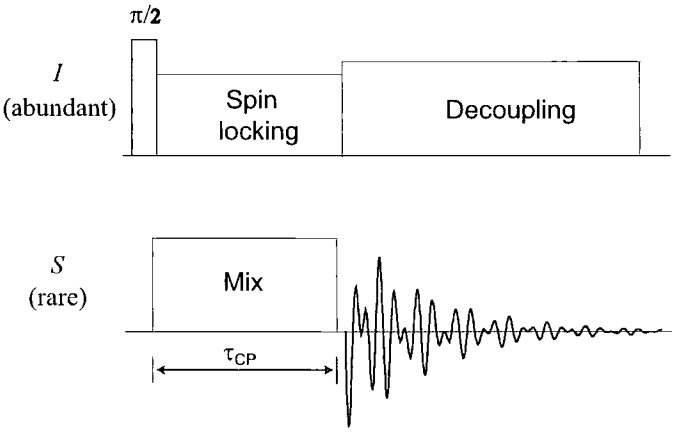

Figure 1.4 Schematic representation of CP experiment. During the time interval τ_{CP} the nuclei, *S* and *I* are simultaneously irradiated by the fields $\vec{B}_{1I}$ and $\vec{B}_{1S}$ with strength such that the corresponding nutation frequencies Ω_I and Ω_S are matched. After the time interval, τ_{CP}, the *S*-spin signal is, usually, acquired under decoupling to remove *I*-*S* dipolar interactions.

A typical CP experiment is shown in Figure 1.4. A $\pi/2$ pulse is applied to the *I*-spins, tilting the *I*-spin magnetization, initially along the static field $\vec{B}_0$ (z-axis), into x-y plane. During, τ_{CP}, both *S* spin and *I* are simultaneously irradiated by $\vec{B}_{1I}$ and $\vec{B}_{1S}$ RF-fields at their respective Larmor frequencies $\omega_{0,I}$ and $\omega_{0,S}$. The *I*-spin

magnetization is locked by applying a $\vec{B}_{1I}$ field parallel to this magnetization. When the strength of $\vec{B}_{1I}$ and $\vec{B}_{1S}$ are such that the nutation frequencies $\Omega_I = \gamma_I B_{1,I}$ and $\Omega_S = \gamma_S B_{1,S}$ are equal (Hartmann-Hann condition) the energy transfer from *I*-spins to *S*-spins can take place, with corresponding enhancement of the transverse *S*-spin magnetization. This energy transfer is caused by *I*-*S* dipolar interactions that induce flip-flop transitions (zero-quantum transitions) between Zeeman states, which are relative to the quantization axes defined by the fields $\vec{B}_{1I}$ and $\vec{B}_{1S}$ in the appropriate double rotating frame.

References

1. J. W. Emsley: Nuclear Magnetic Resonance of Liquid crystals, *NATO ASI Series* (1983)
2. J. J. Sakurai: Meccanica Quantistica Moderna, *Zanichelli, Bologna* (1990), Chapter 3.
3. D. A. Varshalovich, A. N. Moskalev, V. K. Khersonskii: Quantum Theory of Angular Momentum, *Word Scientific, Singapore* (1988)
4. M. E. Rose: Elementary Theory of Angular Momentum, *Wiley, New York* (1995), Chapter 5.
5. C. P. Slichter: Principles of Magnetic Resonance, *Springer-Verlag Berlin Heidelberg New York*, (1989), Chapter 2.
6. B. C. Gerstein, C. R. Dybowski: Transient techniques in NMR of solids, *Academic Press INC* (1985), Chapter 1.
7. R. Freeman: Spin choreography. Basic Steps in High Resolution NMR, *Oxford University Press* (1998), Chapter 2.
8. R. R. Ernest, G. Bodenhausen, A. Wokaun: : Principles of Nuclear Magnetic Resonance in one and two dimensions, *Oxford University Press, London* (1987), Chapter 2.
9. R. I. G. Hughes: Structure and Interpretation of Quantum Mechanics, *Harvard University Press* (1992), Chapter 2.
10. M. Mehring, V.A.Weberruβ: Object-Oriented Magnetic Resonance *Academic Press INC* (2001), Chapter 3.
11. A. W. Joshi: Elements of Group Theory for Physicists, *Wiley Eastern Private Limited* (1973), Chapter 2.
12. M. G. Arfken: Mathematical methods for Physicists, *3rd. ed., Academic Press, New York* (1985).
13. P. Halmos: Introduction to Hilbert Spaces, *AMS Chelsea Publishing, 2nd edition* (1957).
14. L. D. Landau, E. M. Lifshtz: Fisica Statistica, *Editori Riuniti* (1986), Chapter 3.
15. A. Abragam: Principles of Nuclear Magnetism, *Oxford University Press*, (1961), Chapter 2.

16. M. Mehring: Principles of High Resolution NMR in Solids, *Springer-Verlag, Berlin* (1983), pp.31-32.

17. G. Baym: Lectures on Quantum Mechanics, *Addison Wesley* (1973).

18. J. J. Sakurai: Meccanica Quantistica Moderna, *Zanichelli, Bologna* (1990), Chapter 5.

19. L. Schiff: Meccanica Quantistica, *Boringhieri* (1963), Chapter 6.

20. C. P. Slichter: Principles of Magnetic Resonance *Springer-Verlag Berlin Heidelberg New York* (1989), pp. 20-21.

21. D. Freude, J.Haase: NMR Basic Principles and Progress, *Springer Verlag, Berlin* **Vol. 29** (1993), pp. 25.

22. H. Goldstein: Classical Mechanics, *2nd. ed., Addison-Wesley, Reading, MA* (1980), Chapter 4.

23. E. Merzbacher: Quantum Mechanics, *John Wiley* (1997).

24. S. Dattagupta: Relaxation Fenomena in Condensed Matter Physics, *Academic Press INC* (1987).

25. J. D. Jackson: Classical Electrodynamics, *2nd ed., Wiley* (1975), Chapter 6.

26. M. H. Levitt: Spin Dynamics, *John Wiley* (2001), Chapter 7.

27. E. R. Andrew, A. Bradbury, R. G. Eades, *Nature* **183,** 1802-1803 (1959).

28. I. J. Lowe, *Phys. Rev. Lett.* **2 (7)**, 285-287 (1959).

29. G. Wu, R. E. Wasylishen, *J. Chem. Phys.* **99 (9)**, 6321-6329 (1993).

30. K. Schmidt-Rohr, H. W. Spiess: Multidimensional Solid-State NMR and Polymers, *Academic Press, London* (1994), pp.113.

31. A. Pines, M. G. Gibby, J. S. Waugh, *J. AM. Chem. Phys* **56**, 1776 (1972).

32. J. Schaefer, E. O. Stejskal, *J. AM. Chem. Soc.* **98**, 1031 (1976).

Chapter 2

Decoupling theory

2.1 Introduction

High resolution NMR in solids and liquid crystals requires that the effect of spin-spin interactions must be drastically reduced. The coupling between different types of nuclear spins leads to splitting or broadening of NMR peaks. Decoupling of the abundant spins (e.g., ^{1}H, ^{19}F) often results in substantial improvement in the spectral quality of rare spins (e.g. ^{13}C, ^{15}N). For liquid samples, the main problem is to remove heteronuclear *J*-coupling for nuclei having a wide range of resonance frequencies due to the presence of chemical shift. In liquid crystals and solids the major heteronuclear interactions are dipolar couplings, which are usually of the order of 10 and 40 kHz respectively.

The basic idea on which all decoupling schemes work can be understood as follows: the existence of two lines in the *S*-spin spectrum corresponds to the fact that the *I*-spins have two orientations, up and down. Such orientations correspond to two effective fields [1] that interacting with the *S*-spin give rise to two absorption frequencies in the *S*-spectrum. Applying a RF field to the *I*-spin at its own Larmor frequency, the *I*-spin flips back and forth between up and down orientations. If this flipping is sufficiently fast ($\gamma B_1 \gg$ *strength of spin-spin interaction*) the *S*-spin "sees" an averaged effective field and it will precess at a time-averaged frequency rather than at one or the other of two discrete frequencies. This means that the *S*-spin doublet will collapse into single peak whose frequency it will be determine by its chemical shift.

2.2 Heteronuclear decoupling in *IS* systems

In order to understand the different decoupling schemes we can consider a simple *IS* spin system, evaluating the *S*-signal while the *I*-spin is subject to an arbitrary time dependent perturbation H_{RF}. The Hamiltonian is given by:

$$H(t) = \delta_S S_Z + \delta_I(t) I_Z - 2d_{IS} S_Z I_Z + H_{RF}(t) \tag{2.1}$$

Where the time dependence of $H(t)$ Hamiltonian is determined by an effective RF-field $\vec{B}_{eff}(t)$ as follows [2]:

$$\vec{B}_{eff}(t) = \vec{B}_1(t) + \frac{1}{\gamma_I}\delta_I(t)\hat{e}_z = B_1\cos\varphi(t)\hat{e}_x + B_1\sin\varphi(t)\hat{e}_y + \frac{1}{\gamma_I}\delta_I(t)\hat{e}_z \tag{2.2}$$

Where $\delta_I(t) = \omega_{0I} - \omega_{RF}(t)$ is the proton chemical shift, which is measured with respect to ω_{RF}, whereas the carbon chemical shift δ_S can be ignored since causes only a shift of the *S*-NMR spectrum. The parameters $B_1, \varphi, \omega_{RF}$ are the amplitude, phase and frequency of the RF-field. The time dependence of these parameters determines the most general form of the decoupling scheme.

The corresponding interaction of $\vec{B}_{eff}(t)$ with the nuclear $\vec{I}$-spin is in the rotating frame given by:

$$\gamma_H \vec{B}_{eff} \cdot \vec{I} = \gamma_I B_1 \left[\cos\varphi(t) I_X + \sin\varphi(t) I_Y\right] + \delta_I(t) I_Z = H_{RF} + \delta_I(t) I_Z \tag{2.3}$$

We can, conveniently, to explicit the time dependence of $\vec{B}_1(t)$ as a sequence of piece-wise constant "*states*" H^k. Since $\left[H(t), S_Z\right] = 0$, H is represented in a generic "*k-state*" as:

$$H^k = H^k{}_+ \oplus H^k{}_- \tag{2.4}$$

The sub-matrices $H^k_{\pm}$ corresponding to $|\alpha\rangle$ and $|\beta\rangle$ *S* spin sub-space respectively:

$$H_{\pm}^{k} = \left(\delta_I\left(t_k\right) \pm d_{IS}\right) I_Z + H_{RF}\left(t_k\right) = \vec{\omega}_{e;\pm}^{k} \cdot \vec{I} \tag{2.5}$$

Where the vectors, $\vec{\omega}_{e;\pm}^{k}$, are defined as follows:

$$\vec{\omega}_{e;\pm}^{k} \equiv \left(\gamma_I B_1 \cos\varphi\left(t_k\right) \quad \gamma_I B_1 \sin\varphi\left(t_k\right) \quad \delta_I\left(t_k\right) \pm d_{IS}\right) \tag{2.6}$$

The propagator is also block diagonal:

$$U^k = U_+^k \oplus U_-^k \tag{2.7}$$

Where $U_{\pm}^{k}$ in this case are pure rotations, [3], of the *I*-spin in the relative α and β spin *S* sub-space.

The propagator in the time interval $t_s = \sum_{k=1}^{N} t_k$ is a 4×4 diagonal block matrix whose blocks are given by the successive ordered multiplications of the sub-matrixes $R_{\pm}^{k}$ relative to the "*N-states*" of RF-field $\vec{B}_1(t)$ (Note that "*N-states*" means a series of values of $\vec{B}_1(t)$ at different times, $t_1, t_2, \ldots\ldots t_N$):

$$U\left(t_s, 0\right) = \left[\begin{array}{c|c} R_+ & 0 \\ \hline 0 & R_- \end{array}\right] \qquad \text{with} \quad R_{\pm} = R_{\pm}^{N} R_{\pm}^{k-1} R_{\pm}^{k} \ldots . R_{\pm}^{1} \tag{2.8}$$

and the FID at time t_s is given by:

$$FID\left(t_s\right) = 2tr\left\{R_+ R_-^{-1}\right\} \tag{2.9}$$

The time t_s is the sampling interval; therefore considering one sequence of values, $FID\left(nt_s\right)$, the Fourier transform of this sequence gives the exact calculation *S*-spectrum for an arbitrary decoupling sequence.

In particular since many sequences are periodic and with period t_r not very long, generally, we can assume that the sampling period t_s is equal to the period t_r. This yields an enormous simplification of the theory without loosing the physical information of the results. Sampling the *FID* within the cycle period t_r cyclic sidebands can be observed in the spectrum as it occurs in any periodic problem[4, 5].

However under decoupling field normally used, in practice the *FID* is routinely sampled within decoupling period without observing appreciable spinning sideband intensities.

Extending the *FID* of Eq. (2.9) over nt_r sampling points, after the Fourier's transform we obtain the corresponding spectrum, which consist of δ-functions at frequencies $\pm\nu_m$ and $\pm\nu_s$:

$$\nu_m = \frac{\Phi_+ - \Phi_-}{2t_r} \qquad \text{and} \qquad \nu_s = \frac{\Phi_+ + \Phi_-}{2t_r} \tag{2.10}$$

Where the quantities $\Phi_\pm$ are the full phases accumulated by the successive rotations of *I*-spin vector in the relative α and β sub-spaces and their definition is a consequence of property of rotations.

As it will be noticed the spectrum consist of four peaks, which are due to the main transitions, $\pm\nu_m$ and the satellite transitions $\pm\nu_s$. The heteronuclear spectrum of *I-S* spin-1/2 with no decoupling gives two peaks at the frequencies $\pm\nu_m$ as sketched in the simulation of Figure 2.1-a. When a RF-field is added, transitions previously forbidden are now partially allowed giving rise to the satellite transitions $\pm\nu_s$ as seen in Figure 2.1-(b-c). However the satellite resonances, $\pm\nu_s$, decrease their intensity as the strength of RF-field increases, and with the decoupling power normally used (50-100 kHz) they usually have a negligible intensity. It is worth noting that the satellite transitions are also present when the RF-field is applied in on-resonance.

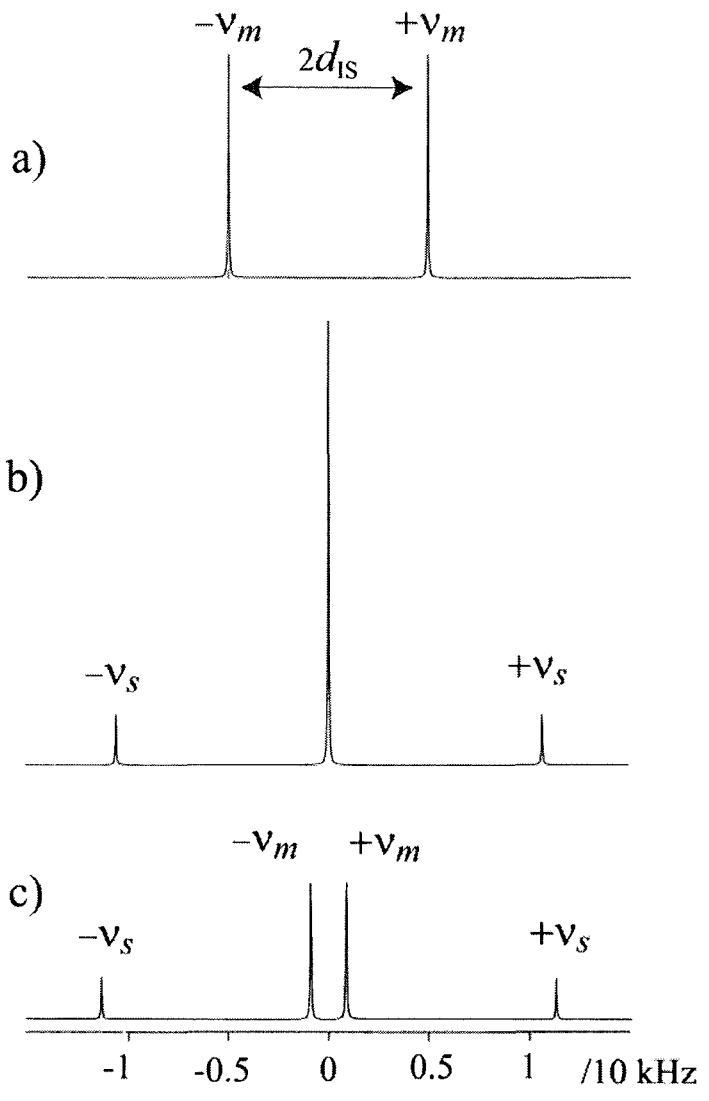

Figure 2.1 *S*-spin simulated spectra with no irradiation (a), and on / off resonance *I*-spin irradiation (b-c). The simulations were performed according to the Hamiltonian given in Eq. (2.1). The (b)-spectrum is relative to a RF-field in a single "*state*", which is referred in literature as a continuous irradiation (CW decoupling). The corresponding H_{RF} Hamiltonian in the rotating frame is given by - $\gamma_I B_1 I_X$ (see Chapter 1). The simulation parameters are: decoupling power, 10 kHz, dipolar coupling d_{IS}, 5 kHz, and off resonance δ_I, 0.5 kHz. It should be noticed that the satellite transitions shown in the simulations (b-c) are quite intense since the decoupling power used (10 kHz) is the same order of magnitude of dipolar coupling, d_{IS} (5 kHz). If the B_1 field becomes strong such that $\gamma_I B_1/2\pi \gg |d_{IS}|$ the intensity satellite transitions are negligibly small.

The impact of RF-field on the main transitions is notable. In condition of on-resonance irradiation the splitting from the main transitions collapses into single peak, while for a non-zero shift from the on-resonance this splitting results in a scaled doublet.

2.2.1 Off-resonance decoupling

Off-resonance decoupling, in heteronuclear spin systems determines a non-zero scaling χ of spin-spin interactions. For a simple AX spin system (with X spin decoupled), we can easily derive the size of this scaling factor as a function of offset-irradiation. The resulting AX-Hamiltonian with CW decoupling can be written

$$H_T = H_0 + H_1 \tag{2.11}$$

The H_1 Hamiltonian is given by:

$$H_1 = (\omega_X - \omega_2) I_Z^X - \gamma_X B_2 I_x^X \tag{2.12}$$

The first term in Eq. (2.12) is the offset term of X spin, while the second term is the interaction between the decoupling field B_2, and magnetic moment of X spin. The "unperturbed " Hamiltonian H_0 is then:

$$H_0 = H_A - 2d_{AX} I_z^A I_z^X \tag{2.13}$$

Where in Eq. (2.13) the first operator H_A, represents the chemical shift interaction for A-spin, while the second term, is the A—X dipolar term. In order to apply the Average Hamiltonian Theory (AHT), [6, 7] it is necessary to redefine the Hamiltonian H_0 in an appropriated interaction frame of which one of its axes is given by a new quantization axis of the X-spin. Effectively, this axis is implicitly defined by means of the Hamiltonian H_1. In fact, the operator H_1 can be rewritten as an

inner product of an effective field, $\vec{B}_{eff} = \{B_2, 0, (\omega_X - \omega_2)/\gamma_X\}$, with the X spin-vector operator $\vec{I}^X$. The effective field, $\vec{B}_{eff}$, determines the direction of the new X quantization-axis. Expressing $\vec{I}^X$ in terms of the new operator $\vec{I}'^X$, the H_0 Hamiltonian assumes the following form:

$$\begin{aligned}\tilde{H}_0^T(t) = H_A - 2d_{AX} I_z^A \Big[I_z'^X \cos\theta - I_x'^X \sin\theta \cos(\gamma_X B_{eff} t) + \\ + I_y^X \sin\theta \sin(\gamma_X B_{eff} t)\Big]\end{aligned} \tag{2.14}$$

Where θ angle is defined by:

$$\theta = \tan^{-1}\left[\frac{\gamma_X B_2}{\omega_2 - \omega_X}\right] \tag{2.15}$$

As it will be noticed, in Eq. 4.4 the terms H_A and I_y^X, remain invariant under rotation to the new reference axis. This is because the unitary operator which defines the rotation commutes with both operators H_A and I_y^X. It is important to note that because we are considering a simple AX system the corresponding Hamiltonian is periodic with a cycle time t_r, which is defined by the equation, $\gamma_X B_{eff} t_r = 2\pi$. However in a more general situation many others non-equivalent X nuclei could be coupled to a single A nucleus in the molecule. As a result no single cycle t_r for all of them is possible. This implies that the cyclic condition [8] cannot be fulfilled for all X-spins in the molecule since each X-spin is associated to a different effective field B_{eff}. However, we are often in the experimental situation in which the strength of the RF-field is sufficient to make the cycle time t_r short enough such that the contribution of the time-dependent terms in Eq. (2.14) is negligible. Under this condition the first term of average Hamiltonian is given by:

$$\bar{H}_0^{(0)} = \frac{1}{\tau_c}\int_0^{\tau_c} \tilde{H}_0^T(t)\,dt = H_A - 2d_{AX}\cos\theta I_z^A I_z'^X \tag{2.16}$$

The term $\cos\theta$ in Eq (2.16) is the scaling factor χ of the A—X dipolar coupling constant d_{AX}. Obviously in the case where non-equivalent A's nuclei are present, the corresponding scaling factor $\cos\theta$ will be different for each X-spin.

Under condition of strong decoupling fields, $|\gamma_X B_2| \gg |\omega_2 - \omega_X| = |\Omega_X|$, the residual dipolar coupling constant can be approximated by:

$$d_{AX}^{reduced} = d_{AX}\chi = d_{AX}\left|\frac{\Omega_X}{\gamma_X B_{eff}}\right| \approx d_{AX}\left|\frac{\Omega_X}{\gamma_X B_2}\right| \tag{2.17}$$

From Eq. (2.17) it is straightforward to see that by varying the frequency ω_2 we can change the size of residual dipolar couplings. This permit to exploit off-resonance decoupling as a method for assignments in heteronuclear spin systems

2.2.2 Decoupling criteria

As we have shown the paragraph above we can calculate the *S*-spin signal under an arbitrary piecewise time-dependent RF-Hamiltonian. We now need to establish some criteria in order to quantify the effects on *S*-spin spectrum given a time dependence of RF-Hamiltonian. From Eq (2.10) we can quantify the effective dipolar interaction by calculating the splinting of the main transitions $\pm\nu_m$:

$$d_{IS}^{eff} = \nu_m = \lambda d_{IS} \tag{2.18}$$

λ represents the scaling factor of the dipolar coupling due to the decoupling.

The total phases accumulated $\Phi_\pm$ depend on the quantities $\delta_I \pm d_{IS}$ so we can write the scaling factor λ [3] as follows:

$$\lambda = \frac{d_{IS}^{eff}}{d_{IS}} = \frac{1}{t_r}\frac{\Phi(\delta_I + d_{IS}) - \Phi(\delta_I - d_{IS})}{2d_{IS}} \tag{2.19}$$

In the limit of small dipolar coupling d_{IS} ($|d_{IS}| \ll |\delta_I|$), which usually occurs in liquid samples, this reduces to:

$$\lambda = \frac{1}{t_r}\frac{\partial \Phi}{\partial \delta_I} \tag{2.20}$$

Perfect decoupling corresponds to a scaling factor $\lambda = 0$ irrespective of the chemical shift δ_I. In practice the performance of decoupling is optimised by minimizing λ over a given range of δ_I (broadband decoupling). In solid and liquid crystal samples the criterion of decoupling of Eq. (2.20) is no longer valid. This is because generally $|d_{IS}| > |\delta_I|$. Moreover the treatment ignores *I-I* homonuclear interactions, which are significant in these phases. However we can recover a more general decoupling condition if we require that over multiple of cycle period t_r we have:

$$R_+ = R_- \tag{2.21}$$

The Eq. (2.21) says that perfect decoupling is achieved when the overall propagators R_+ and R_- are equal over the cycle period t_r. As we mentioned earlier, in the limit of negligible *I-I* interactions the propagators $R_\pm$ assume the same form as the spin-rotation operators. This provides a geometrical interpretation of decoupling even in presence of large heteronuclear dipolar interactions d_{IS} with respect to the chemical shift δ_I. In fact the dynamic of *I*-spin in the α and β S-states can be represented as a motion of two points, $\hat{r}_{I;+}$ and $\hat{r}_{I;-}$ on the surface of unit sphere. From this point a view the relation (2.21) implies that perfect decoupling corresponds to an overlapping of the points $\hat{r}_{I;+}$ and $\hat{r}_{I;-}$ over a cycle period t_r. As a result we can measure the quality of decoupling just calculating the inner product between $\hat{r}_{I;+}$ and $\hat{r}_{I;-}$:

$$\lambda = \hat{r}_{I;+} \cdot \hat{r}_{I;-} = \cos \Phi_{I;\pm} \tag{2.22}$$

As it will be seen in Eq. (2.22) the perfect decoupling corresponds to an angle between $\hat{r}_{I;+}$ and $\hat{r}_{I;-}$ of $\Phi_{I;\alpha\beta} = 0 \pm 2k\pi$ ($k \in \mathbb{Z}$, where $\mathbb{Z}$ is the set of integers numbers).

It is worth noting that the decoupling condition (2.21) requires that only both the end points of the trajectories $\hat{r}_{I;+}$ and $\hat{r}_{I;-}$ must be coincident and not necessarily that these end points coincide with the starting point $\hat{r}_I$, i.e. cyclicity condition (full propagators $U_{\pm} = 1_{op}$) is not a *necessary* condition.

2.3 Effective Hamiltonian and second moment as a decoupling criterion

2.3.1 Effective Hamiltonian

In the case of a periodic perturbation, all physical information about the spectrum is contained in the propagator $U(t_r,0)$. Hence we can calculate an *effective-Hamiltonian*, [9] by diagonalizing the propagator $U(t_r,0)$:

$$U(t_r,0) = \prod_{n=0}^{M} U\left(n\Delta t,(n+1)\Delta t\right) \quad \text{with} \quad M = \frac{t_r}{\Delta t} - 1 \tag{2.23}$$

Where M is the "state" number of the RF-field. The *effective Hamiltonian* is defined by:

$$U(t_r,0) = e^{-iH_{eff}t_r} \tag{2.24}$$

and the explicit calculation is obtained by means of the diagonalization of the propagator $U(t_r,0)$ as follows:

$$e^{-i\Lambda t_r} = V^{-1}UV \tag{2.25}$$

Where the matrix Λ represents the *effective-Hamiltonian* in diagonal form, which elements are obtained by:

$$-i\Lambda_{kk} = \frac{\ln\left(\left|V^{-1}UV\right|_{k,k}\right)}{t_r} \tag{2.26}$$

and the *FID* results:

$$FID(nt_r) = \sum_{ij} \left|A_{i,j}\right|^2 e^{in(\Lambda_{ii}-\Lambda_{jj})t_r} \tag{2.27}$$

where $\left|A_{i,j}\right|^2$ is the transition amplitude between states i and j.

Fourier transform of *FID* given in Eq. (2.27) leads to peaks at the frequencies $\Lambda_{ii} - \Lambda_{jj}$ with intensities of $\left|A_{i,j}\right|^2$, in fact we have:

$$S(\nu) = \int_{-\infty}^{\infty} \sum_{ij} \left|A_{i,j}\right|^2 e^{i(\Lambda_{ii}-\Lambda_{jj})t} e^{-i\nu t} dt = \sum_{ij} \left|A_{i,j}\right|^2 \delta\left[\nu - \left(\Lambda_{ii} - \Lambda_{jj}\right)\right] \tag{2.28}$$

Where the symbol $\delta[\ ]$ indicates the Dirac's delta function, [10].

2.3.2 Another decoupling criterion: second moment M_2

As we know the *FID* can be expanded in a power series of time t with [11] the coefficients given by:

$$M_k = \int_{-\infty}^{\infty} \nu^k f(\nu) d\nu \tag{2.29}$$

The terms M_k's are called moments of the *FID*, and $f(\nu)$ is the spectral intensity. Since $f(\nu)$ is a positive-defined function, the even moments M_{2k}'s are also positive-defined. This suggests that those even moments can be used as a criterion of decoupling. One suitable parameter for this task can be the second moment, which is given by:

$$M_2 = \int_{-\infty}^{\infty} \nu^2 f(\nu) d\nu \tag{2.30}$$

As we have previously shown for a single irradiated I spin the corresponding S-spectrum consists of four peaks at the frequencies $\pm\nu_m$ and $\pm\nu_s$, which are the main

and satellite transitions respectively. Following the results of previously paragraph § 2.3.1 in this case the second moment is:

$$M_2 = \sum_{ij} \int_{-\infty}^{\infty} \nu^2 \left|A_{ij}\right|^2 \delta\left[\nu - \left(\Lambda_{ii} - \Lambda_{jj}\right)\right] d\nu = \sum_{ij} \left|A_{ij}\right|^2 \left(\Lambda_{ii} - \Lambda_{jj}\right)^2$$
$$= 2\nu_m^2 \left|A_{\nu_m}\right|^2 + 2\nu_s^2 \left|A_{\nu_s}\right|^2 \tag{2.31}$$

Since the perfect decoupled *S*-spectrum consists of a single peak at the zero-frequency (centre of *S*-spectrum), the Eq. (2.31) says that the perfect decoupling corresponds to the limits in which $\nu_m \to 0$ and the transition amplitudes of satellite transitions $\left|A_{\nu_s}\right|^2 \to 0$. We should note that the latter requirement could mask the actual efficiency of the decoupling. In fact the contribution to the second moment due to the satellite transition could be quite large even if the contribution from the main transitions is considerably small. This depends on the fact that at RF-field strength, normally used, the absolute frequency $\left|\nu_s\right|$ is quite large, so that even with negligibly weak intensity the satellite transitions can lead to a considerable increasing of the second moment. As a result in using the second moment as a test of decoupling it is usually convenient to remove the contribution from the satellite transitions since small absolute frequency $\left|\nu_m\right|$ corresponds to weak intensity of the satellite transitions.

2.4 Broad Band decoupling

The on-resonance condition is difficult for multi-spins system due to the chemical shift dispersion of the *I*-spin system. The off-resonance irradiation determines one unaveraged component of the effective field causing to different residual couplings in different points of the *I*-spectrum. To obtain an essentially complete decoupling, the amplitude of the irradiating field must be substantially larger of the width of *I*-spectrum. In liquids, employing special techniques decoupling, these conditions yield an effective broad band decoupling with a limited amount of RF power. The situation

is completely different in solids and liquids crystals. In fact, an effective broad band decoupling, because the presence of strong dipolar interactions and large anisotropy of the chemical shift of the *I* spins, would require such a large amount of RF power to give rise to arcing effects on the probe and intolerable heating in liquid crystal samples.

The decoupling with monochromatic RF field is very sensitive to the offset resonance of the RF irradiation, so that many efforts have been done in order to overcome this problem.

Many sequences have been developed to improve the efficiency of the heteronuclear decoupling in liquids. Sequences such as MLEV [12, 13] and WALTZ [14] have given good results in terms of efficiency. The same sequences applied to heteronuclear decoupling in solids do not produce the same good results because of the presence of strong dipolar interactions and of a shielding tensor anisotropy; both effects are comparable with the strength of the RF field. A new generation of multi-pulse sequences based on phase alternate modulation such as TPPM [15] and SPINAL families [16] have improved the efficiency of broad band decoupling in solid and in particular in liquids crystals.

2.5 Analysis of CW *vs.* phase-modulated decoupling

So far we have shown the basic idea of decoupling without analysing any specific case. The aims of this section would be that of understanding the influence of various parameters involved in the decoupling process. Unfortunately this is a hard task, since no analytical methods available give simple results to handle and numerical simulations of the entire spin system can be very difficult, or even impossible. At the moment the only strategy possible is that of combining numerical simulations, based spin-system modelling, with a large set of experimental data. The drawback of this method resides on the fact the validity conclusions, based on the numerical simulation, may be strongly related to the spin-model adopted. However, in order to understanding more about of decoupling we simulated the performance of two

different decoupling sequences, continuous wave (CW) and SPINAL-64. Unlike CW the SPINAL scheme involves phase-modulation of the RF-field. This modulation consists of a combination of the elements Q and $\bar{Q}$ which in turn consist of alternating pulses, $Q = \tau_P(\phi_k)$ and $\bar{Q} = \tau_P(-\phi_k)$, where τ_P is a short pulse of about 170°, and $\pm\phi_k$ are the small phase angles of RF-field.

$$Q = \tau_P(10)\tau_P(-10)\tau_P(15)\tau_P(-15)\tau_P(20)\tau_P(-20)\tau_P(15)\tau_P(-15)$$

$$\bar{Q} = \tau_P(-10)\tau_P(10)\tau_P(-15)\tau_P(15)\tau_P(-20)\tau_P(20)\tau_P(-15)\tau_P(15)$$

In order to understand the performance of the decoupling sequences, we have calculated the second moment of *S*-spectrum as a function of the *I*-spin offset and dipolar-coupling constant, d_{SI}, in both *S*-*I* and *S*-I_2 spin systems. The contour plots of Figure 2.2 illustrate the results of the simulation of CW decoupling. On both *S*-*I* and *S*-I_2 systems, we observe that, given any value of the coupling constant, d_{SI}, the second moment M_2, and so the performance of CW decoupling largely dependent on the *I*-spin offset. This means that the performance of CW decoupling is strongly dependent from the *I*-spin offset irradiation. Comparing the simulations of the *S*-*I* and *S*-I_2 (see Figure 2.2) what we note is that for relatively small values of d_{SI} coupling the presence of *I*-*I* interaction makes more drastic the dependence of second moment from the *I*-offset. However, as the dipolar coupling d_{SI} increases for a particular interval of its values the second moment is relatively small values despite large deviations from the on-resonance condition. Moreover the impact of the *I*-*I* interaction on heteronuclear decoupling is also dependent on the decoupling scheme. As we can see in the simulations of Figure 2.3 the SPINAL decoupling shows that the influence of homonuclear interactions is more effective with respect to the CW decoupling, in the sense that the second moment is minimized in a wider region of the offset- d_{SI} plane. Moreover it is worth noting that in both *S*-*I* and *S*-I_2 spin systems the SPINAL decoupling gives a better performance than CW. This is clearly visible by comparing the simulations of Figure 2.2 and Figure 2.3, where is shown that the second moment corresponding to the SPINAL is of about an order of magnitude less

than the second moment observed for CW decoupling. These theoretical results are in qualitative agreement with the experimental observations on 5CB liquid crystal [15] (for the molecular structure see Figure 2.4). The Figure 2.4 illustrates the ^{13}C-spectra of 5CB in the nematic with CW and SPINAL ^{1}H-decoupling.

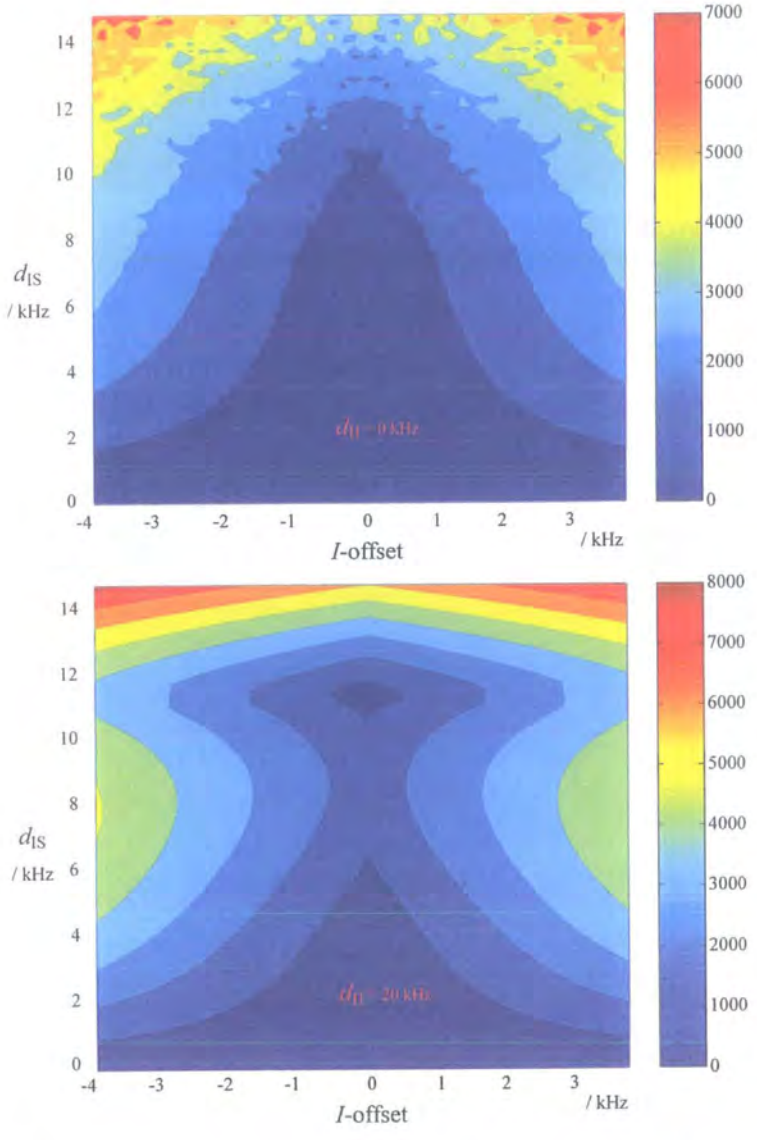

Figure 2.2 Contour plots of the second moment M_2 as function of I-spin offset irradiation and dipolar coupling constant d_{IS}. CW decoupling was applied with RF-power of 50 kHz. At the top the homonuclear dipolar coupling constant was set to zero (S-I system), while on the bottom it was set to 20 kHz (S-I_2 system). The calculation of the second moment M_2 includes all the transitions. The simulations were performed with MATLAB and the code is given in the appendix.

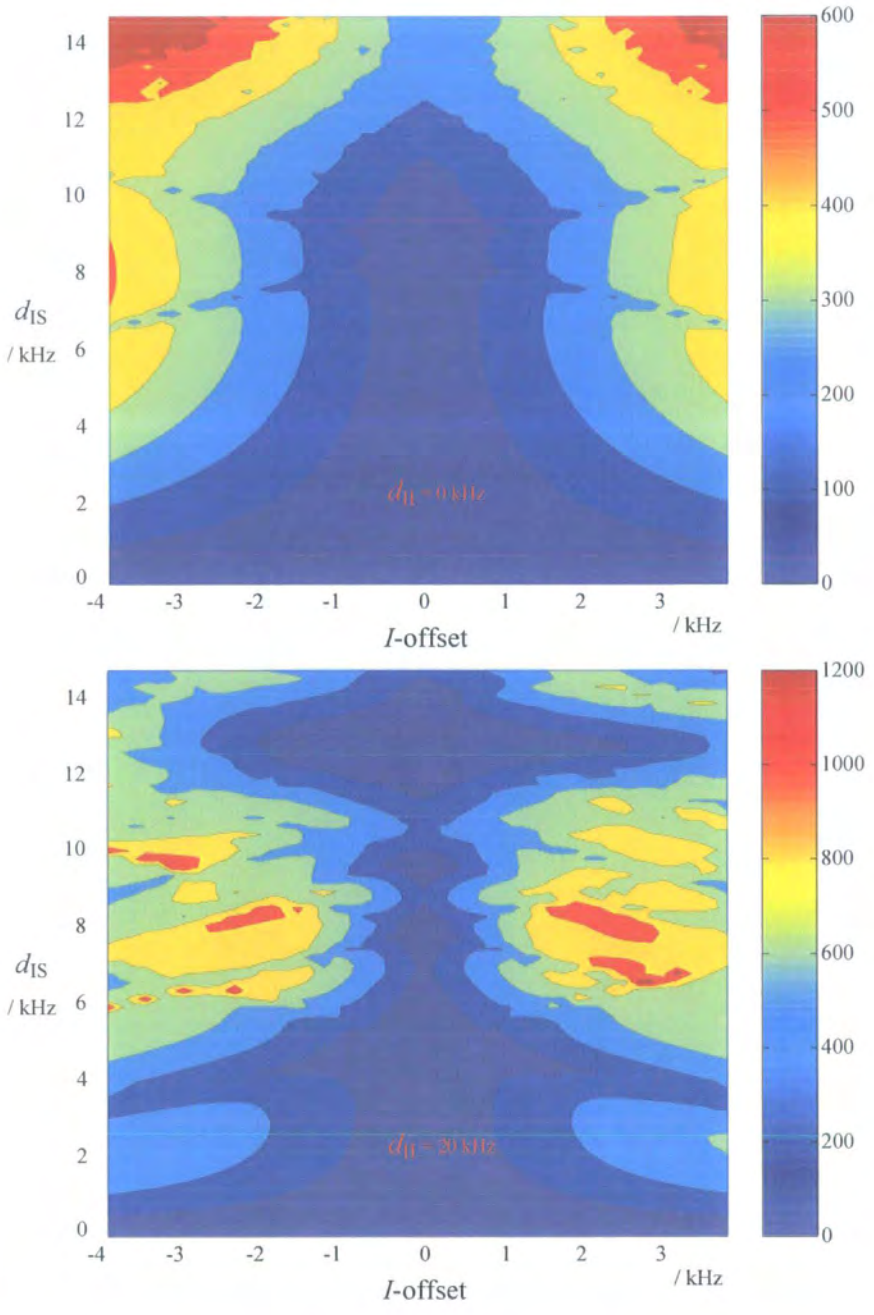

Figure 2.3 Equivalent contour plots of **Figure 2.2** for SPINAL-64 decoupling with a tip angle $\beta = 170^{\circ}$.

As it will be seen SPINAL decoupling leads to a well-resolved ^{13}C-spectra over the entire bandwidth, whereas the CW decoupling shows well-resolved aromatic carbons with a drastic broadening for the carbons in aliphatic region.

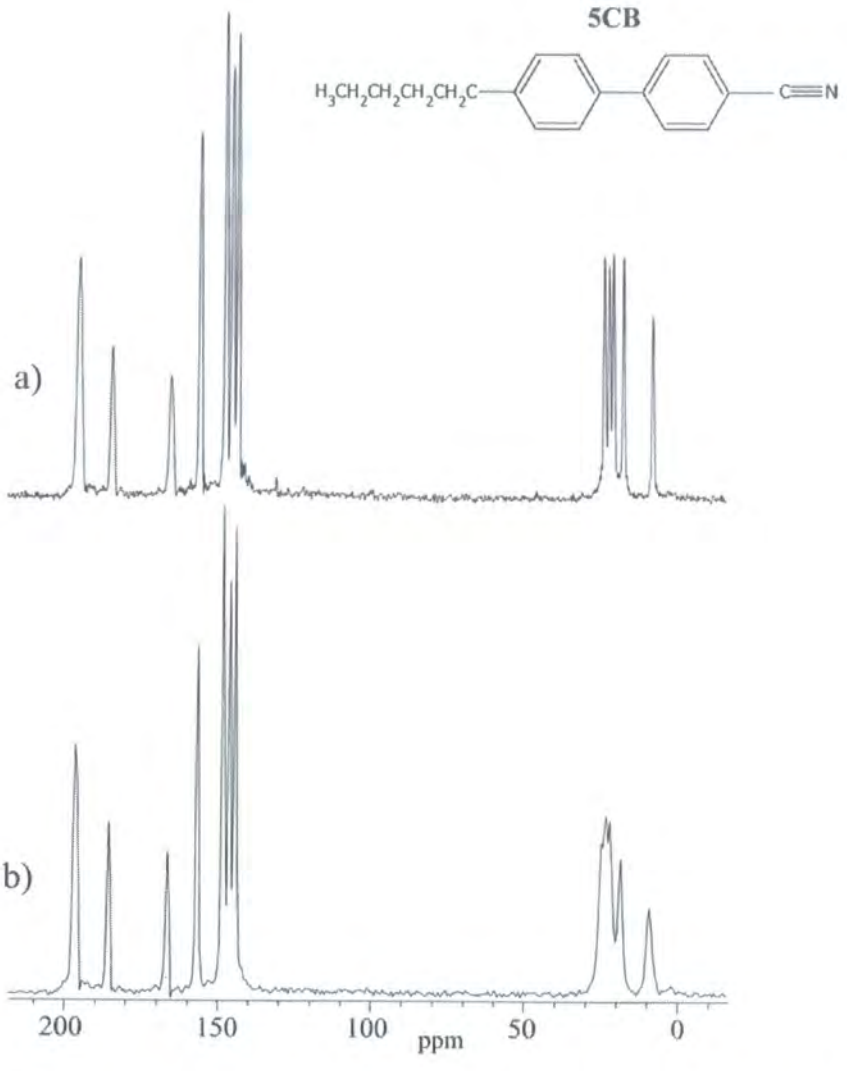

Figure 2.4 CP ^{13}C-spectra of 5CB in nematic phase at 30° C with various ^{1}H decoupling schemes: a) SPINAL-64 with a tip angle β of about 170°. b) CW decoupling. The experimental parameters are: ^{1}H-frequency, 200 MHz, contact time 3ms, recycles delay, 8 s and decoupling power 50 kHz.

In both experiments the ^{1}H-transmitter frequency was set in the middle point of ^{1}H-spectrum of 5CB. Nevertheless this setting does not necessarily correspond to the best decoupling performance. As a result a further optimisation of this frequency can yields to a substantial improvement of the decoupling performance, as occurs for SPINAL sequence. However this is not the case for CW decoupling, since a deviation ^{1}H-transmitter frequency from the centre of the ^{1}H-spectrum we may recover a better resolution for aliphatic carbons and a consequent loss of resolution for carbons in the aromatic region. Nevertheless holding the same ^{1}H-transmittter frequencies for both decoupling schemes, above mentioned, one can compare their response with respect to the same set of *I*-spin offset irradiations. The 5CB liquid crystal can be seen as, approximately, formed by two different kinds of spin systems, C—H and C—H_2, respectively for the aromatic and aliphatic carbons. As it will be noticed in Figure 2.4 the CW performance is much worse for those carbons where the influence of the *I-I* interactions is stronger, i.e. in the aliphatic region. On the other hand this effect is also reproduced through the simulations. In fact they show that exists particular range of dipolar couplings d_{IS} for which the *I-I* interactions [17] make the CW decoupling more sensitive from the *I*-spins offset irradiation. This can explain why the resonances of aromatic carbons are relatively well resolved in comparison with those of aliphatic carbons. The ^{13}C-spectrum with SPINAL decoupling reflects the simulations as well. The observed good resolution over the entire bandwidth is in agreement with the simulations, which show that the SPINAL decoupling is more robust to the off resonance irradiation effects, even including the *I-I* interactions.

In ending this brief discussion about of decoupling analysis may be useful to give some detail more about the role of homonuclear interactions in heteronuclear decoupling. The flip-flop term of Homonuclear Hamiltonian induces a flip-flop "motion" of the abundant *I*-spins (say, ^{1}H) and like the lattice motions and so averaging the *S-I* heteronuclear interactions. In the limit of very fast *I*-"spin diffusion" ($d_{II} \gg d_{IS}$), we observe a drastic quenching of heteronuclear interactions resulting in a narrowing of *S*-spin resonances. This effect has been observed

experimentally, e.g. in ^{13}C-spectra of adamantane [18]. "Freezing " the I-spin fluctuation by means of homonuclear decoupling (Lee-Goldburg experiment, [19, 20]) results in an increase of the S-spin linewidth. This effect is the so-called self-decoupling, or even incoherent decoupling. We notice that the self-decoupling phenomenon usually involves many spins that are interacting with each other and phonon-coupled to the lattice as well. The presence of these multi-body interactions introduces a statistical or thermodynamic aspect on the self-decoupling.

At the first sight one could argue that the I-spin flip-flop always motion helps the heteronuclear decoupling. As demonstrated above through both simulations and experiment this is not true. It is generally accepted in high-resolution solid state NMR that the decoupling field, to be efficient, must overcome not only the heteronuclear couplings, but also homonuclear interactions. However simulations on a simple S-I_2 spin system have demonstrated that even if such condition is satisfied, the influence of homonuclear interactions in heteronuclear decoupling strongly depend upon the relative size of heteronuclear and homonuclear couplings in combination with time modulation of decoupling field.

2.6 Conclusion

In this Chapter we have shown the basic aspects of decoupling theory. In particular we pointed out the relevant differences between decoupling in liquids and decoupling in solids and liquid crystals. Decoupling criteria derived for liquids does not apply for solids or liquid crystals. As a result we proposed more general criterions useful not only in designing new sequences, but also to some extent, for a more profound understanding of decoupling itself.

CW together with MAS remains the most used decoupling method for solids, giving reasonable spectral resolution in most of solid samples. On the other side decoupling sequences, such as WALTZ, provide an efficient broadband decoupling in liquids.

In liquid crystals the situation is slightly different because of large anisotropy of tensor interactions, not averaged out by MAS, makes the decoupling difficult. An essential broadband decoupling can be obtained to a certain extent employing a relatively large amount of RF power. On the other hand this can lead to the sample heating, which result in a degradation of spectral resolution. For these reasons further investigations of decoupling of liquid crystals in Chapter 4 will be given. In particular we will show a large set of experimental data in parallel with numerical simulations of the results obtained emphasising the relevant aspects of some decoupling sequences.

References

1. R. Freeman: Spin choreography. Basic Steps in High Resolution NMR, *Oxford University Press* (1998), Chapter 7.
2. Z. Gan, R. R. Ernst, *Solid State Nuclear Mag Res* **8**, 153-159 (1997).
3. J. S. Waugh, *J. Mag. Res.* **50**, 30-49 (1982).
4. M. Edén, Y. K. Lee, M. H. Levitt, *J. Mag. Res.* **120**, 56-71 (1996).
5. A. D. Bain, R. S. Dumont, *Concepts in Magn. Reson.* **13 (3)**, 159-170 (2001).
6. U. Haberlen, J. S. Waugh, *Phys. Rev.* **175**, 453-467 (1968).
7. E. Wab, *Ann Phys* **48**, 72 (1968).
8. R. R. Ernest, G. Bodenhausen, A. Wokaun: Principles of Nuclear Magnetic Resonance in one and two dimensions, *Oxford University Press, London* (1987), pp. 232-235.
9. T. S. Untidt, N. C. Nielsen, *Phys. Rev. E* **65** (2002).
10. M. G. Arfken: Mathematical methods for Physicists, *3rd. ed., Academic Press, New York* (1985).
11. M. Mehring: Principles of High Resolution NMR in Solids, *Springer-Verlag, Berlin* (1983), Chapter 2.
12. M. H. Levitt, R. Freeman, Frenkiel, *Advances in Magnetic Resonance (J. S. Waugh, Ed.), Accademic Press, New York* **11**, 47 (1983).
13. M. H. Levitt, R. Freeman, *J. Mag. Res.* **43 (3)**, 502-507 (1981).
14. A. J. Shaka, J. Keeler, T. Frenkiel, R. Freeman, *J. Mag. Res.* **53 (2)**, 313-340 (1983).
15. Y. Yu, B. M. Fung, *J. Mag. Res.* **130**, 317-320 (1998).
16. B. M. Fung, A. K. Khitrin, K. Ermolaev, *J. Mag. Res.* **143**, 97-101 (2000).
17. K. Schmidt-Rohr, H. W. Spiess: Multidimensional Solid-State NMR and Polymers, *Academic Press, London* (1994), pp.18-20.
18. M. Ernst, A. Verhoeven, B. H. Meier, *J. Mag. Res.* **130**, 176-185 (1998).
19. M. Lee, W. I. Goldburg, *Phys. Rev. Lett.* **11 (6)**, 255 (1963).
20. M. Lee, W. I. Goldburg, *Phys. Rev. Lett.* **140 (4A)**, 1261 (1965).

Chapter 3

Liquid Crystals

3.1 Introduction to liquid crystalline phase

In this chapter a brief outline of liquid crystal materials it will be given. Reinitzer discovered liquid crystals in 1888. He found that one substance changed from a clear liquid to a cloudy liquid before crystallising and he suggested that this cloudy fluid was a new phase of matter. The liquid crystalline phase is an intermediate state of the matter between solid and liquid. In the (crystalline) solid state there exists a rigid arrangement of molecules, which stay in a fixed position and orientation with a small amount of variation from molecular vibration. So that the solid crystals are characterize by a long-range positional order, and in case of anisotropic molecules there will be an additional long-range orientational order. In the liquid phase the molecules have no fixed position or orientation and are free to move in a random fashion, so that neither positional order nor orientational order are expected.

Starting from the crystalline phase and going through the liquid phase it is evident that not necessarily both type of order (positional and orientational) disappear at same melting point [1, 2]. In fact there are two different possibilities:

1. *Plastic crystalline phases*, where the positional order is still present, but the orientational order has disappeared or is strongly reduced.
2. *Liquid crystalline phases*, in which the orientational order is still present, while the positional order is strongly reduced or even entirely lost.

The *liquid crystalline phase*, or even called *mesophase*, is dived into wide categories: *thermotropic* and *lyotropic*. The distinction between them is that the thermotropic mesophase is temperature-dependent, while the lyotropic mesophase exhibits concentration phase behaviour. The thermotropic mesophase is achieved a within

well-defined range of temperature between solid and liquid phases, and those liquid crystals are one-component systems. By contrast the lyotropic liquid crystals require a solvent (e.g., water) plus the liquid crystalline solute and the variation of the concentration of the solution results the dominating aspect in order to achieve the *mesophase*. We will restrict ourselves to study thermotropic liquid crystals rather than lyotropic one. This is because in this work most of the experiments were performed on thermotropic liquid crystals and also because they are more interesting for physical and commercial applications. In both categories of the liquid crystals, *lyotropic* and *thermotropic*, the techniques to investigate the structure of the *mesophase* are the same, e.g. Polarising Microscopy, X-ray diffraction, NMR (Nuclear Magnetic Resonance), DSC (Differential Scanning Calorimetry). In the next section it will be examined several types of thermotropic liquid crystals' mesophase whose structures differ for various orientational and positional molecular arrangement.

3.2 Calamitic liquid crystals: Different types of mesophase

As mentioned earlier the liquid crystalline phase shows several types of molecular arrangements. The molecular shape influences the structure of the mesophase, so that calamitic, or rod-shaped, molecules form nematic and smectic phases. Smectic liquid crystals are further classified into smectic S_A, S_B, S_C etc, depending upon the molecular arrangement within and between the layers formed by the molecules in the mesophase. Molecules forming a typical calamitic mesophase consist of a rigid core, mostly aromatic, with flexible side chains. The rigid core provides the anisotropic character of the mesophase, while the side chains ensure stability of the orientational ordering.

3.2.1 Calamitic nematic phase

The nematic phase occurs in those substances that have usually rod-like shape molecules and it is characterize by a complete loss of positional order at melting point, so that the centres of mass of the molecules have translational symmetry as in

isotropic liquids. However by decreasing the temperature from isotropic phase, where the molecules are randomly positioned and oriented, to the nematic phase the material gains an amount of orientational order. Due to the rod-shape of the molecules and molecular forces between them, the nematic phase consist of molecules preferentially line up to each other but randomly distribute in the space.

The orientational order allows us to define an average direction of the molecules called the director [3, 4] denoted by the unit vector $\vec{n}$. To be more precise the director is a unit vector field $\vec{n}(\vec{r})$, which defines the local orientation of the molecules at the point $\vec{r} \equiv (x, y, z)$ and varies continuously across of the oriented material. The states of local direction of alignment described by $\vec{n}(\vec{r})$ and $-\vec{n}(\vec{r})$ result indistinguishable, which means that the nematic phase is *apolar*. Moreover the nematic phase shows a rotational invariance around the direction individuates by the vector field $\vec{n}(\vec{r})$, which is equivalent to state that the nematic phase is *uniaxial*. Generally the local domain of orientation extends even for several millions of molecules, but we can achieve a macroscopic alignment of the local director when the material is subject to an external field. This occurs for instance in a NMR experiment where the local director results fully aligned along the direction of static magnetic field giving rise to a macroscopic *uniaxial* nematic phase. In Figure 3.1 is given a schematic representation of a nematic phase.

Figure 3.1 Schematic representation of a nematic phase.

As seen above the director describes locally an average direction of the molecules. However in order to establish the degree of molecular alignment around the local director, $\vec{n}(\vec{r})$, is necessary to introduce another important variable, the so-called *order parameter.*

3.2.2 Nematic order: Microscopic approach

We start with the assumption that the molecules are rigid rods and cylindrical symmetric around their long axis, so that we can identify the orientation of the single molecule with a unit vector $\vec{\xi}$, as graphically represented in

Figure 3.2. Without loss of generality we assume that the z-axis of our laboratory frame, $O(x,y,z)$, coincident with the direction of the director $\vec{n}$. The degree of the alignment of the road-like molecules can be specified by an orientational distribution function $f(\Omega)d\Omega$ [5, 6], which gives the probability of finding a molecule in a small solid angle $d\Omega = \sin\theta d\theta d\varphi$ with a particular orientation $\Omega = (\theta,\varphi)$, where θ and φ are the polar angles corresponding to $\vec{\xi}$. As before explained the nematic phase has the properties to be invariant for rotation about the director axis and also that the directions $\vec{n}(\vec{r})$ and $-\vec{n}(\vec{r})$ are equivalent, for which we must require that the orientational distribution function $f(\theta)$ fulfils to the following conditions:

3. $\dfrac{\partial f(\theta,\varphi)}{\partial\varphi} = 0 \quad \varphi \in [0,2\pi]$ (*Rotational invariance of nematic phase around the director axis*).
4. $f(\theta) \equiv f(\pi-\theta) \quad \theta \in [0,\pi]$ (*The orientations described by* $\vec{n}(\vec{r})$ *and* $-\vec{n}(\vec{r})$ *appear to be indistinguishable*).

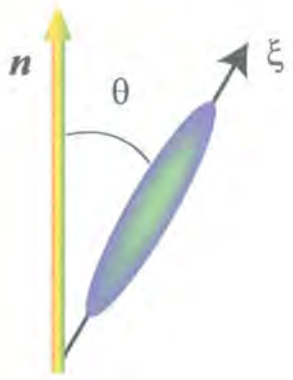

Figure 3.2 Graphic representation of rod molecule with the long axis $\vec{\xi}$ oriented at an angle θ relatively to the direction determined by the director $\vec{n}$. Due to the rotational invariance of nematic phase around the director axis and molecular cylindrical symmetry the orientation of the molecule is specified only by the polar angle θ.

Since the orientational distribution function $f(\theta)$ cannot be entirely known we characterize the molecular alignment by using quantities related to it. To this the only thing we can do is to expand $f(\theta)$ in a series of θ. An appropriated ortonormal bases set is given by the Legendre's polynomials for which we can write $f(\theta)$ as follows [3, 7]:

$$f(\theta)=\frac{1}{2}+\frac{5}{2}\langle P_2\rangle P_2\left(\cos(\theta)\right)+\frac{9}{2}\langle P_4\rangle P_4\left(\cos(\theta)\right)+..... \tag{3.1}$$

From the property (4) the multipole expansion (3.1) all the odd terms vanish, so that the first non-trivial component to use as order parameters is the quadrupolar term $\langle P_2\rangle$:

$$S^{zz}=\langle P_2\rangle=\frac{1}{2}\left\langle\left(3\cos^2\theta-1\right)\right\rangle=\int_0^{\pi} f(\theta)\frac{1}{2}\left(3\cos^2\theta-1\right)d\Omega \tag{3.2}$$

Effectively the term $\langle P_2 \rangle$ contains information about the molecular alignment. In fact if $f(\theta)$ represents a system strongly orientated, which means that it is non-zero only around the orientations $\theta = 0$ and $\theta = \pi$ (fully alignment of the molecules), from the Eq (3.2) we obtain $S^{zz} = 1$. On the other hand if the $f(\theta)$ is non-zero around the orientation $\pi/2$ we obtain $S^{zz} = -1/2$, while under condition of random molecular orientation the order S^{zz} vanishes. The same behaviour is extended to the other terms $\langle P_N \rangle$ defining higher order parameters. In particular the term $\langle P_2 \rangle$, i.e. S^{zz}, represents second rank order parameter in the series expansions of $f(\theta)$.

The molecular reordering in isotropic-nematic phase transition is thought to be due to an orientational pseudo-potential $V(\Omega)$, so that the orientational distribution function $f(\theta)$ can be written as follows [5]:

$$f(\Omega) = \frac{1}{Z} \exp\left[-\beta V(\Omega)\right] \tag{3.3}$$

Where $\beta = 1/k_B T$, (k_B, Boltzmann's constant) and Z is the partition function:

$$Z = \int_{\Omega} d\Omega \exp\left[-\beta V(\Omega)\right] \tag{3.4}$$

It is important to note that the potential torque $V(\Omega)$, in Eq. (3.3), results the orientational energy of a single molecule. As seen in the Eq. (3.3), the orientational distribution function $f(\Omega)$ results strongly dependent on the thermal energy $k_B T$. As a result the order parameter S^{zz} is highly dependent on the temperature of the sample. Figure 3.3 displays a typical order parameter *vs.* temperature relationship. We note the discontinuity at temperature T_C of the phase transition between the liquid crystal and liquid states. At this temperature the thermal energy $k_B T_C >> V$, so that from Eq. (3.3) we see that all orientations Ω become equally distributed.

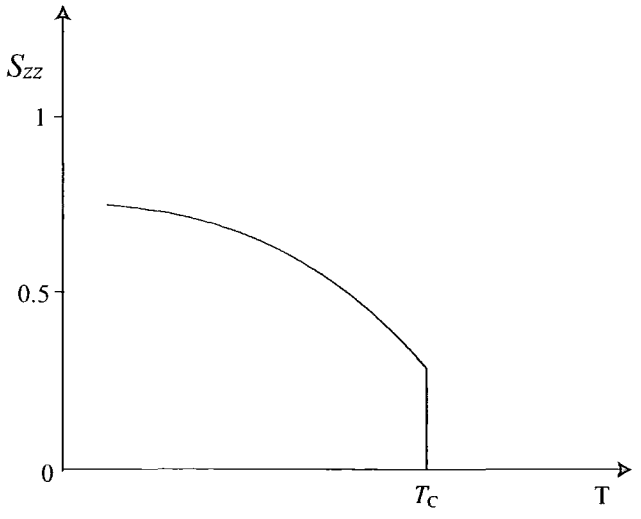

Figure 3.3 Order parameter S^{zz} *vs.* temperature for a typical liquid crystal. T_c is the temperature of transition between the liquid crystal and liquid state.

3.2.3 Calamitic chiral nematic

The chiral or chiral mesophase is a special case of nematic phase. When the rod-like molecules that form the liquid crystalline phase are chiral (i.e. they are not symmetric when reflected) the normal nematic phase is replace by a chiral nematic one. Due to the chirality of the molecules constituting the mesophase, in addition to the long-range orientational order there is a spatial variation of the director leading to a helical structure. In other words the molecules prefer to lie next to each other in a slightly skewed orientation leading to the formation of a structure, which can be visualized as a stack of very thin 2-D nematic-like layers with the director in each layer twisted with respect to those above and below. This is illustrated in
Figure 3.4. However it is important to note that the molecular arrangement, shown in Figure 3.4, is referred to an instant in time, which means that rapid and random positional motion is taking place.

In a large volume compared to the molecular dimension, the director, $\vec{n}(\vec{r})$, rotates following a helical configuration and the full director rotation is achieved over a distance p, called the *pitch*. Since the directions $\vec{n}(\vec{r})$ and $-\vec{n}(\vec{r})$ are still indistinguishable the actual spatial repetition period of the structure is $p/2$. The pitch

is an important physical parameter from which depend the optical properties of the chiral mesophase. In fact for instance the wavelength of reflected light depends on the pitch length.

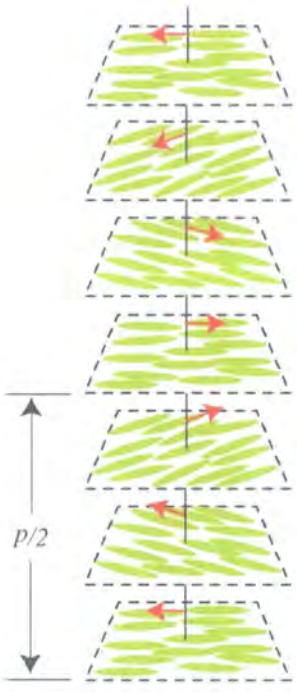

Figure 3.4 Artist view of chiral mesophase. The arrows represent the director following a helical trajectory. In each thin layer the molecules form a 2-D nematic arrangement. Due to the equivalent molecular orientation $\vec{n}$ and $-\vec{n}$ the helical structure is repeated at half pitch $p/2$

In particular the light will be reflected only when its wavelength matches the pitch length. This property is very important for the applications. In fact by changing the temperature we can modify the relative angle of the director between two successive layers, as a result the pitch length will result varied as well. This makes it possible to build a liquid crystal thermometer that displays the temperature of its environment by the reflected colour (monochromatic electromagnetic wave).

Another important physical property is that applying an electric field can modify the helical structure. This is due to the interaction between the electric dipole of the molecules and electric field. The result of this interaction is that the director tends to align along the electric field, so that the helical structure can be stretched or even

fully destroyed. This property is exploited in building the modern display device (LCD), [8-10].

3.2.4 Calamitic smectics

Decreasing the temperature below the nematic phase some liquid crystals can gain a certain amount of positional order. When this occurs we say that the liquid crystals form a smectic phase. Although the smectic phase is still fluid the molecules prefer to lie on average in layers. Within the layers the molecules are preferably pointing in one direction, so that the molecular ordering is essentially as that of a 2-dimesional nematic liquid crystals. However based on different molecular arrangements within the layers there are several types of smectic phases. The most important ones are the smectic-A and the smectic-C [4]. When the nematic-like director is oriented as the normal layer (see

Figure 3.5-(a)) the mesophase is called smectic-A, while if this director tilts away from the layer normal (see

Figure 3.5-(b)) the liquid crystal is in a smectic-C phase.

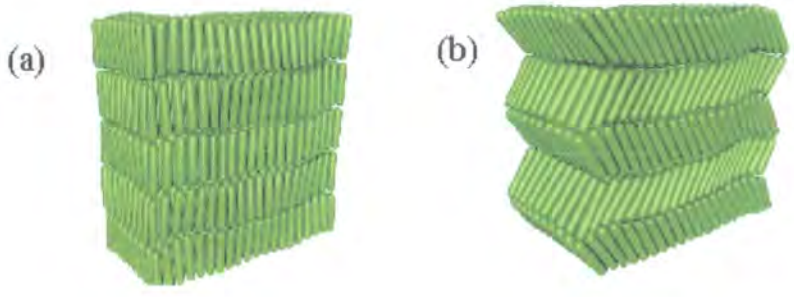

Figure 3.5 Idealized view of two different smectic phases. In (a) is sketched a smectic-A phase with the nematic-like director in the same direction of the normal layer, while in (b) smectic-C phase the director inclined with respected to the normal layer direction.

Smectic materials can also exhibit an additional positional ordering of the molecules within the layer, so that the resulting phase, smectic C, produces a higher symmetry in comparison with the smectic A and B phases.

Similarly to the chiral nematic phase the smectic ordering can form a chiral molecular arrangement denoted by smectic C*. The tilted director of the smectic-C phase is now rotated between the layers forming a helical structure. It is important to remember that many other smectic phase have been identified, more than 10. However we restricted our self at most important ones in order to emphasise the relevant difference with respect to the nematic phases.

3.3 Discotic liquid crystals

In this section a very brief description of discotic liquid crystals will be given. These materials potentially can form nematic and chiral nematic mesophase as in calamitic liquid crystals. Nevertheless due to the particular global shape of the molecules usually a columnar molecular assembling is formed. The molecules are disc-shaped consisting of a rigid flat core surrounded by flexible side chains. As in calamitic liquid crystals the core is usually aromatic. The molecular disc-shape is ensured by both symmetric geometry of the core and suitable number of side chains.

3.3.1 Columnar discotic phase

In columnar mesophase the molecules are aligned in columns. The different arrangement of these columns can be classified as hexagonal (h), rectangular (r), or oblique (ob), moreover the molecular assembling within the columns can be ordered (o), or disordered (d). According to the relative orientation between the columnar axis and director axis the columnar arrangement can be orthogonal or tilted. The molecules assembled into orthogonal columns hexagonal packed form a uniaxial phase. The symbols D_{ho} and D_{hd}, which mean hexagonal ordered and disordered respectively usually denoted these phases. The tilted phases D_{rd} and $D_{ob,d}$, which mean rectangular and oblique disordered respectively, are instead optically biaxial.

As an example the

Figure 3.6 shows an idealised representation of an orthogonal columnar mesophase D_{ho}.

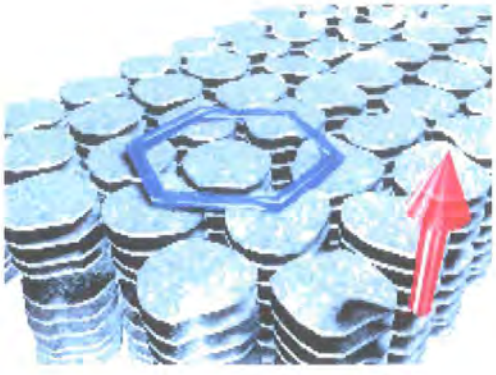

Figure 3.6 Artist view of a columnar phase D_{ho}. The orthogonal columns are arranged to form a hexagonal structure, while the molecular assembling within the columns is disordered. The arrow is showing the direction of the columnar axis, which is in this case coincident with the direction of director axis.

Unlike calamitic liquid crystals the discotic ones at the moment are not employed in building displays (LCD). Nevertheless the columnar mesophase exhibit very special physical properties. One the most important is the anisotropy in conductivity between directions along the columnar axis with respect to that orthogonal. This directional dependent conductivity is due to the particular geometry of columnar mesophase, which enables one-dimensional transport of charge within the columns and an insulating effect by the flexible on the orthogonal direction with respect to the columnar axis.

3.4 NMR of Liquid Crystals

In order to understand the mechanisms that govern the formation of the liquid crystal phase, knowledge of how the orientation of the molecules is coupled with their

conformational degree of freedom is required. Nuclear magnetic resonance (NMR) represents an important instrument to investigate oriented systems such as LC's. Since NMR spectroscopy probes local structure and dynamics (atomic level), it can give detailed information about molecular geometry, average orientation and internal dynamics, [11-15]. The *dipole-dipole interaction*, between magnetic nuclei such as ^{13}C and ^{1}H, contains information on the orientational distribution and the structure of the molecules in the mesophase. The strength of the dipolar interaction between the spins depends on both the size of the internuclear vector $\vec{r}_{ij}$, and by its relative orientation with respect to the static magnetic field:

$$D_{i,j} = -\frac{\mu_0 \hbar \gamma_i \gamma_j}{4\pi^2} \frac{1}{2} \frac{3\cos^2 \theta_{ij} - 1}{r_{i,j}^3} \tag{3.5}$$

Here μ_0 is the permeability in vacuum, $\hbar$ is the Planck's constant, $r_{i,j}$ is the inter nuclear distance, θ is the angle between the magnetic and the internuclear-vector $\vec{r}$ connecting the nuclei *i* and *j*. In a liquid crystalline phase the dipolar interaction is partially averaged and can be written as:

$$\left\langle D_{i,j} \right\rangle = -\frac{\mu_0 \hbar \gamma_i \gamma_j}{4\pi^2} \frac{1}{2} \left\langle \frac{3\cos^2 \theta_{ij} - 1}{r_{i,j}^3} \right\rangle \tag{3.6}$$

The quantity within the angular brackets is the average taken over all molecular motions. If there is no correlation between the internuclear distance r_{ij} and the term $\left\langle 3\cos^2 \theta_{ij} - 1 \right\rangle$, Eq (3.6) becomes:

$$\left\langle D_{i,j} \right\rangle = -\frac{\mu_0 \hbar \gamma_i \gamma_j}{4\pi^2} \frac{1}{2} \frac{\left\langle 3\cos^2 \theta_{ij} - 1 \right\rangle}{\left\langle r_{i,j}^3 \right\rangle} \tag{3.7}$$

For rigid molecules the quantity $\left\langle r_{ij}^{\,3} \right\rangle$, in Eq. (3.7) is coincident with $r_{ij}^{\,3}$. However the difference between the cubic distance $r_{ij}^{\,3}$ and its averaged value is often quite small, so that the averaging of the internuclear distance r_{ij} can be safely ignored.

In Eq. (3.7) $\langle D_{i,j} \rangle$ is the averaged strength of dipolar interaction, which is determined from NMR spectra. Because the nematic director orients along the magnetic field, the strength of dipolar interaction is directly related to the order parameter $S_{i,j}^{zz}$.

$$\langle D_{i,j} \rangle = -\frac{\mu_0 \gamma_i \gamma_j \hbar}{4\pi^2} S_{i,j}^{zz} \frac{1}{r_{i,j}^3}$$

with

$$S_{i,j}^{zz} = \frac{1}{2}\langle 3\cos^2\theta - 1 \rangle$$

The quantity $S_{i,j}^{zz}$ is the order parameter of the axis passing through i and j nuclear positions with respect to either the director axis or the applied magnetic. The possibility of determining the order parameters of the molecular segments from diluted NMR spectroscopy is limited by the complexity of the spectra. This complexity derives from the dipolar coupling between diluted ^{13}C and abundant ^{1}H spins, also for small molecules.

For these reasons the application of NMR spectroscopy to study the liquid crystal materials depends upon the possibility of 'selecting' the interactions through spin decoupling (see Chapter 2) and of separating the interactions with SLF techniques (Separated Local Fields, see Chapter 6).

References

1. G. W. Gray: Thermotropic Liquid Crystals, *Wiley*, (1987), Chapter 1.
2. P. J. Collings and M. Hird: Introduction to Liquid Crystals: Chemistry and Physics, *published by Taylor and Francis* (1997), Chapter 9.
3. J. W. Emsley: Nuclear Magnetic Resonance of Liquid crystals, *NATO ASI Series* (1983).
4. G. Vortogen, W. D. Jeu: Thermotropic Liquid Crystals: Fundamentals, *Springer-Verlag* (1988).
5. R. Y. Dong: Nuclear Magnetic Resonance of Liquid Crystals, *Springer Verlag* (1997), Chapter 3.
6. J. Courtieu, J. P. Bayle, B. M. Fung, *Progress in NMR Spectroscopy* **26**, 141-169 (1994).
7. J. W. Emsley, J. C. Lindon: NMR Spectroscopy using Liquid Crystalline Solvents, *Pergamon Press* (1975).
8. P. G. de Gennes, a. J. Prost: The Physics of Liquid Crystals, *OUP,2nd edition* (1993), Chapter 1 and Chapter 5.
9. I. Khoo and S. Wu: Optics and Nonlinear Optics of Liquid Crystals, *World Scientific Publishing* (1992).
10. V. G. Chigrinov: Liquid Crystal Devices, *Adtech Book Co Ltd* (1999), Chapter 2.
11. T. Nakai, S. Miyajima, Y. Takanish, S. Yoshida, A. Fukuda, *J. Phys. Chem. B* **103**, 406-416 (1999).
12. B. M. Fung, J. Afzal, T. L. Foss, M.-H. Chau, *J. AM. Chem. Phys* **85**, 4808-4813 (1986).
13. Min Zhou, V. Frydmann, L. Frydman, *J. AM. Chem. Soc* **120**, 2178-2179 (1998).
14. J. M. Polson, E. E. Burnell, *J. AM. Chem. Phys* **103(16)**, 6891-6902 (1995).
15. M. L. Magnuson, B. M. Fung, M. Schadt, *Liquid Crystals* **19(3)**, 333-338 (1995).

Chapter 4

Line splitting and broadening effects from ^{19}F in ^{13}C-NMR of liquid crystals

4.1 Introduction

NMR is one of the most important experimental tools to investigate the liquid crystalline phase. Understanding such phases requires knowledge of both molecular conformation and molecular orientations. This can be accomplished using NMR methods, which are sensitive to the molecular geometry, average orientation, and internal dynamics. In the NMR of spin-1/2, nuclei, such as ^1H, the dipolar interactions provide information, about spin-spin distances and orientation between the external magnetic field and internuclear vectors. However the large number of ^1H—^1H couplings makes the ^1H-spectra difficult to analyse, even in relatively small molecules [1]. ^1H-spectra can be simplified by the isotopic dilution of protons, i.e. by partial replacement deuterium nuclei. This procedure indeed reduce the number of ^1H—^1H couplings but selective or random deuteration of the samples can be difficult; moreover it can create problems in the peak assignment and deuterium decoupling. Recently Ciampi *et al.* [2] have demonstrated that in mono-fluorinated liquid crystal samples, such as I35 (for the molecular structure see Figure 4.1) , a set of dipolar couplings d_{ij}^{CF} can be sufficient to investigate molecular conformation and ordering. The success of this method resides in the accurate determination of dipolar couplings d_{ij}^{CF} from ^1H-decoupled ^{13}C-spectra. The major problems encountered by Ciampi *at al.* in studying for instance I35, were indeed the effectiveness of ^1H-decoupling over the entire ^1H-band width. They found out that was not possible to resolve C—F splitting for aliphatic and aromatic carbons simultaneously with a single decoupling

sequence. In particular they achieved very well resolved carbon lines in the aromatic region by using COMARO-2 [3] decoupling scheme with an almost complete loss of resolution for carbons in the aliphatic region. The reverse was obtained using SL [4] sequence, i.e. good resolution for aliphatic carbons and severe broadening for those aromatic carbons with the largest couplings to the ^{19}F. Since this broadening of the group of carbons close to the ^{19}F site is very peculiar, we decide to investigate the nature of this effect. This chapter will be dedicated to examining the impact of ^{1}H-decoupling in liquid crystals and in particular focusing our attention on the C—H—F spin system.

Many heteronuclear decoupling sequences have been developed in order to reduce the carbon linewidth and to improve their decoupling efficiency (i.e. minimising the amount of RF-power deposited into the sample). The latter aspect is very important in liquid crystal samples, since the removal of RF heating effects is crucial point in order to obtain high resolved spectra.

In order to understand more about heteronuclear decoupling in LC's and in particular its effects on C—H—F systems, we tested different decoupling schemes based on composite pulses and phase modulations, such as TPPM [5, 6], COMARO [7] and SPINAL [6] families. We found that the novel SPINAL sequences were able to restore good resolution over the entire ^{13}C bandwidth with a minimum of optimisation. Successful interplay between the experiments and numerical simulations was fundamental in order to establish the physical origin of these broadenings

4.2 Initial experiments: determining the origin of the line-broadening

As demonstrated in the previous work [2] on this sample (I35), each ^{13}C site should be split into a doublet by its coupling to the ^{19}F. Fast relative motion of the molecules in the LC phase eliminates intermolecular interactions and so only intra-molecular interactions will be significant; the heteronuclear couplings to ^{1}H should be eliminated by decoupling.

Preliminary experiments had shown, however, that it was very difficult to obtain a well-resolved spectrum across the entire spectral width. In particular, many of the expected C—F doublets were poorly resolved in the CW-decoupled spectrum. Since the resolution of these couplings was critical to their quantification, we decided to investigate the origin of the behaviour.

We proposed a number of possible explanations:

1. RF heating: it is well known that the resolution of ^{13}C spectra of liquid crystals can be significantly degraded by RF heating if the mean power deposited in the sample becomes too high [8]. Although motionally averaged, the C–H dipolar interactions are large (kHz) and so require relatively high B_1 fields for decoupling (compared to the decoupling of the J interactions of solution-state NMR). This means relatively high powers (typically 60 W in our experiments) are being deposited in the sample during decoupling. The resulting RF heating causes local fluctuations of the order parameter of the nematic phase [9]. Since the correlation time of these fluctuations is comparable with T_2, the resolution is degraded. Any overall increase in the sample temperature will also change the order parameter and hence the resonance frequencies of peaks with a non-zero shift anisotropy.
2. An unidentified "coherent" effect i.e. an explanation in terms of the NMR Hamiltonian.
3. An unidentified "incoherent" effect, i.e. an explanation in terms of relaxation effects. Line widths may be limited by the appropriate T_2 value; so one possible explanation is that the relaxation is particularly efficient for the carbons close to ^{19}F [10]. Moreover, it is well known from solution state NMR that correlations between different relaxation mechanisms can result in differential line-broadenings of multiplet components. This effect is now widely exploited in the TROSY experiment [11], which selectively detects the narrow component of a differentially broadened multiplet.

The experiments were performed on a Chemagnetics CMX spectrometer operating at a proton Lamor frequency of 200.13 MHz, using a standard double-resonance MAS

probe. (A static probe with an horizontal coil would give more efficient RF performance than MAS probes in which the coil is inclined at the magic angle with respect to the magnetic field, but it was useful to perform all experiments, static and spinning, with the same experimental set-up). Solid I35 was packed into the 7.5 mm (external diameter) rotors and the sample was then maintained in the nematic phase at 40 °C (Chemagnetics temperature controller). The proton linewidth measured on a static sample of PDMSO was ~20 Hz corresponding to a linewidth of ~ 5 Hz on ^{13}C. Although this inhomogeneous linewidth is large by solution state standards, it is not unreasonable for liquid crystal experiments and is reasonably good for a static sample in a probe not designed for high-resolution work.

^{13}C spectra were obtained using a variety of phase-modulated proton decoupling sequences.

4. As we have already mentioned CW stands for continuous wave irradiation and consists of a constant amplitude B_1 field.

5. COMARO [7] (*composite magic angle rotation*) derives from two pulse elements XY (where Y and X are the phases 0 and $\pi/2$ of the RF-field).

   Inserting the composite pulses $\phi_1 = 385, \phi_2 = 320$, $\phi_3 = 25$ in Y and X we obtain the COMARO multi-pulse sequence:

   $$COMARO = Y_{385}\,\overline{Y}_{320}\,Y_{25}\,X_{385}\,\overline{X}_{320}\,X_{25}$$

   Where the subscripts represent the nutation angles of the z-component of the ^1H-magnetization, while the bars at the top of X and Y represent the phases π and $3\pi/2$ of the RF-field respectively.

   We implemented the COMARO-2 scheme, which is obtained with the same substitutions in X, Y $\overline{Y}$ of the COMARO sequence:

   $$COMARO-2 = (XY)_3\,(\overline{Y}X)_3$$

6. COMPOSITE PULSES decoupling [12] sequence: the sequence here described is an element of COMPOSITE PULSES decoupling family, which is designed for the off-resonance compensation. As in COMARO sequences, the sequence used

derives from two pulse elements XY (where Y and X are the phases 0 and $\pi/2$ of the RF-field). Inserting the composite pulses $\phi_1 = 336, \phi_2 = 246$, $\phi_3 = 10$ $\phi_4 = 74$ in Y and X we obtain:

$$X_{336}\bar{X}_{246}Y_{90}\bar{Y}_{74}Y_{10}\bar{X}_{246}X_{336}$$

7. TPPM, SPARC and SPINAL families: the TPPM scheme (*two pulse phase modulation*) contains two alternating pulses, $P = \tau_P(\phi/2)$ and $P = \tau_P(-\phi/2)$, where τ_P is a short pulse of about, 165° and ϕ is a small phase angle (about 8°).

$$TPPM = \bar{P}P$$

SPARC [5] is built from arranging the basic *TPPM* pulses P and $\bar{P}$ in phase cycling schemes according to a method developed in references [13, 14]. In particular we have implemented the SPARC-16 super-cycle:

$$SPARC-16 = P\bar{P}\bar{P}P\ \bar{P}PP\bar{P}\ PP\bar{P}P\ \bar{P}\bar{P}P\bar{P}$$

As mentioned in Chapter-1 SPINAL is obtained by particular combination of the elements Q and $\bar{Q}$. These elements are obtained changing the phase angle in the basic elements P and $\bar{P}$ of *TPPM* scheme. They are represented as:

$$Q = \tau_P(10)\tau_P(-10)\tau_P(15)\tau_P(-15)\tau_P(20)\tau_P(-20)\tau_P(15)\tau_P(-15)$$

$$\bar{Q} = \tau_P(-10)\tau_P(10)\tau_P(-15)\tau_P(15)\tau_P(-20)\tau_P(20)\tau_P(-15)\tau_P(15)$$

In particular we have investigated two members of *SPINAL* family, SPINAL-64 and SPINAL-128:

$$SPINAL-64 = Q\bar{Q}\bar{Q}Q\ \bar{Q}QQ\bar{Q}$$

$$SPINAL-128 = Q\bar{Q}\bar{Q}Q\ \bar{Q}QQ\bar{Q}\ QQ\bar{Q}Q\ \bar{Q}\bar{Q}QQ$$

The decoupling performance is highly dependent on the ^{1}H transmitter frequency and so this was optimised for each sequence. The different sequences do not have the same offset dependence. The various parameters of the different pulse sequences were also optimised: pulse duration τ_P for TPPM, SPARC and SPINAL, while for TPPM the

phase difference ϕ was also optimised. The optimal spectra for the various decoupling sequences are shown in Figure 4.1.

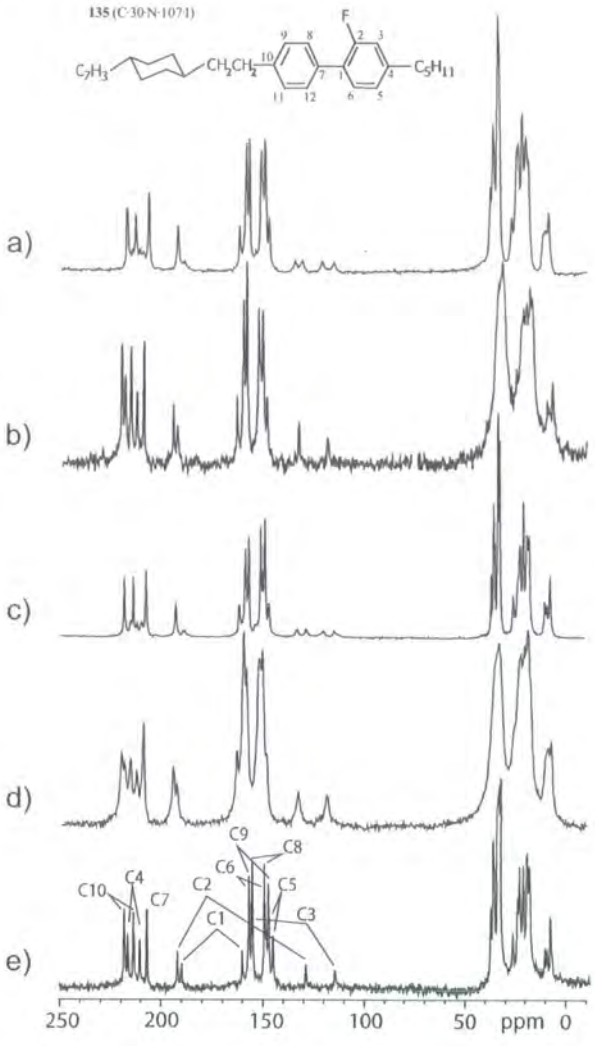

Figure 4.1 ^{13}C-spectra of I35 in the nematic phase with various ^{1}H-decoupling schemes: (a) CW, (b-c) COMARO-2 and TPPM respectively, while (d) COMPOSITE PULSES and SPINAL-64, (e). For both TPPM and SPINAL-64 the pulse duration τ_P was optimized resulting in tip angles of ~ 180° and ~170° respectively. For TPPM the phase difference was also optimized (to 14°). We also performed experiments with SPARC, which are not shown here, since the results are very similar to TPPM. Moreover results from SPINAL-128 have been omitted as well since the performance of SPINAL-64 was slightly better. The assignment of the C—F doublets illustrated on spectrum (a) was taken from reference [2]. The experiential parameters were: contact time 3ms, recycle delay 5s and decoupling

power 50 kHz. The variation of the signal-to-noise (S/N) in the spectra is due to different numbers of the transients accumulated.

To check the impact of RF heating on the spectral quality, we also tested the effect of decreasing the relaxation delay between acquisitions while using SPINAL64 decoupling. Decreasing the recycle delay increases the mean power deposited in the sample and leads to shifts of the resonance frequencies. As shown in Figure 4.2, the shifts are negligible under the conditions used in the experiments of Figure 4.1 i.e. a recycle delay of 5 s.

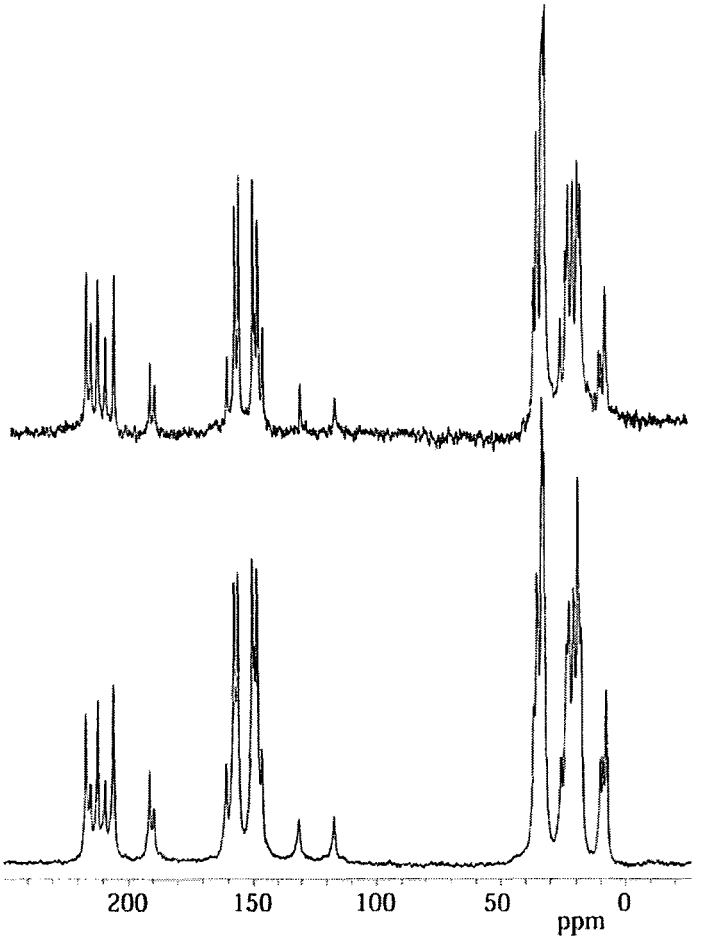

Figure 4.2 ^{13}C spectrum of I35 in the nematic phase at 40° with SPINAL-64. This experiment was performed with the same setting as that described in the caption of Figure 4.1 except for the recycle delay, which was reduced from 5 s (top) to 2 s (bottom).

The best quality spectra were consistently obtained using the SPINAL-64 sequence; the minimum ^{13}C linewidth was about 10 Hz. COMARO-2 gives the same line resolution for aromatic carbons, while aliphatic carbons are poorly resolved; COMPOSITE PULSES decoupling even resolving the larger C—F splittings, such as C1, C2 and C3, the overall ^{13}C-spectrum is broadened. On the other hand the C—F doublets are poorly resolved in the both the CW and TPPM-decoupled spectra e.g. C4 is broadened, while in other doublets, such as C2 and C3, one component is sharp while the other splits into a broad doublet. These additional spectra features are hard to explain by either RF heating or "incoherent" effects, which could give line-broadenings or even shifts, but are not expected to lead to additional splittings.

As seen above, the effects of RF heating are expected to be minimal under the conditions used. It would also be extremely difficult to explain the asymmetric broadening of some of the multiplets in this way. This leaves an explanation in terms of the nuclear spin Hamiltonian as the most likely possibility. The presence of additional "peaks" in the spectrum also applies additional "transitions" of some form. Since the appearance of these effects is strongly dependent on the decoupling sequence used, it is unsurprising that they are also strongly dependent on the parameters of an individual sequence. This is confirmed in Figure 4.3, which shows the strong variation of the ^{13}C spectra using SPINAL-64 decoupling as a function of the duration τ_p of the individual pulses of the sequence.

The advantage of this experiment is that it provides a clear target for any prediction of the observed effects. It is more difficult to compare the result from different sequences, since the spectra will be affected by the set-up of the individual parameter of the sequences. The strong variation of the spectral appearance with a single parameter is something that we can hope to reproduce clearly in simulations.

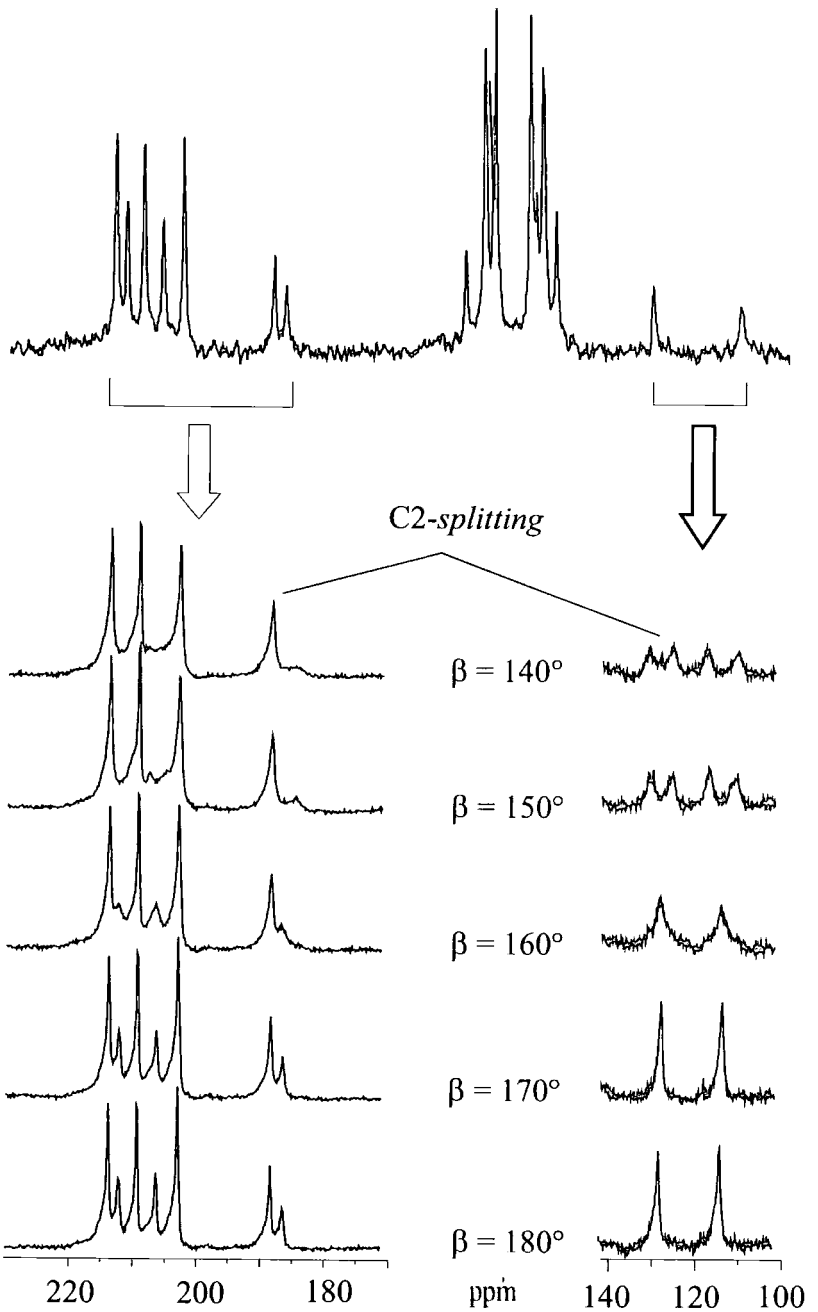

Figure 4.3 Aromatic region expansion of ^{13}C-spectra of I35 in the nematic phase at 40°. SPINAL-64 ^{1}H-decoupling was applied varying the pulse duration τ_P, given in the figure in terms of the nutation angle of ^{1}H-magnetization, β (where $\beta = \omega_{RF}\tau_p$, with ω_{RF} the strength of RF field). The experimental parameters were: contact time 3 ms, recycle delay 5 s and decoupling power 50 kHz.

4.3 Modelling of the line broadening

As seen in Figure 4.1 the C2 splittings show very clearly how the individual component of C2—F doublet is affected by the line broadening, which is not the case for the C1-C3 carbons. As a result we can hope to reproduce the observed effects in simulations the observed effects by using a suitable spin-model for the C2 carbon. For these purposes we consider the biphenyl ring of I35 as shown in Figure 4.4 and using the results obtained by Ciampi *at al* we determine which nuclear spins have significant interactions with carbon C2.

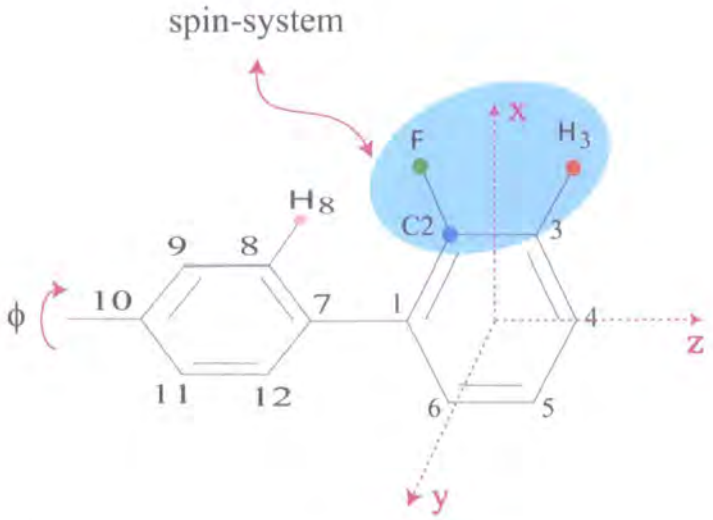

Figure 4.4 Schematic representation of biphenyl ring of I35. The two phenyl rings lie in different planes, with relative orientation of $\phi = 37^{\circ}$ around the *x*-axis. In the blue region is sketched the spin system for the carbon C2, which consists of three spins, C2—F—H3. The choice of this spin system is justified on the basis of the relative strength of dipolar interactions between the carbon C2 and the other nuclear spins in the biphenyl ring.

The dipolar interactions $D_{i,j}$'s within the rigid fluorinated fragment are given by the following formula:

$$D_{ij} = -\left(K_{ij}/r_{ij}^3\right)\left[S_{zz}\left(3\cos^2\theta_{ij;z}-1\right)+ \right.$$
$$+\left(S_{xx}-S_{yy}\right)\left(\cos^2\theta_{ij;x}-\cos^2\theta_{ij;y}\right)+ \qquad (4.1)$$
$$\left.+4S_{xz}\cos\theta_{ij;x}\cos\theta_{ij;y}\right]$$

with

$$K_{ij} = \left(\mu_0/16\pi^2\right)h\gamma_i\gamma_j \qquad (4.2)$$

and where $\theta_{ij;x}$, etc. are the angles between *xyz* axes and the inter-nuclear vector $\vec{r}_{ij}$. The axes *xyz* constitute a reference frame fixed in the fluorinated ring, as drawn in Figure 4.4. The quantities S_{zz} etc, in Eq. (4.1), are the local order parameters for these axes. From the knowledge of the bond lengths and the relative angle of the biphenyl rings, the coordinates of the atomic positions have been, and from these the internuclear vectors r_{ij} and angles $\theta_{ij;x}$, etc have been calculated. Using these data and the order parameters previously determined by Ciampi [2] a set of dipolar couplings $D_{C2,j}$ and $D_{F,k}$ has been calculated, where the index k is referring to us the ^{1}H's, while for the index j, the ^{19}F nucleus is also included. The resulting set of these dipolar couplings is outlined in Table 1:

Table 1 Dipolar couplings for the carbon 2 spin-system (/kHz). The dipolar couplings do not contain the absolute errors, as they are very small and so not relevant to the simulations.

Atoms	F	H3	H8	Other H's
C2	~ 1.5	~ -1.5	~ 0.5	< 0.6
F	0	~ -5.2	~ -1.4	< 0.5
Order Parameters used to calculate the dipolar couplings				
$S_{zz} = 0.682 \pm 0.001$		$S_{xx} - S_{yy} = 0.011 \pm 0.001$		$S_{xz} = -0.013 \pm 0.001$

As seen from Table 1 we only need consider the interactions of C2 with the ^{19}F and H3. Although the proton H8 experiences a significant dipolar interaction with the ^{19}F (~ 1.4 kHz) its interaction with C2 is weak, so we neglect effects on the C2 spectrum. The rest of the spins are interacting with the spin system C2—F—H3 only weakly (interactions < 0.5 kHz), and so negligible line-broadening effects on C2 resonances from them are expected. We simulated the C2 signal varying the tip angle β and leaving the ^{1}H-offset as a free parameter of the simulations since the proton spectrum is too poorly resolved to permit an accurate measurement of the offset of H3 relative to the ^{1}H-trasmitter. In the simulations we have neglected any effect from relaxation processes, and the results are illustrated in Figure 4.5.

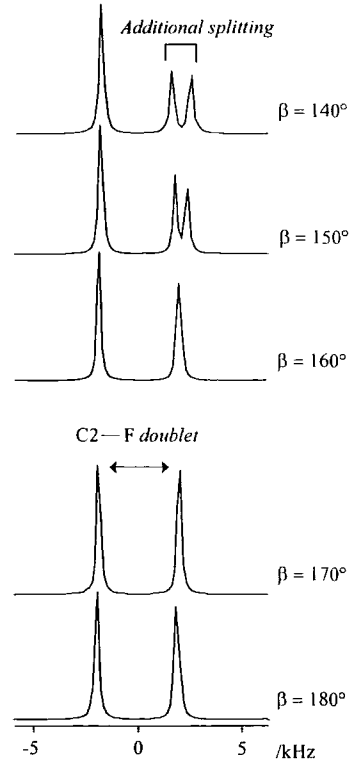

Figure 4.5 Simulation of C2 spectra for the spin system C2—H3—F using SPINAL-64 for ^{1}Hdecoupling with various values of the tip angle β. According to Table 1 the internal interactions were: d_{CH}, 1.5 kHz, d_{HF}, 5.2 kHz and d_{CF},, 1.5 kHz. The ^{1}H-offset, δ_H, was arbitrarily set to 1 kHz, while the decoupling power was 50 kHz as in the experiment. The MATLAB code used can be found in the Appendix.

To calculate the carbon signal we have calculated the time evolution of the initial density matrix $\rho(0) = I_x$, under the influence of the total time-dependent Hamiltonian, H_T.

This total Hamiltonian is given by a sum of an internal time-independent spin Hamiltonian, H_{int}, which describes the interaction between spins, and a time-dependent RF-Hamiltonian, H_{rf}, resulting from the interaction of the applied RF-field B_1 with ^{1}H-spins of the system.

$$H_T(t) = H_{\text{int}} + H_{rf}(t) \tag{4.3}$$

The internal Hamiltonian, in this case, is written as:

$$H_{\text{int}} = \delta_C I_z^C + \delta_H I_z^H + \delta_F I_z^F + 2d_{CH} I_z^C I_z^H + 2d_{CF} I_z^C I_z^F + 2d_{HF} I_z^H I_z^F \tag{4.4}$$

Since the operator and I_z^F commutes with both H_T, and the initial carbon density matrix, the ^{19}F chemical shift, δ_F, have no effect on the time evolution of the carbon signal, while the chemical shift δ_C just shifts the ^{13}C resonances so it can be ignored.

As seen in Figure 4.5 numerical simulations based on a simple three-spin system C—H—F convincingly reproduce the experimental trends. In Figure 4.6 we plot the functional dependence of the second moment on the ^{1}H-offset and the tip angle β.

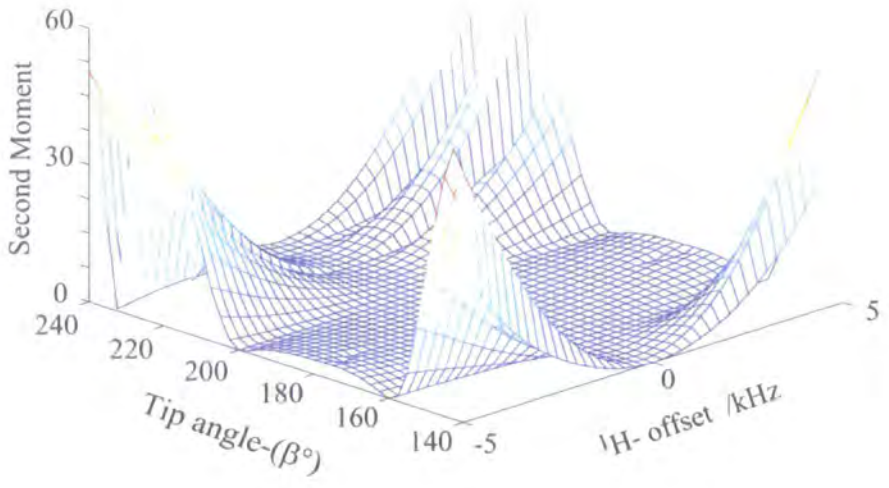

Figure 4.6 Second moment simulation of the ^{13}C spectra as a function of the ^{1}H-offset and SPINAL-64 tip angle β . The RF power and dipolar coupling d_{CH}, 1.5 kHz, were the same that we used for the C2—H3—F system.

As seen in Figure 4.6 the performance of SPINAL-64 is consistent with experiment of Figure 4.3. The flat region of Figure 4.6 in consistent with the lack of significant difference between the spectra with tip angles 170° and 180°. However this is only true for the aromatic carbons. The best tip angle for *both* aliphatic and aromatic carbons of I35 is about 170°. This suggests that the C—H spin system is a suitable choice for the aromatic carbons rather than for the aliphatic carbons where stronger ^{1}H—^{1}H homonuclear interactions are expected. Figure 4.6 also shows that the ranges of the tip angle β where the line broadenings take place correspond to those regions where the SPINAL-64 becomes very sensitive with respect to the ^{1}H-offset. Experimentally we investigated these theoretical results experimentally using SPINAL-64 with a misadjusted tip angle β, (~140°), and varying the ^{1}H-offset. Despite the poor resolution of these badly decoupled spectra rather clear results were obtained. In Figure 4.7 the C2 resonances clerly resolve into doublet as the ^{1}H-transmitter frequency is significantly shifted away from the reference frequency ν_{ref}

(200.13 MHz). This large shift is peculiar for the carbons with the largest C—F splittings, showing a significant different dependence from the ^{1}H-offset in comparison with rest of the other aromatic and aliphatic carbons. The simulations of C2 resonances based on C2—H3—F spin model convincingly reproduce the experimental behaviour, as illustrated on the right side of Figure 4.7. Although the simulations and the experiments are clerly showing that the broadening of a component of C2 doublet could be consistent with an off-resonance effect, the other component turns out to be sensibly independent from the ^{1}H-shift. Further investigations on this asymmetric behaviour have been done by using CW decoupling. CW experiment was performed keeping the ^{1}H transmitter frequency fixed while the decoupling power was varied within a wide range. With this experiment we can explore indirectly how the individual components of C2 doublet are affected by an off-resonance irradiation. We should note that the equivalent experiment with the misadjusted SPINAL-64 could lead to the same results. However SPINAL-64 has a complicated time dependence for which the relationship between the off-resonance and decoupling power less clear than that in CW decoupling. On the other hand unlike SPINAL-64, the CW Hamiltonian is static in a suitable rotating frame and an exact analysis of a simple spin system is possible [15].

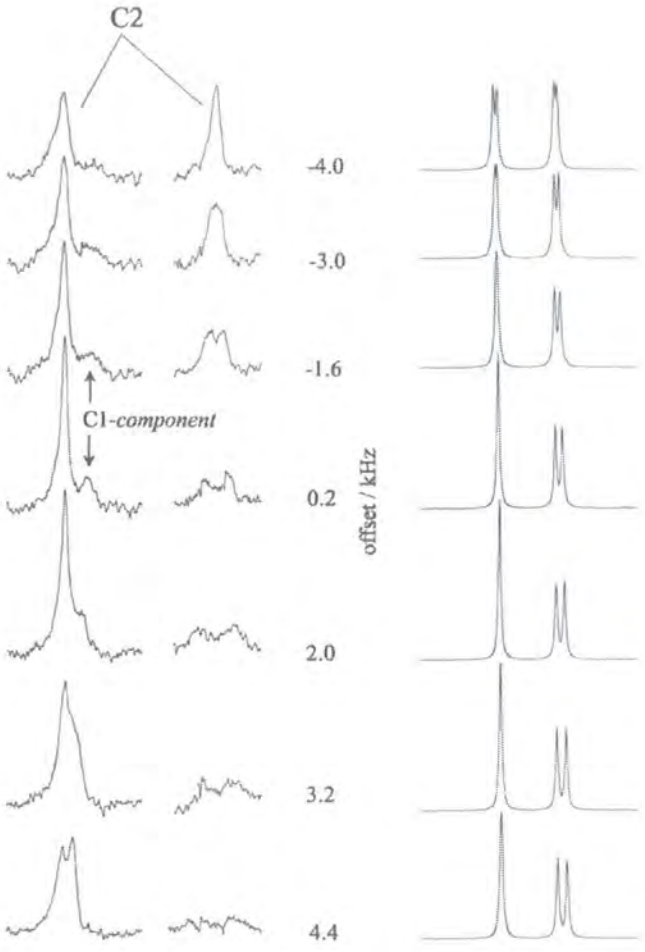

Figure 4.7 (Left) selected C2—F splittings from the ^{13}C spectra of I35 in the nematic phase (T~40°), using ^{1}H-SPINAL-64 decoupling with a misadjusted tip angle ($\beta \sim 140°$), as a function of ^{1}H-offset with decoupling power of 50 kHz. (Right) simulations, based on C2—H3—F spin system,. The only free parameters of the simulation was a uniform ^{1}H-offset, which was found to be ~ 500 Hz. The rest of the parameters were set according to Table 1.

From theoretical analysis and experiments it is well known that the efficiency of CW decoupling also strongly depends upon the relative strength of decoupling field and ^{1}H-offset [15]. Setting the carrier frequency of ^{1}H-transmitter in the centre of the ^{1}H-spectral band we performed varied the decoupling power within a wide range of values (80-30 kHz). The results of this experiment are shown in Figure 4.8. It will be noticed that even at relatively high decoupling power, e.g. ~80 kHz, additional line

splittings of C2-C3 carbons are still present, and as these become very large at relative low powers, (e.g. ~30 kHz).

This behaviour is strongly reminiscent of the off-resonance effects familiar from both liquid-state [16] and, to a lesser extent, solid-state [17] NMR.

Although the trend of the additional splittings such as those observed for a component of C2 doublet could be consistent with what we expect from increasing off-resonance effects, it remains hard to interpret the behaviour of the other component, which shows a single peak, which is well resolved at high decoupling powers.

Simulations of C2 carbon using the previous C2—H3—F spin model reproduce perfectly the experimental dependence on ν_{rf}, as illustrated on the right side of Figure 4.8. The only variable was the ^{1}H offset, which was found to be $\delta_H \approx 4$ kHz.

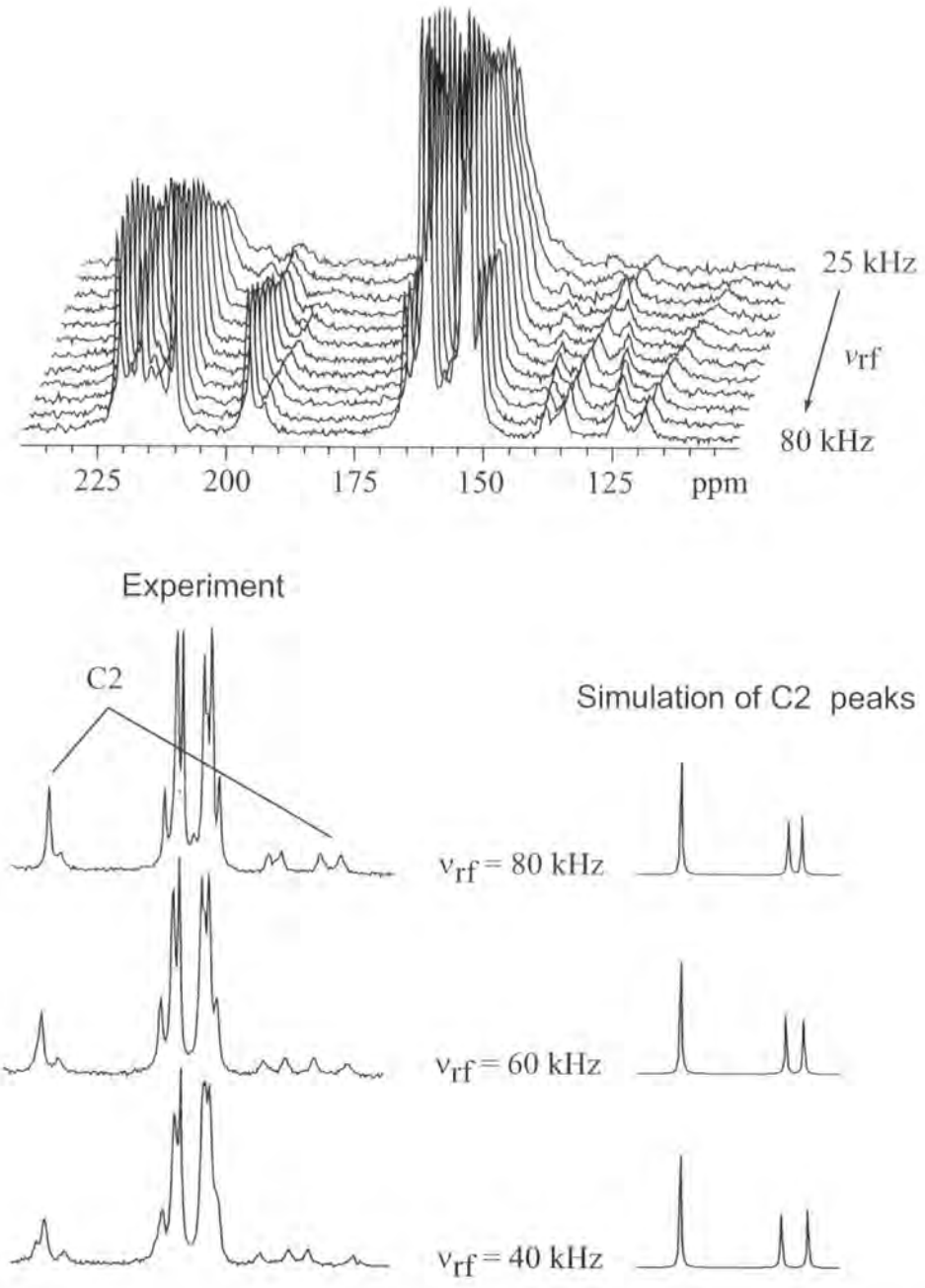

Figure 4.8 (Top) ^{13}C spectra as a function of power of CW irradiation, expressed as the nutation frequency ν_{RF}. (Bottom) Comparison of selected slices of this data set with numerical simulations of the spectra for C2 using the experimental parameters plus the known dipolar couplings: d_{CH}, 1.5 kHz, d_{CF}, 1.7 kHz, d_{HF}, -5.2 kHz.

Consideration of the Hamiltonian structure for the C—H—F system reveals the origin of these effects. Starting from the internal Hamiltonian (4.3) and considering that only the ^{1}H is irradiated, the spin coordinates relevant to the ^{13}C and ^{19}F are both secular with the Zeeman interactions. As a result the total Hamiltonian (4.3) can be blocked into sub-spaces labelled according to the ^{13}C and ^{19}F α and β states.

Thus the Hamiltonian in the ^{1}H-subspace, for ^{19}F in an α state and, for instance, the ^{13}C in a β state is given by:

$$H_{\alpha/\beta} = \left(\frac{-\delta_C}{2} \mp \frac{d_{CF}}{2} \right) \mathrm{I} + \left(\delta_H + d_{HF} - d_{CH} \right) I_Z^H + \nu_{rf} I_X^H \tag{4.5}$$

Where I is the identity operator in the ^{1}H-Hilbert' space.

Indeed, the Hamiltonian (4.5) has the same mathematical form as for the simple C—H case. Considering the C—H Hamiltonian for the ^{13}C in the α and β states we have:

$$H_{\alpha\beta} = \left(\pm \delta_C / 2 \right) \mathrm{I} + \left(\delta_H \pm d_{CH} \right) I_Z^H + \nu_{rf} I_X^H \tag{4.6}$$

The only differences between the Hamiltonians of Eq. (4.5)-(4.6) are due to the presence of an effective shift of the ^{13}C resonances i.e., $\delta_C \mp d_{CF}$, and by an additional offset term given by the H—F dipolar interaction, d_{HF}. As a result three-spin C—H—F system can be considered as formed by two independent C—H spin system, according to the ^{19}F states.

As seen in Chapter 1, a mismatch of decoupling transmitter from the exact resonance condition results in a non-zero scaling factor χ of the C—H interactions, causing line-broadening, or even splitting if single C—H interactions are resolved. This is shown in the simulations of Figure 4.9 (b-c).

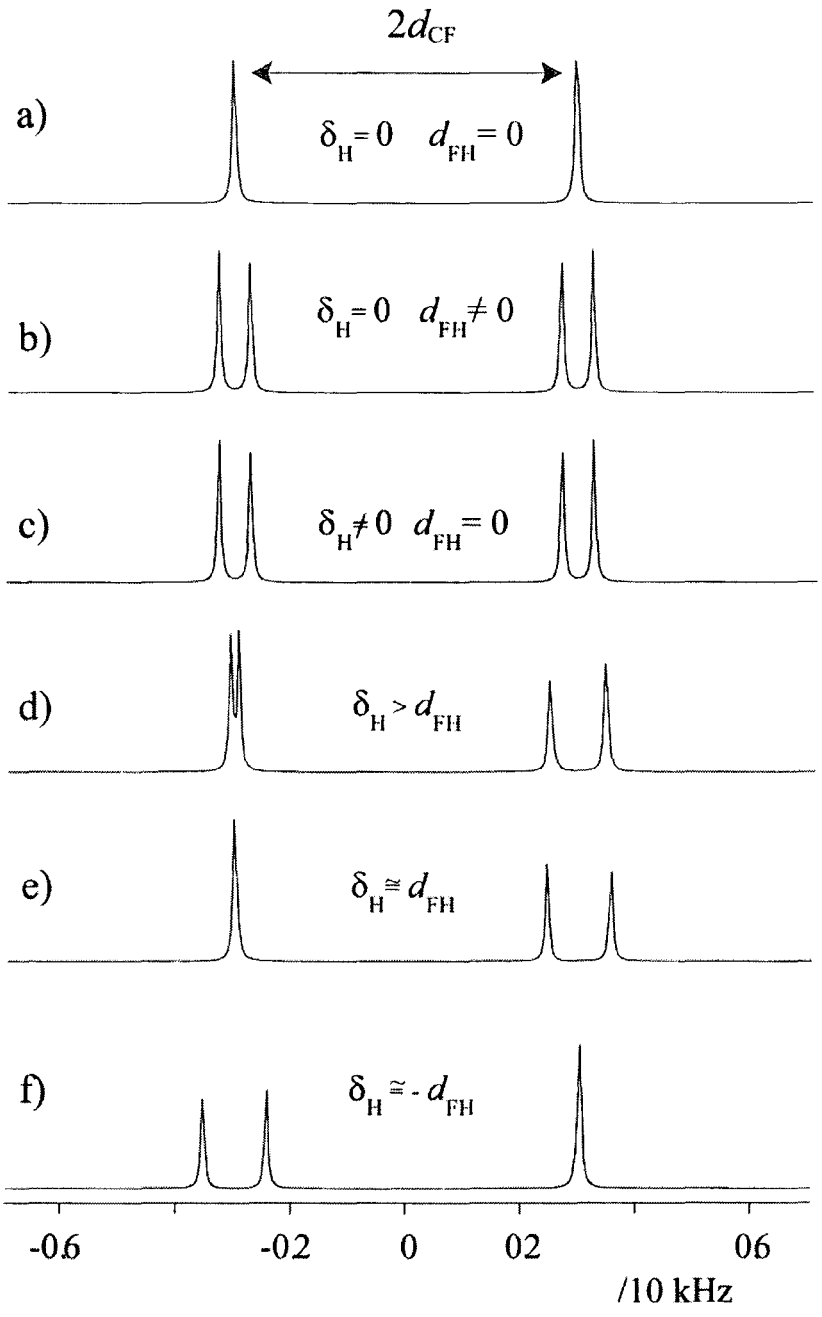

Figure 4.9 Effects of various combinations of ^{1}H off-resonance shift (H) and H—F dipolar coupling (d_{HF}) on a simulated C—F doublet under ^{1}H-CW decoupling: (a) no H—F coupling, on-resonance, (b-c) off-resonance or non-zero dipolar coupling, (d-f) different combinations of off-resonance shift and dipolar coupling.

The introduction of H—F interaction into an effective offset, Eq. (4.5) may seem trivial; indeed its effects are equivalent to a non-zero offset, as clearly shown by the simulation in the Figure 4.9 (b-c). Unlike δ_H, however, the effective off-resonance term, now, depends on the ^{19}F state, and we cannot remove its effects by optimising the transmitter offset. Moreover, d_{HF} can be large, much larger than the variation of δ_H due to ^{1}H chemical shift range (~500Hz at a ^{1}H Larmor frequency of 200 MHz). In particular for C2, the relevant dipolar coupling d_{HF} is about -5.2 kHz. This is clearly seen in the ^{19}F-spectrum of I35 in the nematic phase.

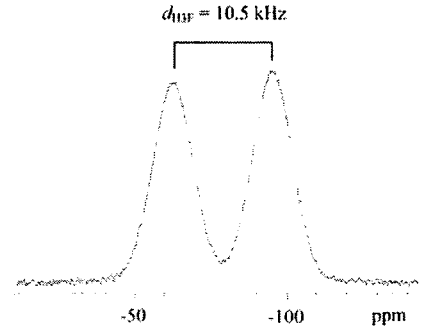

Figure 4.10 ^{19}F-spectrum of I35 in the nematic phase at T ~40°. The doublet is due to the largest F—H3 dipolar coupling. The rest of ^{1}H's of biphenyl ring broaden both components of F—H3 doublet, resulting in a FWHH of about 3.7 kHz.

The asymmetric effects are straightforwardly explained. It follows directly just observing that the magnitude of the effective ^{1}H offset $|\delta_H \pm d_{HF}|$ is different for a non-zero ^{1}H chemical δ_H according to the ^{19} F state. Hence the different appearance of the individual components of the C—F doublet are the result of different performance of the ^{1}Hdecoupling, as seen Figure 4.9-(d). In particular when $\delta_H \approx d_{HF}$, one component is on resonance giving rise to a very sharp peak, while the other component is being irradiated off resonance and splits into a resolved doublet. The simulations successfully reproduce the behaviour of the C2 and C3 splittings. This means that the C—H—F spin model for C2 and C3 is sufficient to describe the "real" spin system in the limit where the rest of the other interactions can be neglected.

As for C4 resonances the simple C—H—F spin model is inadequate to reproduce the experimental observations, because many other non-negligible dipolar interactions are involved. So the spin model for C4 will include all the nuclear spins present in the mono-fluorinated ring and the corresponding Hamiltonian, and is given by:

$$H_{\text{int}} = \delta_C S_z + 2d_{CF} S_z I_z^F + \sum_{k=1}^{3} \delta_{H,k} I_{k,z}^H + 2d_k^{CH} S_z I_{k,z}^H + 2d_k^{FH} I_z^F I_{k,z}^H + \sum_{k<j}^{3} d_{k,j}^{HH} \left(2I_{k,z}^H I_{j,z}^H - I_{k,x}^H I_{j,x}^H - I_{k,y}^H I_{j,y}^H \right) \tag{4.7}$$

The set of dipolar interactions, have been determined from previous results [2] as described earlier in this section, and are summarized in

Table 2.

Table 2 Dipolar couplings for the carbon 4 spin-system (/kHz). The dipolar couplings do not contain the absolute errors, as they are very small and so not relevant to the simulations.

Atoms	H3	H5	H6	F
C4	~0.8	~0.9	~-0.21	~-0.15
H3	0	~0.52	0.09	~-5.2
H5	~0.52	0	~-5.5	~0.07
H6	~0.09	~-5.5	0	~0.42
Order Parameters used to calculate the dipolar couplings				
$S_{zz} = 0.682 \pm 0.001$	$S_{xx} - S_{yy} = 0.011 \pm 0.001$		$S_{xz} = -0.013 \pm 0.001$	

The ^{1}H-offset δ_{H_K} is a free parameter. The decoupling method used in the simulations, is SPINAL-64, varying tip angle beta, rather than CW, which gives a very broad C4 doublet, irrespective of any variation of experimental parameters, such as ^{1}H shift δ_H, or decoupling power ν_{rf}. Hence, using the SPINAL decoupling and varying the adjustable parameters, such as the tip angle, allows us to connect the experimental observations with the calculated spectra. The correspondence between the experiments, Figure 4.1, and the results of the simulations, Figure 4.11, is remarkable and provides unequivocal demonstration of the spin dynamical nature of these effects.

A comparison between the simulations of Figure 4.11, with homonuclear interactions, (a), and without, (b), respectively, shows no substantial difference.

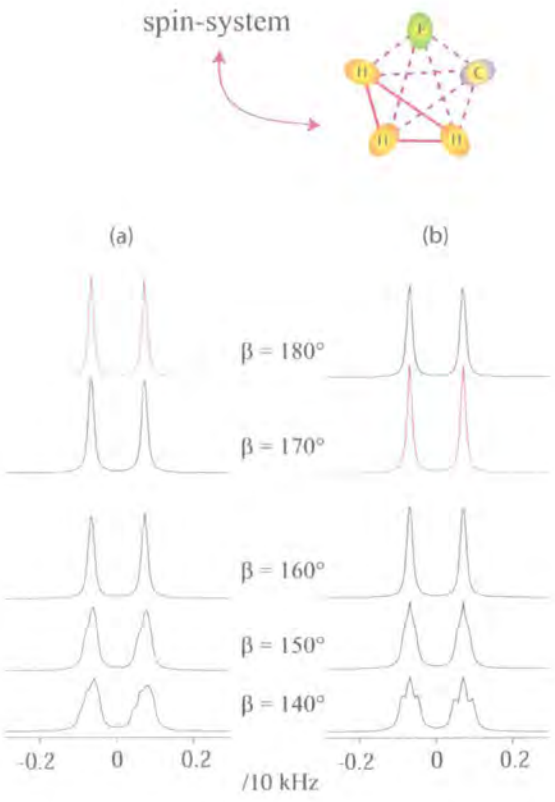

Figure 4.11 Simulations with SPINAL-64 of an entire phenyl fragment i.e., C—F—H_3 for the carbon C4. Varying the tip angle β, within the range (140°-180°), and using the real set of dipolar coupling constants, we reproduce the experimental observation. (b), simulations neglecting the H—H interactions. Including H—H interactions do not introduce substantial differences, however it will be noticed that the best tip angle β is now $180°$, and $170°$ when the H—H are not included (spectra in red).

Nevertheless, a closer examination of the simulations, (b), shows that, as observed in the spectra, the C—F doublet slight better resolved for a tip angle of ~ 180°. Unlike C2, where the best decoupling has been obtained with a tip angle of ~170°, including H—H interactions, the best performance of SPINAL-64 is now achieved with a tip angle of 180°. This difference in tip angle may seem irrelevant, however, it shows that the decoupling mechanisms is affected by the ^{1}H flip-flop term of the homonuclear Hamiltonian. This suggests that a fuller understanding of decoupling is likely to

require a more complete treatment of the dipolar-coupling network between protons. If we neglect the ^{1}H homonuclear interactions, the spectrum from, say, a $CFH_AH_BH_C$ system is simply given by the convolution of the spectra the individual CHF systems i.e., $CFH_A \otimes CFH_B \otimes CFH_C$. If one of these protons is particularly influenced by the ^{19}F (e.g., C1, C2, C3) visible line-splittings will be observed, otherwise the convolution of a number of small splittings will result in a non-specific and increasingly Gaussian line-broadening (e.g., C4).

4.4 Exploiting of line splitting effects

As often occurs in NMR, the detailed investigation of particular effects can be helpful, not only for a deeper understanding of the technique itself, but also for obtaining more information from the experiment. For instance, in our case, the observation of the line splitting can give information about the relative signs of C—F dipolar couplings, may otherwise difficult to obtain. As an example, the H—F interaction, in the biphenyl fragment of I35, is the same for C2 and C3 carbons, the observed line-splittings must be consistent with the relative signs of the dipolar couplings, d_{C2F} and d_{C3F}. Changing the decoupling RF-field offset reveals the relative sign of these dipolar couplings. From the spectra of Figure 4.12, we can, easily, deduce that the dipolar coupling of C2 and C3 have opposite sign. This is straightforward if we realize that reversing the sign of C—F dipolar coupling swaps the peaks of the doublet. As a result varying the ^{1}H-offset will affect the individual components of the C—F doublet in the opposite fashion.

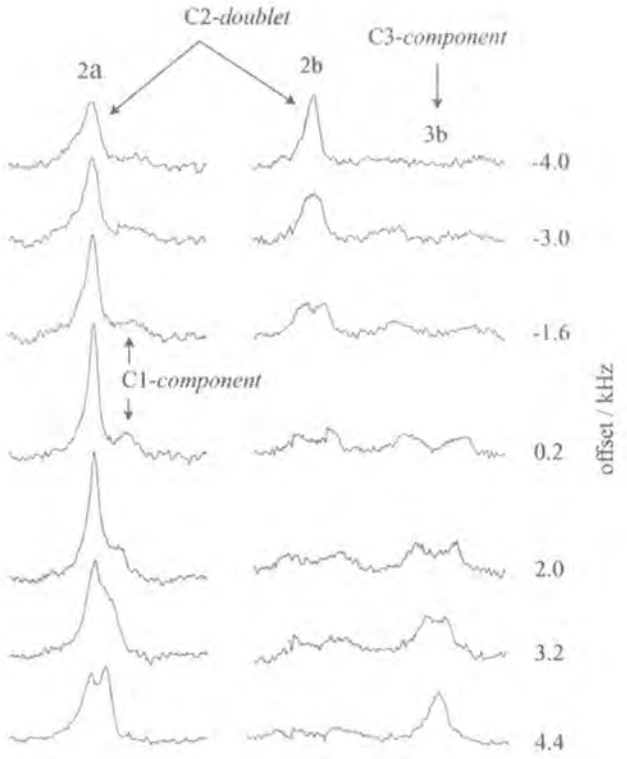

Figure 4.12 Exploiting the line-splitting effect. Selected portions of the ^{13}C-spectra of I35 in the nematic phase at ~40° C, as a function of ^{1}H-offset (SPINAL-64 decoupling). The tip angle β was misadjusted (~140°) in order to observe the line-splitting effects over the range of ^{1}H-offset used. Following the components of C2 and C3 doublets, 2b and 3b, respectively, we can easily see that they have opposite behaviour as the ^{1}H-offset varies.

We can exploit the line-splitting effects to determine the relative dipolar coupling sign, using, such as SPINAL, whose performance can be controlled by changing a set of experimental parameters. For instance the variation of the tip angle β, in SPINAL, enables the degree of line-splitting effects on ^{13}C linewidth to be controlled; we cannot obtain the same results using CW, or even TPPM decoupling, because even a slight mis-setting of the ^{1}H-transmitter frequency from the optimum condition produces a excessively large ^{13}C line-broadenings.

4.5 More about off-resonance irradiation

Indeed, these off-resonance effects have been used, in the past. Off-resonance decoupling can be exploited to simplify the assignments in heteronuclear spin systems by scaling the spin-spin interactions. By applying a strong RF-field and varying its frequency within a range large with respect to the *I*-spectrum bandwidth, we can modulate the scaling factor, χ (see Chapter 1-6) leading to *S*-spin multiplets dependent on the *I*-spin resonance offset. Experimentally, off-resonance effects are minimized by optimising the position of the ^{1}H transmitter to reduce the size of δ_H. However in many circumstances it can be very difficult to minimize the off-resonance effects for all the ^{1}H's of the molecule. This is clearly seen in Figure 4.13, which shows the optimisation of CW decoupling with respect to the ^{1}H-offset. The resulting ^{13}C spectra show that the optimal spectra for the aliphatic and aromatic carbons correspond to significantly different settings of the ^{1}H-transmitter frequency. The difference between the aliphatic and aromatic ^{1}H's is about ~1kHz, which corresponds to ~5 ppm for the ^{1}H Larmor frequency of 200 MHz. This is consistent with the relative chemical shift between the aliphatic and aromatic ^{1}H's.

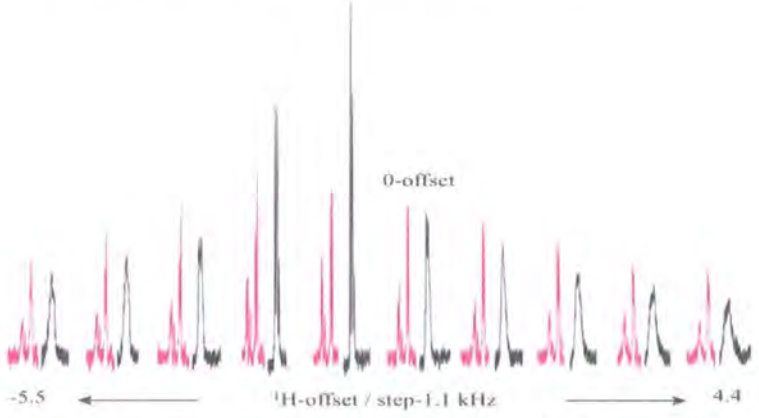

Figure 4.13 ^{13}C-spectra of I35 in the nematic phase at 40° C with CW decoupling as a function of the ^{1}H-offset. The parts in colour are the aromatic regions and the other parts the aliphatic region. The experimental parameters were: contact time, 3ms, recycle delay, 4 s, and decoupling power, 50 kHz.

As shown in Figure 4.14 SPINAL-64 turns out to be fairly sensitive with respect to the displacement of ^{1}H transmitter frequency for the aliphatic ^{1}H's and to a lesser extent for the aromatic ^{1}H's. However, unlike CW, for a particular setting of ^{1}H transmitter

frequency it provides a good ^{13}C resolution over the entire bandwidth (see Figure 4.1-e).

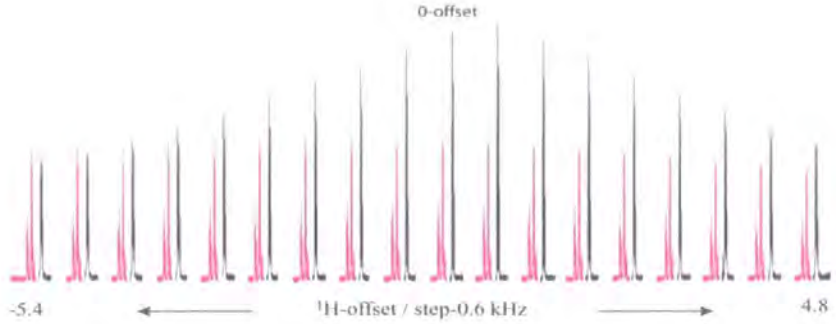

Figure 4.14 ^{13}C-spectra of I35 in the nematic phase at 40° C with SPINAL-64 decoupling as a function of the ^{1}H-offset. The tip angle was 170°, and the decoupling power, 50 kHz. In each element of the spectra series the part in colour is the aromatic region and the other part the aliphatic region. The experimental parameters were: contact time, 3ms, recycle delay, 4 s.

This is a puzzling result since it poses the question whether or not the offset is an important parameter in order to obtain good decoupling. It is interesting in Figure 4.14 to note the different offset dependence of SPINAL with respect to the aromatic and aliphatic ^{1}H's. The aromatic carbons are affected by the ^{1}H-offset only little. This agrees with the results of the simulations of Figure 4.6 giving a further confirmation that for the aromatic carbons the C—H spin model is a suitable approximation. As for the aliphatic carbons, the ^{1}H-offset dependence of SPINAL is relatively strong and this could be due to the presence of large H—H dipolar interactions. The simulations shown in Figure 4.15 confirm this hypothesis.

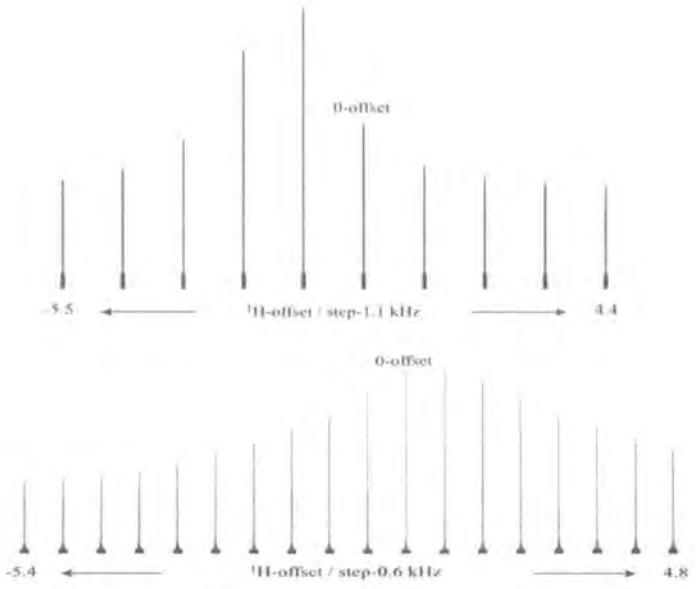

Figure 4.15 Simulations of the offset dependence of ^{13}C spectra in a C—H—H spin system for CW (top) and (bottom) SPINAL-64 decoupling. In SPINAL-64 the tip angle was 170°, and the RF- power, 50 kHz for both decoupling schemes. The ^{1}H-transmitter frequency was varied as in the corresponding experiments, with a common shift from 0-offset of 1.5 kHz for both ^{1}H's. The dipolar coupling constants d_{CH} and d_{HH}, were set to 10 and 20 kHz respectively.

In fact just simulating the ^{1}H-offset dependence of an aliphatic C—H-H group with both, CW and SPINAL-64, we are able to reproduce the profile of peak intensities that accords well with the corresponding experiments illustrated in Figure 4.13 and Figure 4.14. The results show how the different decoupling schemes are influenced by the introduction of the homonuclear interactions. In summary we can say that I35 is a very good sample to study the decoupling since it provides two well separated spin systems, C—H and C—H—H, respectively for the aromatic and aliphatic carbons. The goal of SPINAL-64 is that it is broadband decoupling for aromatic carbons; as a result the broadening for the aliphatic carbons from an off-resonance irradiation can be minimized leading to good and uniform resolution over the entire ^{13}C bandwidth.

4.6 Conclusions

Broadenings of the ^{13}C resonances in ^{1}H-decoupled spectra have been previously observed in highly fluorinated molecules, however their rationalizations clearly do not apply here, since they do not explain many experimental observations presented here. On the other hand a simple explanation in terms of off-resonance effects caused by H—F interactions appears to be more satisfactory, and correctly predicts that employing ^{1}H decoupling sequences that are robust with respect to off-resonance irradiation, such as SPINAL, can eliminate these broadenings without resorting to ^{19}F decoupling. Extending these studies to the more complicated case of solid samples under magic angle spinning we found that similar loss of resolution are at work for those C—H—F spin systems in which the H—F interactions are strong. Nevertheless the analysis and the corresponding rationalisations are not straightforward in this case. Explanation of these effects can only be rigorously demonstrated in static oriented system, such as liquid crystals. However detailed studies of these broadenings on solid samples will be given in the next chapter.

References

1. J. W. Emsley, J. C. Lindon: NMR Spectroscopy using Liquid Crystalline Solvents, *Pergamon Press* (1975).
2. E. Ciampi *et al.*, *Liquid Crystals* **26**, 109-125 (1999).
3. D. Nanz *et al.*, *J. Mag. Res.* **113**, 169-176 (1995).
4. D. Sandström, M. H. Levitt, *J. AM. Chem. Soc* **118**, 6966-6966 (1996).
5. Y. Yu, B. M. Fung, *J. Mag. Res.* **130**, 317-320 (1998).
6. B. M. Fung, A. K. Khitrin, K. Ermolaev, *J. Mag. Res.* **143**, 97-101 (2000).
7. K. V. Schenker, D. Suter, A. Pines, *J. Mag. Res.* **73**, 99-113 (1987).
8. B. M. Fung, *J.Mag. Res.* **86**, 160 (1990).
9. Min Zhou, V. Frydmann, L. Frydman, *J. AM. Chem. Soc* **120**, 2178-2179 (1998).
10. E. W. Hagaman, *J. Mag. Res.* **104**, 125-131 (1993).
11. M. H. Levitt, Spin Dynamics. Basics of Nuclear Magnetic Resonance, *John Wiley & Sons Inc* (2001), pp. 538-564.
12. M. H. Levitt, *Progress in NMR Spectroscopy* **18**, 61-122 (1986).
13. A. J. Shaka, J. Keeler, *Prog.NMR Spectrosc* **19**, 47 (1987).
14. R. F. a. F. M. H. Levitt, *J. Mag. Res.* **47**, 328 (1982).
15. R. Freeman: Spin choreography. Basic Steps in High Resolution NMR, *Oxford University Press* (1998), Chapter 1.
16. A. Abragam: Principles of Nuclear Magnetism, *Oxford University Press*, (1961), Chapter 11.
17. k. Takegoshi, C. A. McDowell, *J. Mag. Res.* **66**, 14-31 (1986).

Chapter 5

Resolving *J*-coupling in solids and liquid crystals

5.1 Introduction

As treated in detail in the previous chapter, studies of ^{13}C-NMR on mono-fluorinated liquid crystal (I35) show an unusual line broadening of the C—F doublets when applying continuous wave {^{1}H}-decoupling (CW, [1]) as well as other sequences, such as TPPM [2-4]. As previously shown (see Figure 4.1, chapter 4), the amount of the broadening was sufficiently large to make it impossible to determine the splittings of the C—F doublets from the ^{13}C spectrum. The impact of these spectral anomalies in NMR spectroscopy of liquid crystals is particularly unfortunate. The determination of physical properties of liquid crystals, such as molecular conformation, order parameters etc, requires the precise measurements of these interactions.

Combining the simulation of the spin dynamics and experiments we were able to explain the physical origin of this broadening in terms of effectively off-resonance ^{1}H-irradiation. Considering a simple C—H—F spin system and simulating the evolution of ^{13}C-signal under CW decoupling, we reproduced the experimental behaviour, showing that H—F dipolar interaction appears as an additional transmitter offset, whose sign depends on the alpha *vs.* beta ^{19}F state. If the decoupling is not robust with respect to transmitter offset (such as CW decoupling), this results in broadening of the ^{13}C resonances. By applying novel ^{1}H-decoupling sequences, in particular SPINAL [4], we recovered good resolution over the entire spectral width.

In this chapter, we extend this study of these effects to the case of spinning solid samples. This problem is much more complicated, as the Hamiltonian is now time-dependent and, at least for rigid solids, the dynamics are affected by both

intermolecular and intramolecular interactions. As a first step, we consider spinning liquid crystal samples, since rapid translational motion eliminates *intermolecular* interactions, making it easier to model the spin dynamics. We observe analogous line-broadenings in the ^{13}C spectra with CW ^{1}H-decoupling. Optimization of TPPM ^{1}H-decoupling strongly reduces, or even entirely suppresses these effects within the experimental resolution.

We then consider conventional solids. In this case, a number of factors are shown to be important in determining the ability to resolve the C—F interactions.

5.2 Spinning Liquid Crystals

5.2.1 Director dynamics

8. Stationary sample

The potential energy [5] per unit volume of a liquid crystal due to alignment of the director **n** in the magnetic field of magnitude $\vec{B}_0$ is given by

$$E = -\frac{1}{3}\Delta\chi B_0^2 \frac{\left(3\cos^2\alpha - 1\right)}{2} \tag{5.1}$$

where α is the angle between the director $\hat{n}$ and the field $\vec{B}_0$, and $\Delta\chi$ is the anisotropy of magnetic susceptibility. The minimal energy depends on the sign of susceptibility, i.e. the molecules align parallel to the field when $\Delta\chi$ is greater than zero and orthogonal to the field when $\Delta\chi$ is negative. The directors [6] of most nematic liquid crystals orient in the direction of the static magnetic field.

In the presence of a strong magnetic field, the molecules experience a torque, which is given by the derivative of the potential energy with respect to the α angle:

$$\tau_m = \frac{\partial E}{\partial \alpha} = \Delta\chi B_0^2 \cos\alpha \sin\alpha \tag{5.2}$$

The resultant alignment of the molecules is determined by the balance between the torque due to the magnetic field and the torque due to the viscosity of the fluid. The viscous torque per unit volume τ_v is given by:

$$\tau_v = \gamma_1 \dot{\alpha} \tag{5.3}$$

where $\dot{\alpha}$ is the rate of change of the direction of the director, and γ_1 is the viscosity coefficient of the fluid. At equilibrium, these torques are in balance, $\tau_m = \tau_v$.

Hence we can obtain the characteristic rate of reorientation ω_0 of the director:

$$\omega_0 = \frac{\Delta\chi B_0^2}{\gamma_1} \tag{5.4}$$

In a typical nematic liquid crystal, ω_0 is order of hundreds of Hz for B values around 10 T.

9. Spinning sample

If the liquid crystal is spun at a spin rate, ω, much greater than ω_0, the director will not have enough time to align along the magnetic field. The resulting director orientation will correspond to the minimum average of the potential energy over the period of the rotation. The Figure 5.1 shows a graphic representation of the angular variables necessary to describe the spinning of liquid crystals.

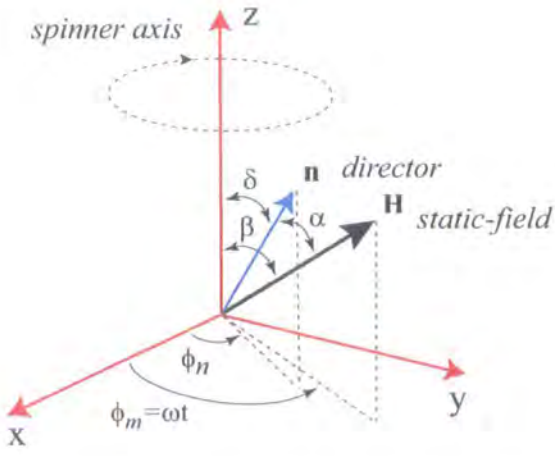

Figure 5.1 Schematic representation of liquid crystals spinning in the magnetic field. The reference frame (in red) is fixed with the sample and its z-axis is collinear with spinner axis. In this frame the magnetic field **B** is rotating around the spinner axis with an angular speed ω with respect to laboratory frame, while the director **n** is stationary. The magnetic field orientation is determined by

the polar angle β and by the time-dependent azimuthal angle ϕ_m. The angles δ and ϕ_n establish the direction of the director **n**. The relative orientation between the magnetic field and director is determined by the time-dependent angle α.

Considering the liquid crystal in the reference frame defined above under condition in which $\omega_R >> \omega_0$, the director **n** is stationary. Its orientation can be described by a polar angle δ and an azimuthal angle ϕ_n. The magnetic field direction is specified by an angle β, which corresponds to the angle between the magnetic field and the spinning axis, and a continuously changing angle $\phi_m = \omega t$. It is then straightforward to determine the time dependence of the angle α between the magnetic field and director axis. The average value of the potential energy over one rotor period is:

$$\begin{aligned} \langle E \rangle &= -\frac{1}{3}\Delta\chi B_0^2 \left[\frac{3\cos^2\beta - 1}{2}\right]\left[\frac{3\cos^2\delta - 1}{2}\right] \\ &= \frac{1}{3}\Delta\chi B_0^2 f(\delta,\beta) \end{aligned} \tag{5.5}$$

From the Eq (5.5), we see that for a given angle β, the average energy value $\langle E \rangle$ depends solely on the polar angle δ.

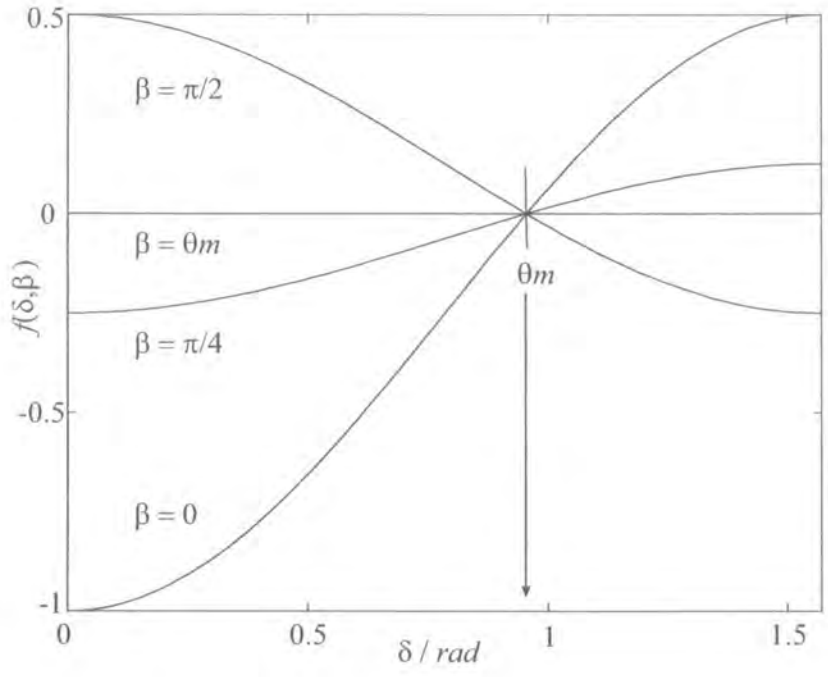

Figure 5.2 Plot of the function $f(\delta,\beta)$. When the liquid crystal is spun at magic angle, $f(\delta,\beta)$ is always zero.

For liquid crystals with a $\Delta\chi > 0$, the minimum of the potential energy is found at $\delta = 0°$ for β less than the magic angle, θ_m, i.e. the director is aligned with the spinning axis. In the case of $\beta > \theta m$, the minimum is at $\delta = \pi/2$ and the local directors are uniformly distributed in a plane perpendicular to the spinning axis. In the special case where $\beta = \theta m$, the minimum of the energy is independent of the angle δ, i.e. there is no preferred director orientation. Across the sample, only a short range of the nematic order is preserved, and the orientations of the local domain are uniformly distributed over the solid angle.

As a result, nematic liquid crystals, spinning at exactly the magic angle, can be considered in terms of its NMR in the same way as a powdered solid. Unlike solids, however, the molecular tumbling in liquid crystals removes the intermolecular interactions; the NMR signal is entirely governed by intramolecular interactions.

5.2.2 ^{13}C-NMR of liquid crystals under MAS

On static ^{13}C spectrum of mono-fluorinate liquid crystal, such as I35, due dipolar plus *J*-coupling interactions between ^{13}C and ^{19}F nuclei the individual ^{13}C resonance should split into a doublet. As demonstrated in the previous chapter, CW-decoupled spectra shows an unusual broadening of C—F doublet [7], or even additional splitting in one of its components while the other peak remains relatively sharp. In order to establish whether or not this class of effects has a more general character we extended the previous experiments to the case of rotating samples. The corresponding ^{13}C spectrum under magic angle spinning [4, 8-16], because the C—F dipolar interactions are scaled to zero, the ^{13}C resonances should be split into a doublets only by the non-zero J_{CF} scalar interactions. Nevertheless, as clearly visible from the Figure 5.3, the CW ^{1}H-decoupling splits the individual components of the expected C2-doublet (^{13}C directly bonded to ^{19}F) into a further broad doublet. Unlike the static case, now the additional splittings are approximately equally spaced on both components, moreover its dependence from the shift of ^{1}H-trasmitter [15] appears negligible within the range of ± 5 kHz. The C3 peak also is strongly affected by the CW decoupling. As C2 the C3 carbon is interacting with ^{19}F nucleus but now through the double bond *J*-coupling, so that only a little splitting is expected (~ 20 Hz in this compound). Conversely the C3 multiplet shows the principal splitting of order of ~ 80 Hz, while one of component further splits into a doublet. As seen in Figure 5.3, unlike the C2 splitting, the C3 pattern shows a clear dependence from the ^{1}H-shift, exchanging the minor splitting from one component to the other one.

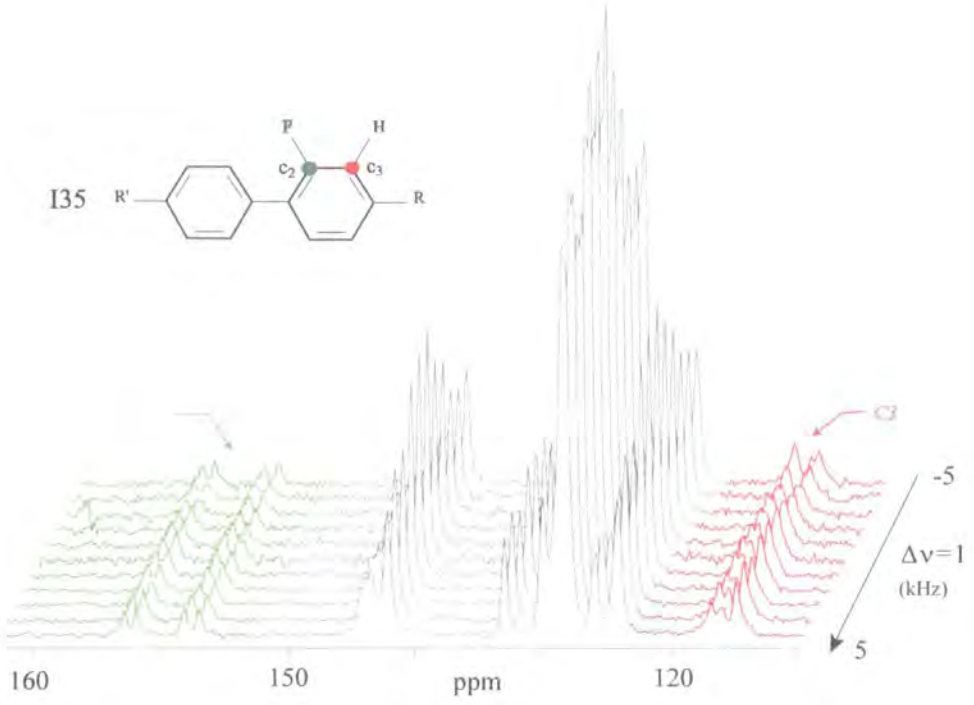

Figure 5.3 ^{13}C spectra expansion of aromatic region of I35 in the nematic phase. The spectra were performed under MAS with a spinning speed of 1.8 kHz. ^{1}H-CW decoupling also has been applied varying the ^{1}H-offset within the range ± 5kHz with a step of 1kHz, and decoupling power 50kHz. The nematic phase was maintained at 40°. Acquisition parameters were: pulse duration 5 μs, contact time 3ms, and recycle delay 6s, number of transient 800.

As in the static case, the broadening and splittings observed under magic angle spinning are strongly dependent on the decoupling sequence used. In fact by using phase–modulated ^{1}H-decoupling, such as TPPM, with a simple optimisation of the tip angle ß (nutation angle of ^{1}H-maganatisation in RF-frame), the broadening effects are strongly reduced. As we can see in the Figure 5.4, for "small" tip ß angles the performance of TPPM is comparable with CW, as the tip angle increases the decoupling becomes more effective recovering well resolved C2 doublet and relatively sharp C3 peak when a tip of 180° is reached. The ^{1}H off-resonance optimisation, like CW, was not particularly relevant for C2-resonaces, while for the peak C3 better resolution was found when the ^{1}H transmitter displaced ~ 1kHz from the zero-offset condition. As shown in the Figure 5.5, the best resolution over the entire spectral width was achieved by using SPINAL-64, in particular for the C3

peak has been possible to observe the double-bond $^2J_{CF}$ splitting, which is about ~21 Hz. This is consistent with previous solution data as reported in reference [17]. Like TPPM, SPINAL-64 consists of a train of pulses with a fixed tip angle β (around 170°), and the decoupling performance should be optimised with respect to this angle. Unlike TPPM, varying the tip angle within the same range, C2 and C3 resonances are quite resolved even at small tip angle, although the best performance was found with a tip of ~180°.

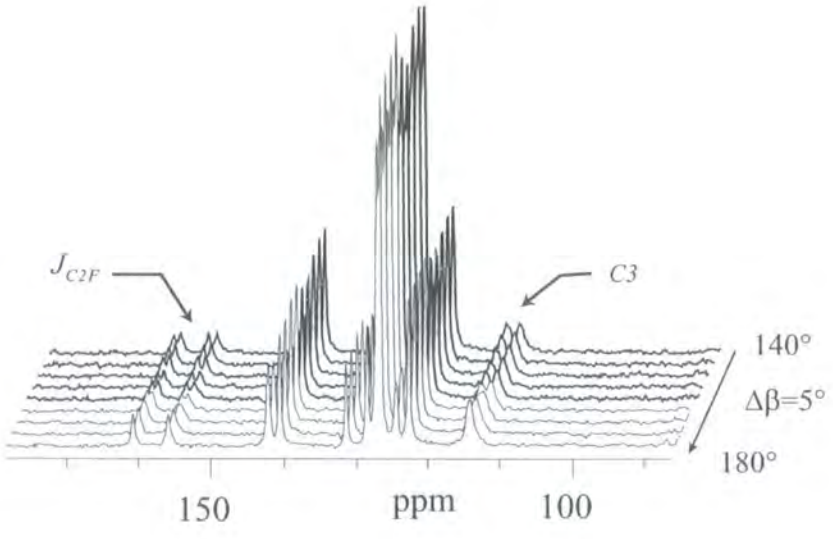

Figure 5.4 ^{13}C spectra expansion of aromatic region of I35 in the nematic phase. The spectra were performed under MAS with a spinning speed of 1.8 kHz. ^1H-TPPM decoupling also has been applied using a phase angle φ of 15° and varying the tip angle ß within the range 140°÷180° with a step of 5°. The decoupling power was 50 kHz and the best ^1H-offset, 1 kHz. The nematic phase was maintained at 40°. Acquisition parameters were: pulse duration 5 μs, contact time 3ms, and recycle delay 6s, number of transient 800. C2 linewidth, ~ 23 Hz, while for C3 ~55 Hz

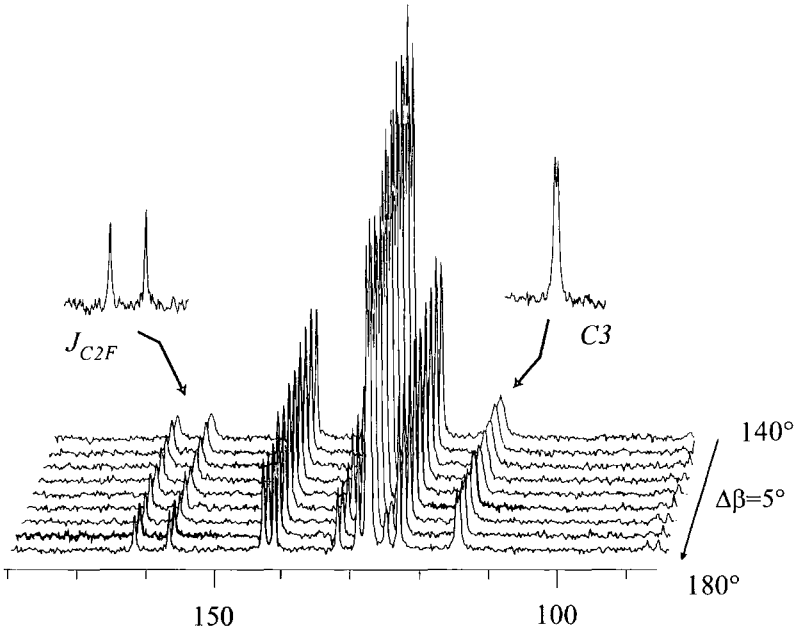

Figure 5.5 ^{13}C spectra expansion of aromatic region of I35 in the nematic phase. The spectra were performed under MAS with a spinning speed of 1.8 kHz. ^{1}H-SPINAL-64 decoupling also has been applied varying the tip angle ß within the range 140°÷180° with a step of 5°. The decoupling power was 50 kHz and the best ^{1}H-offset, 1 kHz. The nematic phase was maintained at 40°. Acquisition parameters were: pulse duration 5 μs, contact time 3ms, and recycle delay 6s, number of transient 800. C2 linewidth, ~ 12 Hz, while for C3 the $^{2}J_{CF}$ is ~ 21 Hz

The experiments were performed on a Chemagnetics CMX spectrometer operating at a proton Lamor frequency of 200.13 MHz, using a standard double-resonance MAS probe. The I35 in solid phase was packed in a rotor of 7.5 mm and using a temperature controller the temperature of the mesophase was stabilized at 40°. It is important to ensure that the magic angle is correctly set. Away from the magic angle, the local directors are either aligned along the spinning axis or distribute uniformly in a plane perpendicular with respect to this axis. The magic angle condition was tested using the sample KBr, and rotor-echoes where observed until 12 ms on FID. The resolution was checked measuring the ^{13}C linewidth on adamantane with a spinning speed of 2 kHz. The shimming was optimised until a linewidth of ~5 Hz was achieved, which is close to the limit of possible resolution on these solid-state probes. Since the phase-modulated decoupling sequences are

quite sensitive with respect to the tip angle parameter, particular care was taken in the calibration of ^{1}H pulse excitation.

5.2.3 Analysis of line splittings and broadening effects under MAS

Due to the fast relative motion between the molecules the broadening effects is entirely governed by intramolecular interaction. Moreover as we know from the static case, the relevant intramolecular interactions for both carbons C2 and C3 are due to the nearest ^{1}H and single ^{19}F present in the molecule. Following the same procedure as in the static case we represent the C—F-H Hamiltonian under ^{1}H-decoupling in α and β ^{19}F subspace, Eq. (5.6). It is straightforward to see that in this representation the C—F-H spin system can be regarded as a two effective "C—H" systems relative to the α, β ^{19}F states. In fact according to Eq. (5.6), due to both C—F and H—F dipolar interactions the ^{19}F spin states behave as an effective ^{13}C-CSA and an effective ^{1}H-CSA respectively.

$$H_{\alpha/\beta}(t)=\left(\delta_C(t)\pm d_{CF}(t)\pm\frac{J_{CF}}{2}\right)I_z^C+2d_{CH}(t)I_z^CI_z^H+\left(\delta_H(t)\pm d_{HF}(t)\right)I_z^H+H_{RF}(t) \tag{5.6}$$

where all the tensor interactions are now time dependent due to the mechanical rotation. The time-dependent Hamiltonian $H_{RF}(t)$ represents the interaction in the rotating frame between the ^{1}H spins and the RF field:

$$H_{RF}(t)=\nu_{RF}\left(I_x^H\cos\phi(t)+I_y^H\sin\phi(t)\right) \tag{5.7}$$

In order to reproduce the effects above observed we performed a simulation of the C2 signal using the same set of interaction constants as in the static case (see Chapter-4) and giving the ^{1}H-offset, $\Delta\nu$, as a parameter of simulation. In agreement

with observation the J_{CF} line splitting remains unaffected by any variation of the ^{1}H-offset within the range ± 5 kHz. Obviously the offset-range in which the ^{13}C line splitting remains substantially unaffected by the ^{1}H-offset irradiation depend on both the size of C—H dipolar coupling and the strength of the RF-field. On the other hand the simulation confirms that the rationalization of these effects as due to an off-resonance irradiation does not apply here. In the static case the C—F line splitting effects was entirely governed by the term $\Delta\nu \pm d_{HF}$ (see Chapter 4), so that as the ^{1}H-offset $\Delta\nu$ is the same of $|d_{HF}|$, one component of the doublet is on-resonance condition (sharp peak) while the other one is irradiated with a large ^{1}H-offset (broad peak, or even line splitting). As previously demonstrated by the simulation and experiments, indeed, the line splitting effect reveals this strong dependence from the effective offset term $\Delta\nu \pm d_{HF}$. Simulations under magic angle spinning show that the ^{1}H-CSA plays the same role as $\Delta\nu$ in the static case. So that according to the Hamiltonian given in Eq. (5.6), in the limit of negligible effect from $\Delta\nu$, here the $^{1}J_{CF}$ line splittings and broadening are entirely governed by the tensor quantity $\delta_H \pm d_{HF}$.

The results of some simulations are shown in the Figure 5.6.

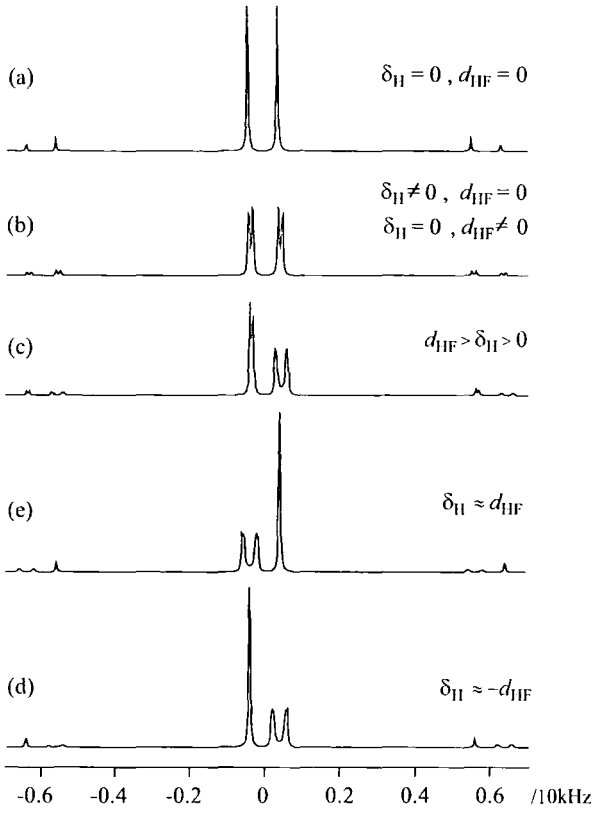

Figure 5.6 Simulated pattern of the $^1J_{CF}$ splitting in a C—H—F spins system under magic angle spinning The simulation was performed using CW ^{1}H decoupling and varying the ^{1}H CSA, δ_H, and the dipolar tensor d_{HF} (all the tensor interactions are collinear). ^{1}H-offset has been ignored because it has no relevant effects on the line splitting. Full $^1J_{CF}$ splitting is recovered when δ_H and d_{HF} are both zero (a), with a non-zero δ_H or d_{HF}, or non-zero δ_H and d_{HF}, no genuine $^1J_{CF}$ splitting is observed (b-e).

The assumption of the collinear tensors in the simulation of Figure 5.6 is justified because the molecules in the nematic phase effective rapid re-orientation perpendicular to the director axis reduces tensor interactions to their projections along the director. In solids, however, we will also need to define the relative orientation of the tensor interactions. Assuming the chemical tensor, δ_H axially symmetric so that only one Euler angle, say β, is necessary to describe the relative orientation of the principal axis system of the two tensors. Under previous assumption we simulated the J_{CF} splitting pattern changing the relative orientation

between δ_H and d_{HF} tensors varying the Euler angle β. The results are illustrated in Figure 5.7.

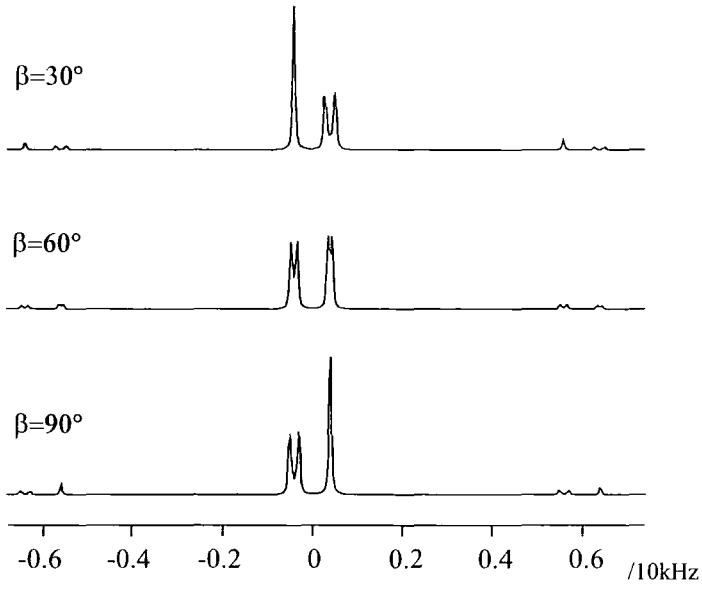

Figure 5.7 Effect on $^1J_{CF}$ splitting of the relative orientation between the PAS' ^{1}H CSA and PAS' H—F dipolar tensor. ^{1}H CSA tensor is assumed symmetric so that only angle β is necessary to describe the relative orientation between those tensors' PAS. The simulation was performed in a C—H—F system using CW ^{1}H decoupling under MAS.

The simulations demonstrate that the large splitting effect observed on the C2 and C3 carbons is due to the proximity of ^{1}H and ^{19}F nuclei. We can get some insight into the case of simple CW decoupling (where there is a single time dependence due to the mechanical rotation) using Average Hamiltonian theory (AHT), [18-21] following the treatment of Ernst [22, 23] who first described analogous effects in a simple two-spin system.

If the decoupling field is relatively strong, i.e. $\nu_{RF} >> \nu_R$, it is convenient to determine the average Hamiltonian in the reference frame defined by the RF interaction. The zero- and first-order Hamiltonians are given by:

$$\bar{H}^{(0)} = \left(J_{CF} - 2d_{CF}\left(\Omega_{CF}\right)\right) I_z^C I_z^F \tag{5.8}$$

$$\bar{H}^{(1)} = \frac{1}{2\omega_{RF}}\left(\delta_H^2(\Omega_H) + d_{CH}^2(\Omega_{CH}) + d_{HF}^2(\Omega_{HF})\right) I_x^H$$
$$\frac{-2\delta_H(\Omega_H) d_{CH}(\Omega_{CH}) I_x^H I_z^F}{\omega_{RF}} + \frac{4 d_{CH}(\Omega_{CH}) d_{HF}(\Omega_{HF}) I_z^C I_z^F I_x^H}{\omega_{RF}} \tag{5.9}$$

The magic angle spinning removes all second rank interactions in the zero-order average Hamiltonian, leaving just the J_{CF} coupling. The first-order correction, Eq (5.9), contains the product of two second-rank tensors. This product can be reduced to a sum of zero-rank, second-rank and fourth-rank tensors [24] i.e. a (small) isotropic shift, a second rank term, which is removed by the magic-angle spinning, and a fourth rank term, which is not. This last term results in an orientation-dependent line broadening.

In the C—H—F system, this term depends of the ^{19}F spin state:

$$\bar{H}^{(1)}_{\alpha/\beta} \propto \frac{-2 d_{CH}(\Omega_{CH})\left[\delta_H(\Omega_H) \pm d_{HF}(\Omega_{HF})\right] I_z^C I_x^H}{\omega_{RF}} \tag{5.10}$$

These analytical calculations explain the reasons why the individual C—F resonances split into a further well-defined doublet (C2). The single C2-resonances are associated to a different contribution, adding or subtracting the H—F dipolar coupling to ^{1}H-CSA according as the ^{19}F state. Nevertheless the C2 doublet (Figure 5.3) exhibits a line splitting on both components quite symmetric. This may be due to the dominating large dipolar tensor d_{HF} against the ^{1}H CSA anisotropy, which are quite small in general.

The same explanation applies for the C3 peak, even if some clarifications seem to be necessary. Due to the quite small $^2J_{C3F}$ interaction, an order of magnitude less than the $^1J_{C2F}$, the undesirable splitting on both components of the doublet may be comparable with the $^2J_{C3F}$ splitting, so that we should observe the C3 peaks to split into a "doublet of doublets". The observations instead show an asymmetric triplet with a well defined modulation by the ^{1}H-offset irradiation.

The reason for this unusual behaviour, in the context of previous analysis, may be that for the C3 carbon we need to involve also the scalar interaction J_{C3H}, which is negligible for the C2 carbon.

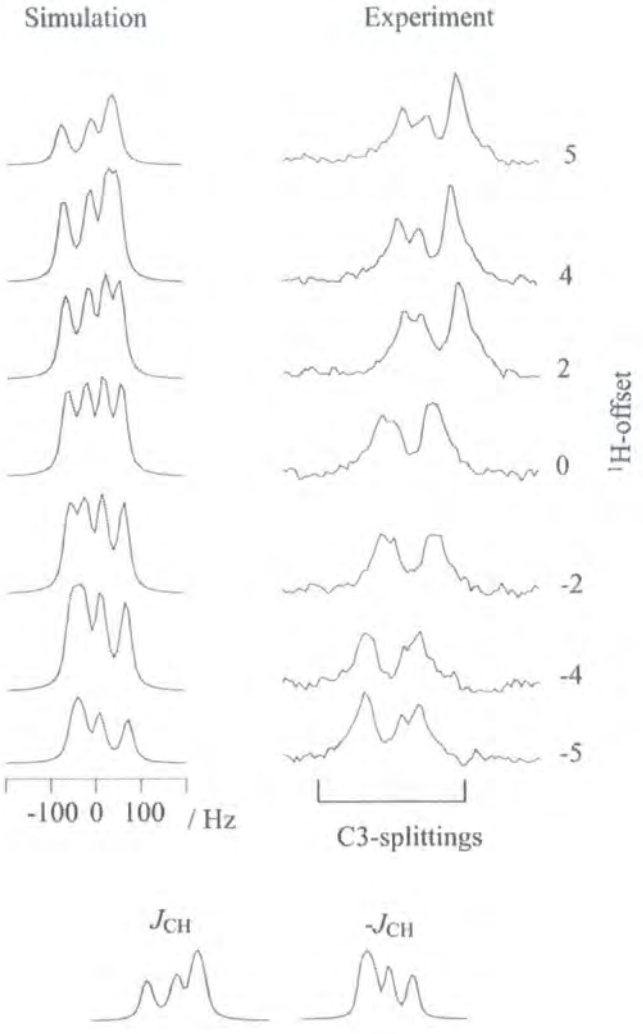

Figure 5.8 Comparison between experiment and simulation of C3 carbon splittings with ^{1}H CW decoupling as function of offset. The experimental data set derives from the selected portion of the ^{13}C spectra of Figure 5.3, while the C3 signal has been simulated using a C—H—F spin system varying the ^{1}H-offset as shown in Figure. As in the experiment the decoupling power was of 50 kHz and the spinning speed of 2.8 kHz. The other simulation parameters were: ^{1}H CSA of 1 kHz, J_{CH}, 160 Hz, J_{CF}, 22 Hz, d_{CH}, 2.5 kHz, d_{HF}, 5 kHz d_{CF}, 2 kHz and δ_H^{iso}, 1 kHz. All the tensor quantities were assumed collinear.

If in Eq (5.10) we make the substitution, $d_{CH} \rightarrow d_{CH} + {}^{1}J_{CH}$, at first-order in the average Hamiltonian we find a scalar term dependent by ^{1}H-offset:

$$\frac{2\,{}^{1}J_{CH}\delta_{H}^{iso}}{\omega_{RF}} I_{z}^{C} I_{x}^{H} \tag{5.11}$$

If the large splitting is quite small as in our case (~80Hz), the term of the Eq (5.11) may give an observable modulation of C3 pattern. This is clearly seen in the simulations of Figure 5.8, which reproduce the experimental dependence of C3 splittings on ^{1}H-offset. However the relevant aspect of these simulations is that as the sign of J_{CH} is reversed (bottom of Figure) the C3 pattern swaps around the zero-point of frequency axis. This demonstrates that the offset dependence of C3 splittings is exclusively due to the presence of $^{1}J_{C3H}$ interaction, which is of about ~160 Hz. Consistently in C2 carbon no offset dependence is visible since double-bond $^{2}J_{C2H}$ is quite small in comparison with $^{1}J_{C3H}$. This remarkable correspondence between experiments and simulations confirms that the theoretical predictions based on the first order approximation in AHT theory are sufficient to explain these effects.

As previously demonstrated [22], the line splitting effects can be strongly reduced (or eliminated) using phase-modulated decoupling sequences, such as TPPM. This can be confirmed in numerical simulation. The Figure 5.9 shows a series of simulated spectra in a C—H—F system with TPPM sequence under MAS condition:

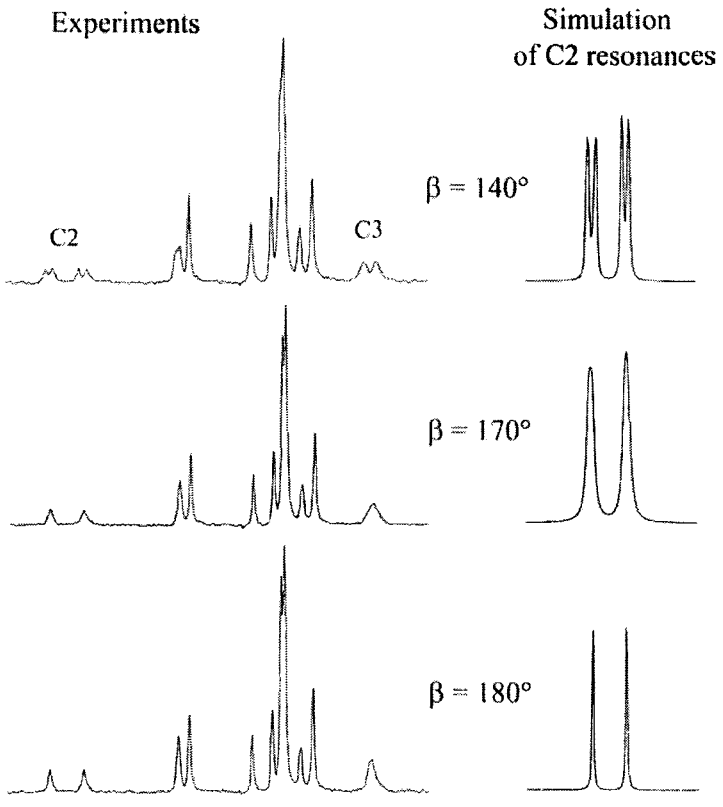

Figure 5.9 (Left) Effect of MAS ^{1}H-TPPM on ^{13}C-linewidth varying the tip angles β with phase difference fixed at $\Delta\varphi = 14^{\circ}$ (See experiments of Figure 5.4). (Right) Numerical simulations of the C2 doublet in a C—H—F spin system, using the experimental values for spinning speed and decoupling parameters. The other simulation parameters were: ^{1}H CSA 1 kHz J_{CF}, 250 Hz, d_{CH}, 8 kHz, d_{HF}, -5 kHz, d_{CF}, 2 kHz. All the tensor quantities were assumed collinear. The simulated and experimental spectra are plotted in different scales.

As seen in Figure 5.9 the numerical simulation of C2 splittings are perfectly in agreement with the experiments. It is straightforward to realize that similar simulations, also apply for the C3 splittings. Although we have lost the simple physical picture of the line splitting effects as that in the static case, however we have demonstrated through the simulation that the C—H—F system behaves as two effective "C—H" systems. Moreover the analytical calculation using the average Hamiltonian gives a good description of the effects observed, leaving some physical

insight explaining those effects as due to a recoupling between the C—H tensor with the effective ^{1}H-CSA tensors respectively in the α and β ^{19}F subspaces.

5.3 Observations on conventional solids

5.3.1 Preliminary experiments and discussion

In this section we extend the previous experiments performed on I35 in the nematic phase to solid samples.

As well established in solid-state NMR, combining magic-angle spinning with strong proton decoupling we, usually, obtain relatively high resolution in the spectra of dilute spins, such as ^{13}C. In previous studies of fluorine-containing organic molecules [25], the linewidths of ^{13}C resonances in proximity to the ^{19}F are strongly degraded in comparison with the other peaks. This can be seen in the ^{13}C MAS spectra of Figure 5.10 for Flurbiprofen. As we can see, using CW and TPPM (a-b) decoupling methods, the C2 and C3 resonances are much less resolved with respect to the rest of the other peaks across of the entire spectral width.

In particular the individual components of the *J*-splitting of the C2 carbon bonded to the ^{19}F nucleus is quite broad, especially if compared to liquid crystal case. This shows how in the rigid solids the resolution is strongly affected by the stronger dipolar interaction interactions, considering that the C2 carbon either on the Flurbiprofen and I35 has the same pattern of interactions, but in the latter case the rapid molecular reorientation scales the intramolecular interactions and averages out all the intermolecular ones. This is illustrated in Figure 5.11, comparing the best MAS ^{13}C spectra of I35 both in the nematic phase and in the solid phase using ^{1}H SPINAL-64. As the liquid crystal is cooled below the mesophase temperature the molecular motion is strongly reduced, or even fully quenched. Under this condition with all interactions restored the performance of SPINAL-64 results degraded across of the entire spectral width. This is clearly seen as we compare the ^{13}C spectra of Figure 5.11. In particular the biggest difference between the solid and nematic spectrum is visible for the C2 and C3 resonances. Deconvolution of the C2 doublet shows the TPPM linewidth is reduced by 30% compared to CW decoupling. Making

the same comparison in I35 experiments we find approximately that ratio between TPPM and CW performance.

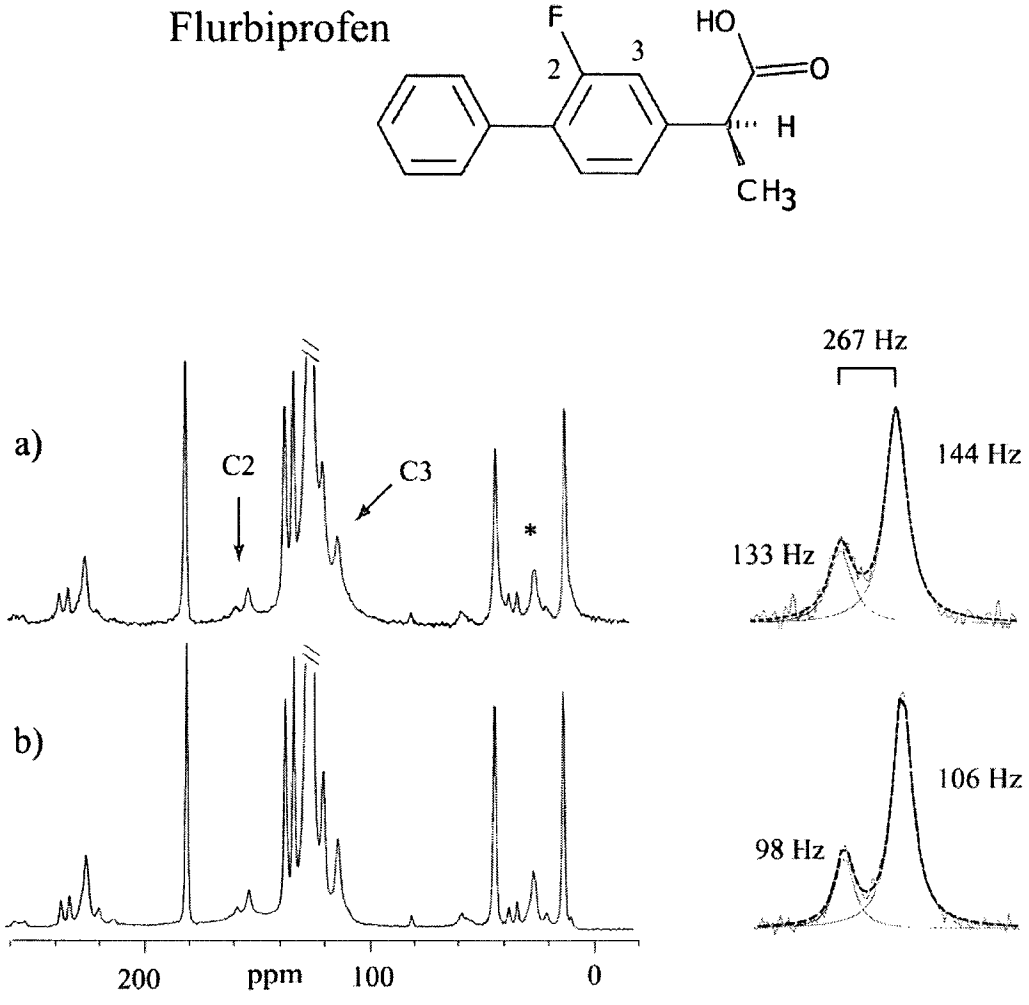

Figure 5.10 ^{13}C-spectra of Flurbiprofen using various ^{1}H-decoupling methods: in (a) CW, and in (b) TPPM, with tip angle a β of 180° and phase angle φ of 14°. The ^{1}H decoupling was 50 kHz and spinning speed 5 kHz. Expansion show the fit of the two components of J_{CF} of C2 to Lorentzian line shapes (the numbers are the fitted FWHH linewidths). Acquisition parameters were: ^{1}H pulse duration 5 μ, contact time 3 ms and recycle delay 15 s.

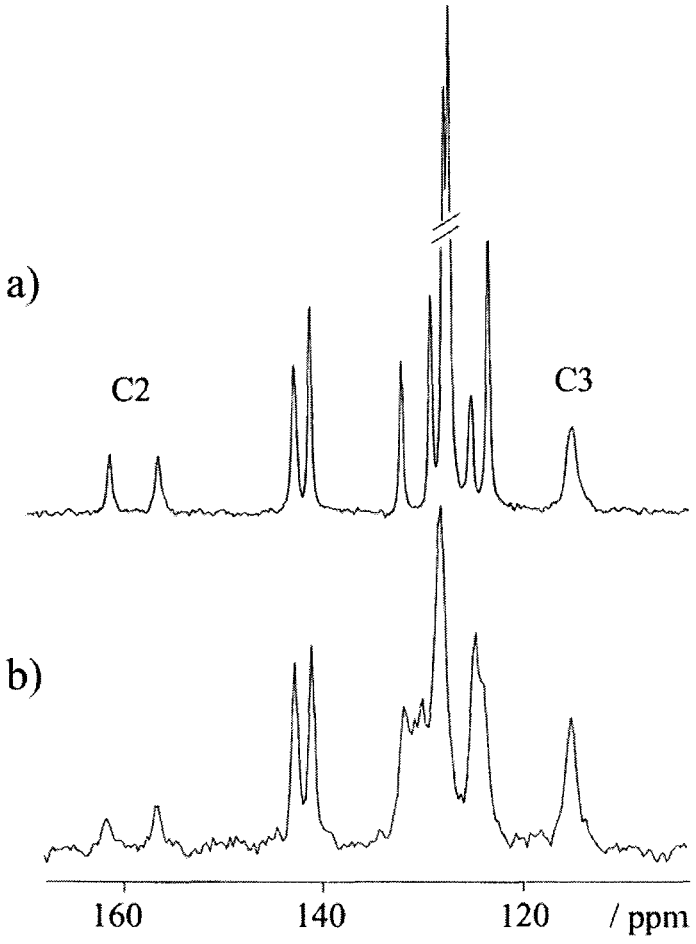

Figure 5.11 Comparison between ^{13}C MAS-spectra of I35 using ^{1}H SPINAL-64. At the top (a), ^{13}C spectrum acquired in the nematic phase (T=40°C) with spinning speed 2.8 kHz, while in (b) ^{13}C spectrum in solid phase (T=15°C) and spinning speed of 3.5 kHz. In both cases the decoupling field strength was 50 kHz.

In both cases we observe an asymmetric C2 pattern with both linewidths and line area unequal. With TPPM the resolution is still poor, but the difference in linewidth between the both peaks is less than that in CW. However the CW broadening is sensibly greater than that with TPPM decoupling.

The origin of the difference in *area* can be found by inspection of the C—H—F Hamiltonian of Eq (5.12). The C—F dipolar tensor is added or subtracted to ^{13}C-CSA tensor according to the ^{19}F α and β states. This means that the centre bands

"α"and "β" at frequency positions $\delta_C^{iso} \pm \frac{J_{CF}}{2}$ are associated with two different effective ^{13}C CSAs $\pm d_{CF}(t) + \delta_C(t)$ as seen below in Eq (5.12). As a result, the two spinning sideband manifolds will have a different distribution of intensities. Since the total intensities of the two sideband manifolds [26-29] are equal, strong effective ^{13}C CSA, say α state, gives to a wide range of spinning sidebands, which corresponds to a weak centre band intensity, vice versa weak effective ^{13}C CSA, say β state, results in a smaller number of spinning sidebands, which gives strong centre band intensity. Again, this effect has been previously described for simple two-spin systems [30].

$$H_{\alpha/\beta} = \left[\pm \frac{J_{CF}}{2} \pm d_{CF}(t) + \delta_C(t) \right] I_z^C + 2 d_{CH}(t) I_z^F I_z^H + \left[\delta_H(t) \pm d_{HF}(t) \right] I_z^H + H_{RF}(t) \tag{5.12}$$

The simulations reported in the Figure 5.12 confirm the above statements showing that as the spinning speed increases the difference in the centre bands intensities results markedly reduced. Although the C2 doublet of Flurbiprofen at spinning speed of 5 kHz (Figure 5.10) exhibits a substantial difference in the peak intensities, no spinning sidebands are observed across ^{13}C spectrum. This is due to the small signal to noise ratio associated with C2 doublet in comparison with that of the other ^{13}C resonances. However the experimental observation is in agreement with the above theoretical predictions. As shown in Figure 5.13, increasing the spinning speed from 5 kHz to 15 kHz the unbalance in peak intensities is substantially reduced.

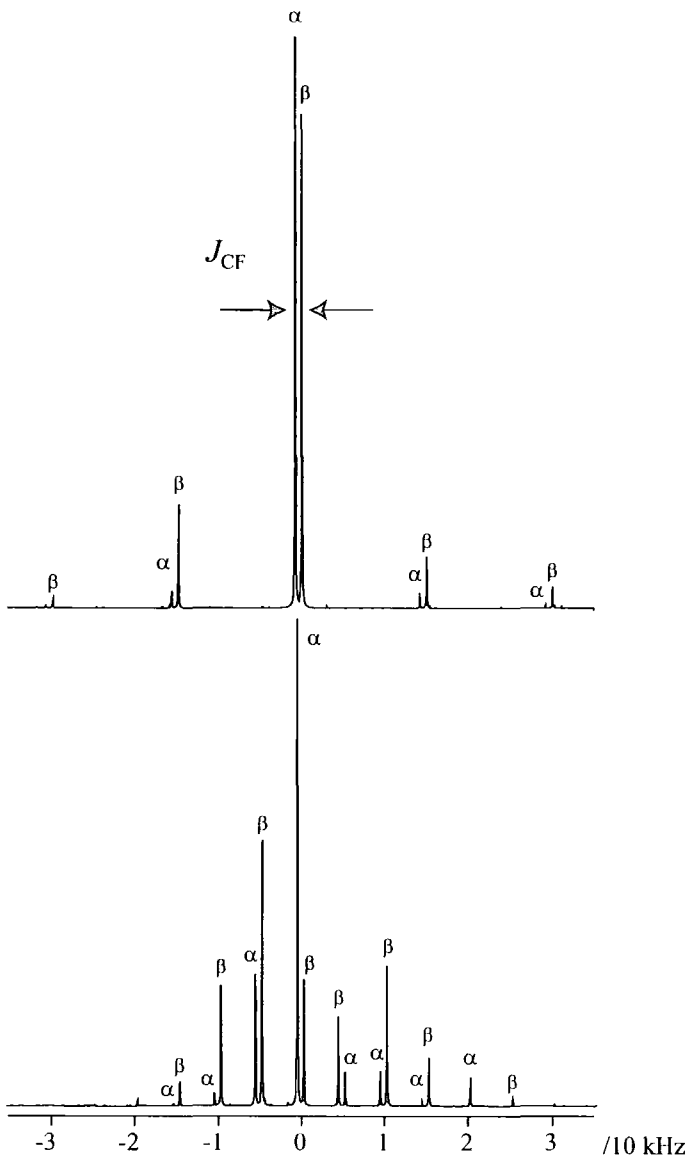

Figure 5.12 Simulation of the ^{13}C spinning sideband pattern n a C—H—F spin system at spinning speeds of 15 kHz (top) and 5 kHz (bottom) using 50 kHz TPPM ^{1}H decoupling (with tip angle $\beta = 180^\circ$ and $\Delta\phi = 14^\circ$). Co-linear tensor quantities were assumed for the sake of simplicity. The other simulation parameters were: ^{1}H CSA of 2 kHz, ^{13}C CSA of 15 kHz, d_{HF}, 6 kHz, d_{CH} 8 kHz, d_{CF}, 4 kHz, J_{CF}, 800 Hz.

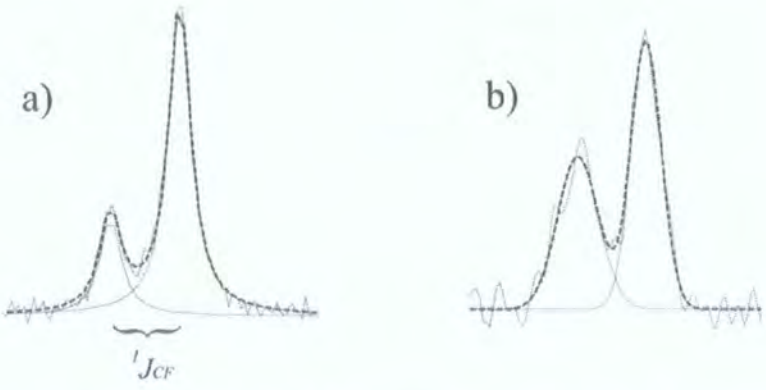

Figure 5.13 Expansion of C2-doublet from ^{13}C spectra on Flurbiprofen with ^1H TPPM decoupling as a function of the spinning speed. At the top, (a), the spinning speed was 5 kHz, while on the bottom (b), 15 kHz. ^1H TPPM parameters: ^1H decoupling power was 50 kHz, tip angle 180° and phase angle φ 14°. Acquisition parameters: pulse duration 5 μ, contact time 3 ms and recycle delay 15 s.

Tab 1. This table displays the fitting parameters of the J_{CF} doublets of Flurbiprofen reported in Figure 5.13. 1ppm here corresponds to 50.32 Hz.

Model: Lorentz	Spinning speed 5 kHz	
$R^2 = 0.99129$	Peak Area	FWHH / ppm
Peak 1	9737±263	1.95±0.099
Peak 2	33589±275	2.1±0.035
Model: Gauss	Spinning speed 15 kHz	
$R^2 = 0.962$	Peak Area	FWHH / ppm
Peak 1	6588±316	2.99±0.15
Peak 2	8763±269	2.30±0.07

As expected, at high spinning speed, the difference in the peak intensities starts to be reduced, but at the same time with respect to low spinning regime, the overall resolution degrades and an appreciable asymmetry in the peak linewidth. Moreover the appearance of the peak shape is Gaussian-like rather than Lorentzian-like as in the low spinning speed (see Tab 1). These effects could be related to an interference between the timescales of decoupling and spinning, but this question has not been pursued further in this study.

5.4 Off MAS effect on J_{CF} splittings

The off magic angle spinning technique [5, 31] (VASS) is currently applied to assign the peaks of the spectra of labelled compound, such as liquid crystals. By varying the angle ϑ of the spinner axis away from the direction the static field, all tensor interactions are scaled by a factor χ:

$$\chi = \frac{3\cos^2(\vartheta) - 1}{2}$$

Obviously at magic angle the scaling factor is zero, which means that only the isotropic part of tensor interactions are preserved. A slight mismatch of the magic angle will result re-introduction of the anisotropic interactions (scaled powder patterns in the case of powder samples). A minimal deviation of scaling factor χ from zero multiplied by a large coupling constant can result in significant effects in the spectrum. For instance, hexamethyl benzene is widely used as a magic angle calibration sample as the aromatic ^{13}C signal is strongly sensitive to variations of the rotor angle. We observed the same effect in ^{13}C spectra of Flurbiprofen, where a small deviation from the magic angle condition causes an apparent reduction of J_{CF} splitting. The experimental results are shown in the Figure 5.14 on the left. In the case a), (misset rotor angle), the effective J_{CF} splitting appears reduced of a factor around 0.2 than that observed in b), where the rotor angle has been carefully set. The strength of the splitting in b) is in agreement with the results obtained from the solution spectra, which was of ~250 Hz.

The resultant line broadening of the centerband depends on the size of the effective CSA, which is the sum or difference of the ^{13}C CSA and the C—F dipolar interaction, depending on the ^{19}F spin state. We can see in Figure 5.14 that one component of the doublet is less affected than the other by the off magic angle effects. In fact in both cases, one of these resonances keeps the same position on the frequency axes, while the other one moves toward the barycentre of the doublet.

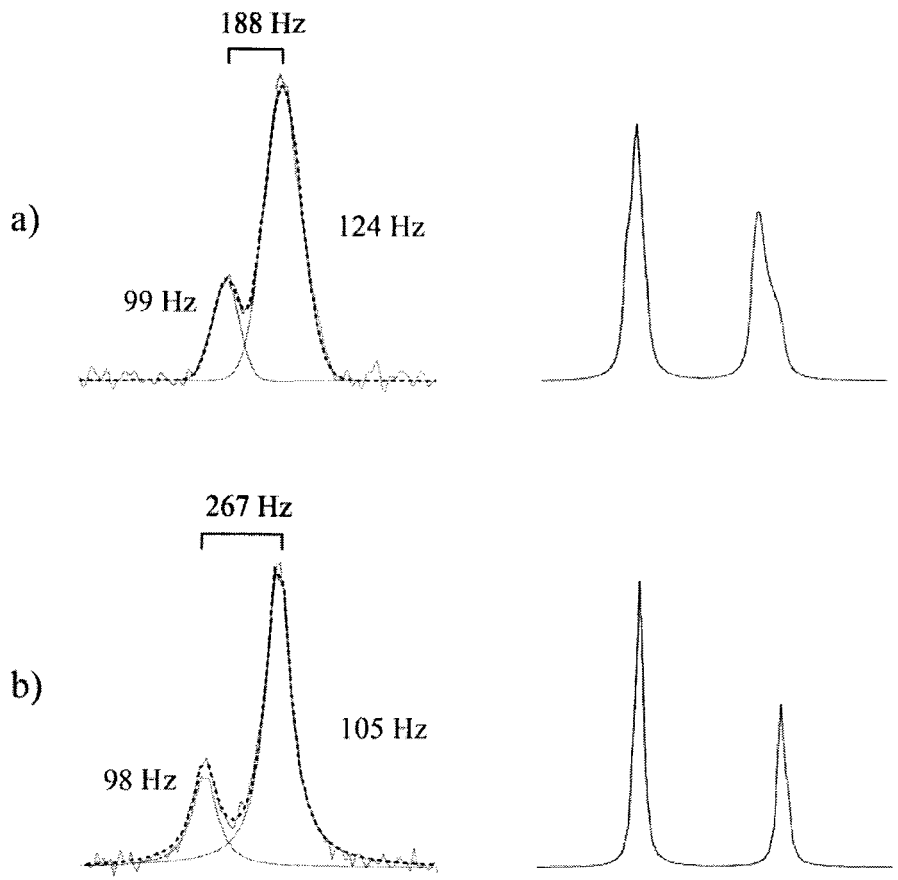

Figure 5.14 Qualitative comparison between experimental and simulation of the magic angle spinning mismatching, with 50 kHz TPPM ^{1}H decoupling (with tip angle $\beta = 180^{\circ}$ and $\Delta\phi = 14^{\circ}$). In a), on the left J_{CF} splitting under slight off-MAS, while, b), on-MAS. The splitting, in a), appears considerably reduced with respect to the case b). Moreover, the resolution of the individual peaks is degraded. On the right, the simulation in a C—H—F spin system reproduce these effects, a), off-MAS, and, b), on-MAS. In both, experiment and simulation the spinning speed used was 5 kHz and the other simulation parameter were: ^{1}H CSA of 2 kHz, ^{13}C CSA of 15 kHz, d_{HF}, 6 kHz, d_{CH} 8 kHz, d_{CF}, 4 kHz, J_{CF}, 250 Hz and the rotor angle was off magic angle of 0.44%. The experimental and simulated doublets are plotted in different scales.

The effective CSA is $\delta_C \pm d_{CF}$, and so the cases where the ^{13}C CSA and dipolar interactions have the same or different signs can be distinguished. In the first case one of these peaks moves toward the barycentre, while in the second circumstance this peak moves in the opposite direction going away from the barycentre itself. In

the Figure 5.14, on the right, are shown the results of the simulation, which are qualitatively in agreement with the experimental observations. Obviously which peak is moving depends on the relative sign of the J_{CF} coupling with respect to sign of the ^{13}C CSA and C—F dipolar tensor interaction. Outlining we can say that a mismatch of the magic angle introduce an additional broadening which distorts the individual components of *J*-doublet hampering any observation of real *J*-coupling.

5.5 Effect of F—F interactions on ^{13}C-linewidth of J_{CF} splittings

5.5.1 Introduction

As previously discussed, the ^{13}C linewidth in a C—H—F system, under MAS and ^{1}H-decoupling, depends on many factors. The predominant spin dynamics effects stem from the interactions between RF-field and tensor interactions giving rise an asymmetric broadening of the J_{CF}-doublet, depending on the ^{19}F state. The removal of this asymmetry depends on the decoupling scheme used. The experimental observations and theoretical calculation show that using the TPPM sequence, the individual components of the J_{CF} splitting are evenly broadened, but their intrinsic resolution is still poor in comparison with the rest of the ^{13}C resonances across the spectrum. In this section, we investigate additional sources of line broadening which may explain the relative difficulty of resolving C—F interactions in solid systems.

5.5.2 Analysis on different systems

So far most of our discussion has focussed on ^{1}H CW decoupling and related effects of broadening on C—F—H system under magic angle spinning. Although we found those effects are strongly scaled by using TPPM decoupling, the resolution of the C—F doublet on Flurbiprofen is still unsatisfactory, while the rest of the carbon resonances across the spectrum are around two times narrower.

In Figure 5.15 we show a comparison of the ^{13}C spectra of I35, Flurbiprofen and 3-fluoro-4-methyl-benzoic acid molecules. All three molecules contain a mono-

fluorinated phenyl ring so that the intramolecular dipolar couplings of C—F—H system are the same. In all three cases, we used TPPM ^{1}H decoupling under MAS.

The first thing we can note is that the best resolution of J_{CF} splitting has been observed spinning I35 in the nematic phase. In contrast, the resolution of the C—F doublet on Flurbiprofen is still unsatisfactory or even completely lost as seen in 3-fluoro-4-methyl-benzoic acid, where the J_{CF} doublet lumps in a single very broad peak. Although we carried out many experiments, varying the spinning speed and also using different ^{1}H decoupling schemes, no significant improvement on resolution has been observed. As for the C3 peak, however, the resolution is significantly improved using TPPM instead of CW decoupling.

There are two significant differences between I35 and the other two molecules. One of these is related to the intermolecular interactions acting on C—F—H system. In I35, due to the molecular tumbling, the C—F—H system is not interacting with nuclear spins belonging to other molecules in the sample, i.e. no effects from intermolecular interactions on ^{1}H decoupled ^{13}C spectrum are expected. In contrast, Flurbiprofen and 3-fluoro-4-methyl-benzoic acid are both rigid solids. So that the isolated C—F—H system in I35, due to the intermolecular dipolar couplings is now interacting with both ^{19}F and ^{1}H spins. The other important distinction between I35 and solids resides on the fact that in I35 all components of the anisotropic interactions perpendicular to the director axis are averaged away by the fast anisotropic rotation of the single molecule, (this assumption derives from the comparison of the correlation times of the molecular motions with the NMR time scale). As a consequence, the motionally-averaged anisotropic interactions share a common principal axis system defined by the director axis, and so they have the same time dependence when subject to macroscopic rotation. By definition such a Hamiltonian commutes with itself at all times and so is "inhomogeneous" in the sense defined by Maricq and Waugh [9]. For the inhomogeneous system the spectra readily break up into sharp spinning sidebands and even slow spinning can lead to considerable line narrowing.

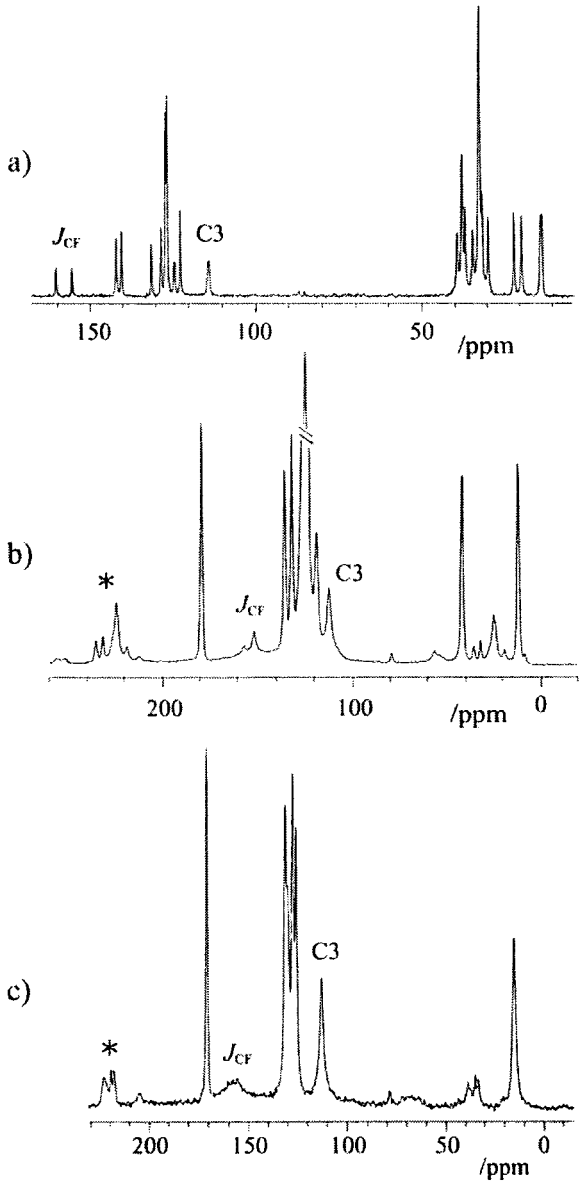

Figure 5.15 Comparison of CP/ MAS ^{13}C spectra in three different compounds, using ^{1}H TPPM decoupling. On the top, (a) I35 in the nematic phase, on the middle Flurbiprofen and at the bottom 3-fluoro-4-methyl-benzoic acid. In all three cases we used the same ^{1}H decoupling setup, e.g., decoupling power 50 kHz, and for the TPPM parameters, tip angle β , 180° with phase angle of 14°. For I35 spinning speed was 2.8 kHz, while for the other two samples 5 kHz. Since those samples contain the same mono-fluorinated biphenyl fragment the only difference resides on F—F and F—H intermolecular dipolar interactions.

In "real" solids, however, the anisotropic interactions do not share a principal axis systems and the overall Hamiltonian does not commute with itself at different times. In this case we say that system behaves "homogenously". Spinning these systems usually lead to spectra with spinning sidebands that have distinct width and significant line narrowing can be achieved only if the rotation speed is much greater than size of spin Hamiltonian.

As a result in the limit of efficient ^{1}H decoupling in order to obtain negligible effects from F—F and C—F dipolar interactions is necessary to use high spinning speeds. As previously remarked, however, the experiment on Flurbiprofen shows that using TPPM decoupling with a spin rate of 15 kHz the overall resolution of the J_{CF} doublet is degraded in comparison with the observation at spinning speed of 5 kHz (see Figure 5.13). One possible explanation of these observations is that of interference between the two averaging processes, the magic angle spinning and ^{1}H decoupling. One of the most important interference effect between mechanical rotation and decoupling field is the rotary-resonance recoupling [32-34], which leads to a broadening of the spinning sideband spectrum by means of recoupling of the dipolar coupling and chemical-shielding tensors. Although very fast spinning speed combined with an efficient ^{1}H-decoupling [35] it is not an easy task, a new sequence (acronym, XiX, [36, 37]), has been developed by M. Ernst which seems to be more efficient with respect to TPPM scheme.

Due to the ^{1}H decoupling, the ^{1}H spin bath should not be the predominant factor in limiting the resolution of J_{CF} splitting. This is consistent with the experimental observation, as seen in the ^{13}C spectra of Flurbiprofen (Figure 5.16); varying the ^{1}H decoupling offset does not significantly affect the J_{CF} doublet. Conversely the protonated carbons are quite sensitive as the ^{1}H offset varies; scaling the corresponding carbon linewidth about a factor of two over J_{CF} peaks. Moreover increasing the ^{1}H decoupling power from 50 kHz to ~ 60 kHz, the ^{13}C linewidth of J_{CF} splitting does not reveal substantially differences.

Similar behaviour is found in 3-fluoro-4-methyl-benzoic acid, where the J_{CF} remains severely broadened irrespective of any variation of ^{1}H proton decoupling parameters.

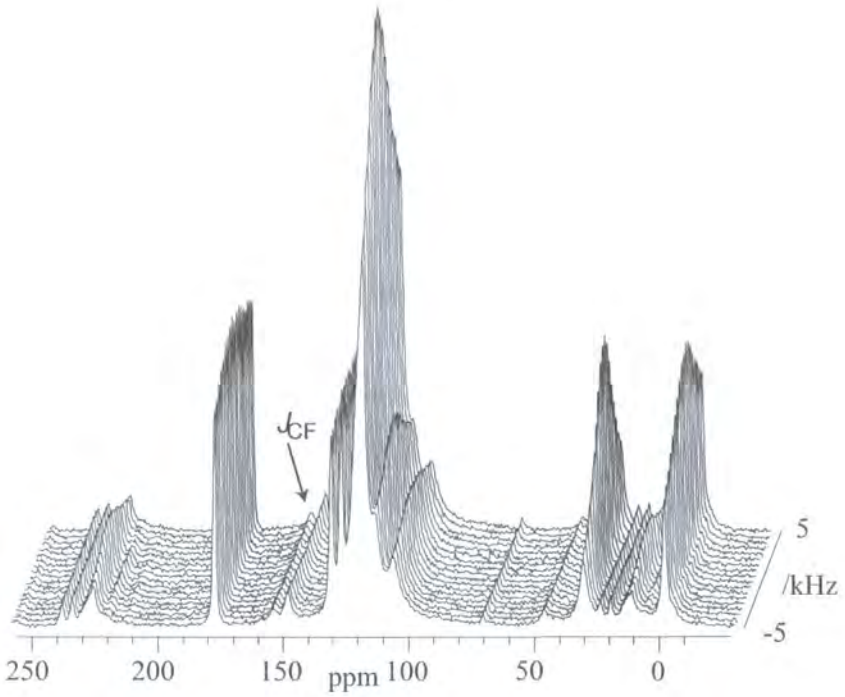

Figure 5.16 ^{13}C spectra of Flurbiprofen varying ^{1}H offset within the range of ± 5 kHz. The decoupling scheme used was TPPM with a tip angle β of 180° and phase angle ϕ 14°, while the decoupling power was 50 kHz. The experimental parameters were: contact time 3ms, recycle delay 10 s and spinning speed ~ 5 kHz. As seen in the Figure the J_{CF} splitting remains substantially unaffected as ^{1}H offset varies against the relevant variation for the protonated carbons.

As a result in this context we need to investigate the effects of finite lifetime of ^{19}F on the ^{13}C spectrum. The nature of spin state lifetime in solids is dominated by coherent effects ("spin diffusion" due to multiple dipolar coupling), rather than truly incoherent relaxation. However with a good approximation we can describe the spin diffusion mechanism as a stochastic process by using an exchange model. This model is an alternative fashion to avoid unmanageable calculation using density matrix treatment for very large spin system. However, using this method we can easily estimate the maximum broadening on J_{CF} splitting generated by the exchange process. To do this we need to involve Liouville space [38] considering the superoperator:

$$\hat{L} = i[H,] + \hat{\Gamma} \tag{5.13}$$

The Hamiltonian H in Eq. .(5.13) represents two spins C—F scalar interaction, while $\hat{\Gamma}$ is the relaxation operator. The form of $\hat{\Gamma}$ for the exchange model is given by:

$$\hat{\Gamma} = k\left(\left[I_x^F,\left[I_x^F,\right]\right]+\left[I_y^F,\left[I_y^F,\right]\right]+\left[I_z^F,\left[I_z^F,\right]\right]\right) \tag{5.14}$$

The factor k, in frequency unit, establishes the efficiency of spin diffusion in the ^{19}F spin bath. From solution state experiments we found for Flurbiprofen a J_{CF} coupling of ~250 Hz. Using this value we performed the simulation varying the strength of spin diffusion rate k. In the Figure 5.17 are shown the simulation results with the maximum contribution to the line broadening around 250 Hz at a spin diffusion rate k of 570 Hz.

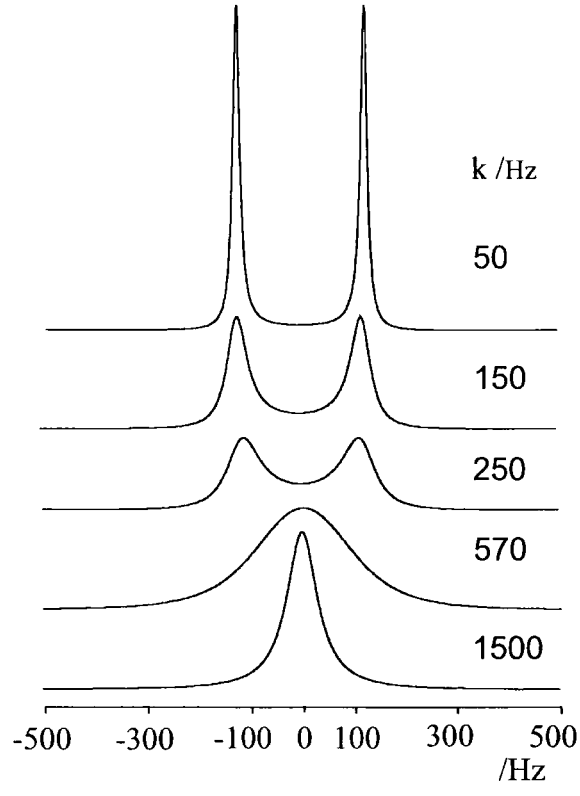

Figure 5.17 Simulation of line broadening effects on J_{CF} splitting from spin diffusion in the ^{19}F spin bath. The simulation was performed for a *S-I* spin system, where the *I*-spin is coupled via dipolar

interactions to the *I*-spin bath. The spin diffusion model was based on an exchange type process. The spectra were simulated varying the parameter *k*, which represents the spin diffusion rate.

These results are consistent with experimental observation on Flurbiprofen. We found that the minimum linewidth of the individual components of the C—F doublet was about 100 Hz, which is much less than the broadening (~ 250 Hz) achievable from spin diffusion with a J_{CF} coupling of 250 Hz. This is consistent with the fact that the J_{CF} doublet is observable with the separation of the peaks as in the liquid case.

On the other hand, as seen in the simulation of Figure 5.17, when the diffusion process becomes more active the distance between the peaks decreases significantly. The simulation shows that at a linewidth of 100 Hz the J_{CF} splitting results reduced of the 25%, against the full splitting experimentally observed.

This suggests that the observed linewidth is limited by the "inhomogeneous " broadening rather than the finite lifetimes of ^{19}F spin state.

By contrast in 3-fluoro-4-methyl-benzoic acid the J_{CF} splitting lumps into single broad peaks whose linewidth is around ~330 Hz with the same J_{CF} coupling constant of Flurbiprofen (~250 Hz). Unlike Flurbiprofen, in this case the amount of the broadening of J_{CF} doublet could be consistent with the maximum broadening introduced by ^{19}F spin diffusion process. On the other hand the efficiency of spin diffusion is related not only to the strength of dipolar interactions but also it depends on the density of the spin bath. As a result the molecular packing can be an important parameter in determining an efficient spin diffusion process. In Figure 5.18 is illustrated an expansion of the local structure of Flurbiprofen, (a), and 3-fluoro-4-methyl-benzoic acid. The relevant difference between those two structures resides on the different distributions of ^{19}F network interactions. In Flurbiprofen the relevant effects from F—F interactions are restricted only to ^{19}F spin pair in proximity of the C2 site. The corresponding ^{19}F spin bath can be regarded as a repetition of quite isolated ^{19}F spin pairs. This, probably, explains why the local ^{19}F environment is less effective in degrading of the C2 resonances.

As for the 3-fluoro-4-methyl-benzoic-acid, the ^{19}F bonded to the carbon C2 is interacting with a long linear array of ^{19}F nuclei coupled to each other with same dipolar coupling constant. This ^{19}F nuclei distribution around the C2 site certainly aids the "spin diffusion" mechanism causing a considerable reduction of ^{19}F Zeeman state lifetime.

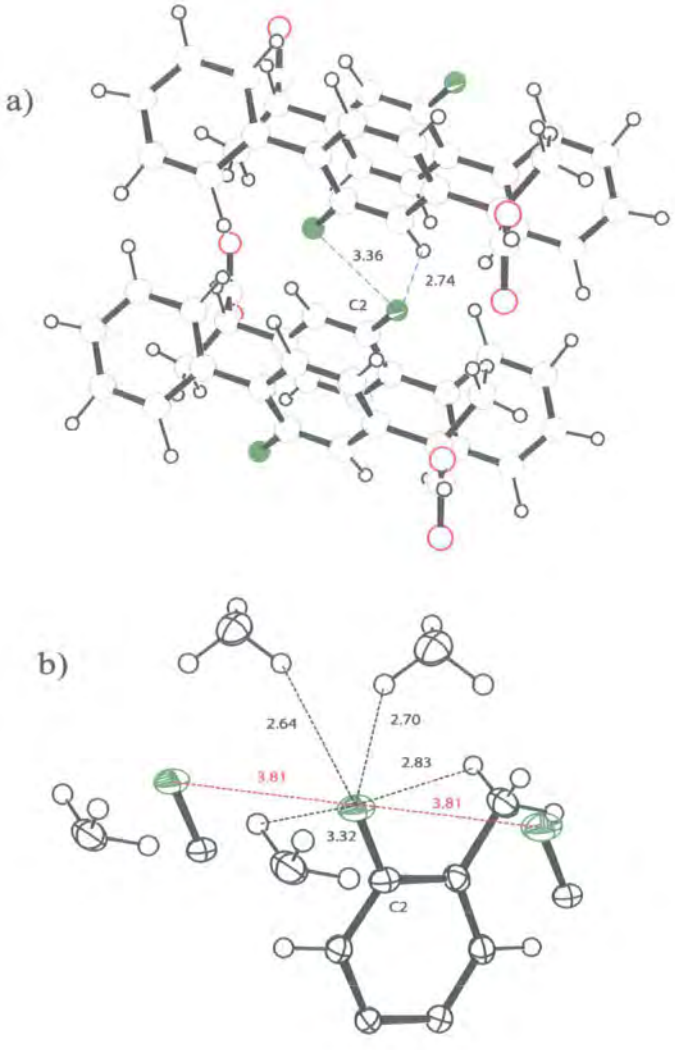

Figure 5.18 Expansion of two crystal structures: a) Flurbiprofen, b) 3-fluoro-4-methyl-benzoic acid. The numbers reported in figure are the internuclear distance in Ångströms. The dipolar couplings constants around the C2 carbon are comparable in both cases, while the distribution of ^{19}F nuclei is different. In Flurbiprofen the relevant F—F interactions can be approximated to a spin pair, which is

not the case for the 3-fluoro-4-methyl-benzoic acid where the ^{19}F's are equally spaced forming linear arrays.

5.6 Fluorine T_2 measurement and discussion

5.6.1 Hahn echo experiment

The schematic representation of Hahn echo experiment is given in Figure 5.19. This experiment consists of a $(\pi/2)_x$ pulse to create an observable magnetisation in the *x*-*y* plane, and a $(\pi)_y$ pulse applied at time $\Delta t_1/2$ after the excitation pulse, to refocus the NMR signal at Δt_1.

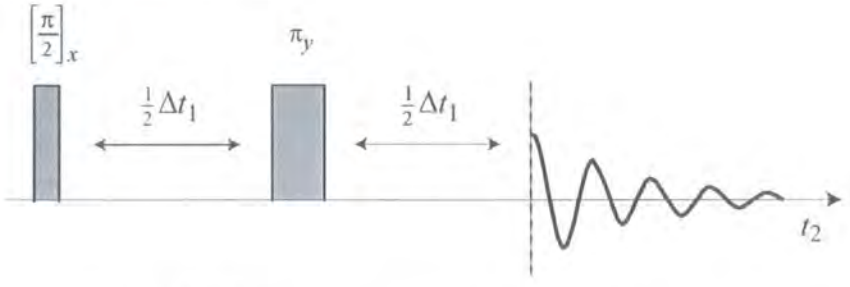

Figure 5.19 Schematic representation of Hahn echo sequence.

The $(\pi)_y$ pulse should refocus the linear interactions, such as dc-field inhomogeneities, chemical shift and the heteronuclear dipolar interactions.

So that, the coherences create in the *x*-*y* plane of the rotating frame dephase under these interactions at echo time. It is important to note that the rate of this dephasing is determined by two different mechanisms: coherent and incoherent process. The coherent process is generated by multibody interactions, such as dipolar couplings among abundant spins (dipolar dephasing). Since well-defined Hamiltonian governs this contribution to the signal decay, using an appropriate multiple-pulse sequence can eliminate it. By contrast, we cannot eliminate the incoherent contribution to the dephasing using pulse sequences, since this results from stochastic fluctuations of local fields.

After these clarifications we can say that the Hahn echo experiment provides a measurement of T_2 that involves both coherent and incoherent dephasing processes.

5.6.2 T_2 experiments

In order to understanding more about the physical origin of the ^{13}C linewidth due to the intermolecular effects, the ^{19}F T_2 has been measured. To increase significantly this relaxation time T_2, one needs to reduce as much as possible, the F—F (homonuclear decoupling) interactions and F—H as well (heteronuclear decoupling). The achievement of a consistent scaling factor of these interactions we need to combine the maximum efficiency of the two averaging process available: The magic angle spinning and double $^{19}F\&^{1}H$-irradiations. Unfortunately, in many cases both of these techniques suffer of some physical limit.

As mentioned in the previous section instance, to eradicate the strong homonuclear interactions by using the magic angle spinning is often quite difficult, even with relative fast spinning speeds. On the other hand in conventional double decoupling experiments quite often a large amount of RF-power must be employed with a consequent stress of the resonant circuit, or even heating the sample. In both cases, we can overcome, of some extent, those two technical problems, reducing the volume of the coil and the rotor. We need to realize that in this situation the reduced amount the sample drastically degrades the sensitivity making hard to observe rare nuclei, like ^{13}C as in our case. Summarizing, if the very well resolved J_{CF} splinting is related to a very long T_2 on ^{19}F space, in many circumstances, it will be very difficult to achieve, especially in large high-fluorinated molecules. Surprisingly, even in small mono-fluorinate molecules such as, Flurbiprofen the ^{19}F T_2 is quite short. Figure 5.20 shows the fluorine T_2 measurement on Flurbiprofen using Hahn echo experiment. By fitting the data with a single exponential, the value of T_2 is around 630 μs. The length of this T_2 is quite reduced, considering that the spinning speed used was of 15 kHz and that the strength of F—F and F—H dipolar coupling were not very large, about 3 kHz, and 5 kHz respectively. Moreover a π pulse of 5.5 μs refocused effects from the heteronuclear dephasing. Nevertheless, the J_{CF}

splitting with proton decoupling and under the above MAS condition is observable, even thought the carbon linewidth of the doublet is still poor. It is remarkable that, also at low spinning speed, 5 kHz, this splitting appears and shorter ^{19}F T_2 is expected because F—F are less averaged by MAS.

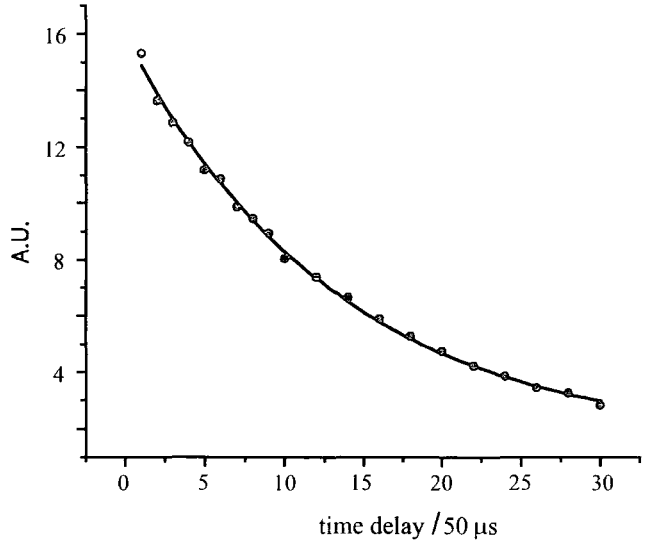

Figure 5.20 Fluorine T_2 relaxation time measurements of Flurbiprofen molecule using the Hahn echo sequence. Fitting the data with a single exponential the T_2 is $630 \pm 30 \mu s$. The spinning speed was 15 kHz and the π -pulse duration, 5.5 μs.

From the experiments of I35 in the nematic phase and solid, (Figure 5.11), is seen that in the former case (nematic) a sharp doublet is observed and no F—F couplings are present, whereas in the latter case (solid) where the F—F are recovered the doublet is quite broad. This shows the effects of the F—F interactions and consequently that the ^{19}F T_2 parameters plays an important role in resolving the J_{CF} splitting, but its value it does not provide a direct criteria to establish how well the interactions will be resolved, the challenge is to understand which part of T_2 mechanism indeed, determines the lifetime of ^{19}F states.

From simple considerations of the Fourier theory is known that any phenomenon of duration τ is represented by a Fourier frequency distribution of a width not less than

$\delta\nu \simeq 1/2\pi\tau$. If we apply this result directly to the uncertainty relation, $\Delta E\Delta t \geq \hbar$, we obtain that:

$$\delta\nu\Delta t \geq \frac{1}{2\pi} \tag{5.15}$$

In NMR this means that an interaction, in order to produce two resonances separated by a frequency $\Delta\nu$, must have duration τ large in comparison with, $1/2\pi\Delta\nu$.

By doing a simple calculation, and assuming the ^{19}F T_2 as the duration of the J_{CF} interaction we find out that we can not distinguish two peaks separated by a frequency of 250 Hz, as shown on the Flurbiprofen ^{13}C spectrum (Figure 5.10). This fact says that we need to take care when we are speaking about the physical meaning of T_2, in other word we cannot take the T_2 value, directly, as lifetime of α or β ^{19}F states. In the end, the T_2 measurement on LC's I35, under MAS, gives a value T_2 of 41 ± 1 ms that widely satisfies the condition $T_2 \gg 1/2\pi\Delta\nu$ with a J_{CF} of 250 Hz. This experimental result agrees with the resolutions observed on the MAS ^{13}C spectra of I35 in the nematic phase, but in that case T_2 doesn't contain the effects form F—F interactions because of molecular tumbling.

5.7 Double decoupling experiment

In order to achieve equally distributed carbon resolution across the spectrum we performed the double decoupling experiment irradiating both ^{19}F and ^{1}H. The sequence used is drawn in Figure 5.21:

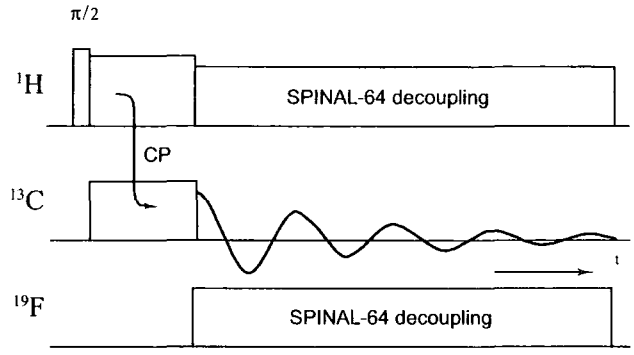

Figure 5.21 Schematic representation of triple channels experiment. The initial ^{13}C magnetisation is obtained by cross-polarisation (CP). The NMR carbon signal evolves under ^{19}F and ^{1}H decoupling according to the SPINAL-64 scheme.

In double decoupling experiment a particular care must be taken about the amount of the power on both channels in order to avoid the CP-MAS condition between the decoupled nuclei. Cross polarising these nuclei during the acquisition time strongly reduces the over all decoupling efficiency giving rise a severe increasing of carbon linewidth. In our experiments, in order to obtain a mismatch in the CP condition, the amount the power employed on ^{1}H and ^{19}F, were 5 μs and 6 μs respectively. Nevertheless it is worth to note that by using SPINAL scheme reduces the possibility, over continuous wave decoupling, to lock the residual ^{1}H-magnetisation after the CP period. This is due to the multi-phase modulation of RF-field which gives rise to a very complicated trajectory of the proton magnetisation. Obviously despite this complicate motion it is not excluded that a small fraction of the magnetisation could be locked. The Figure 5.22 shows the experimental observations of Flurbiprofen and 3-fluoro-4-methyl-benzoic acid using double SPINAL-64 decoupling. Even with double decoupling the C2 linewidth, on Flurbiprofen, is better resolved than the corresponding and C3 resonance in the other molecule, resulting 15 Hz narrower. By using double CW decoupling the resolution is reduced of a factor around 10%, however the doubly decoupled ^{13}C spectra exhibit well-resolved peaks with respected to the singly decoupled peaks, in particular it produces sharp resonances for those carbons bonded to ^{1}H and in proximity to the ^{19}F site, (A-B peaks in the Figure 5.22).

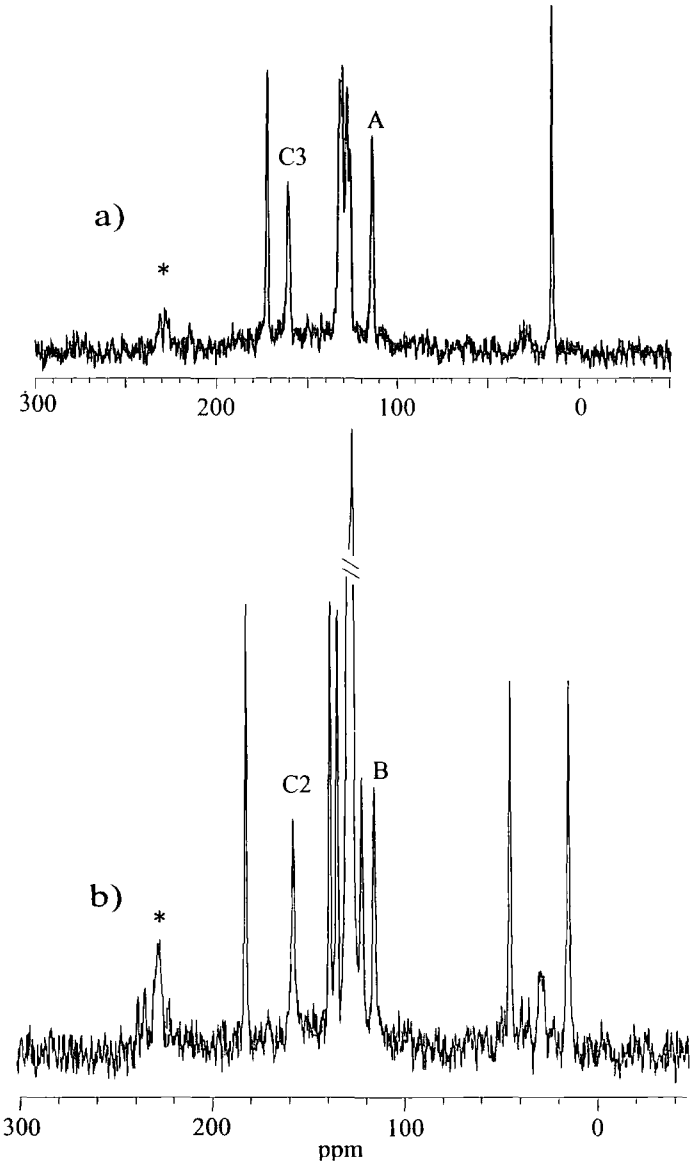

Figure 5.22 ^{13}C-spectra of two molecules: 3-fluoro-4-methyl-benzoic acid a) Flurbiprofen b). Both ^{1}H and ^{19}F spins are decoupled using SPINAL-64 decoupling with a tip angle of 170°. C2 and C3 peaks belong to the carbons bonded to ^{19}F, while A-B peaks are resonances of the carbons bonded to ^{1}H and in proximity to the ^{19}F site. The decoupling power, 5 μs on ^{1}H while 6 μs on ^{19}F. The contact time, 3ms, recycle time, 10 s, a), 30s, b), the spinning speed was 5 kHz.

This shows that indeed the linewidth of protonated carbons is strongly affected by their proximity to ^{19}F site. As experimentally proved, the double decoupling gives better performance over the single one at expense of a more informative spectrum

obtained preserving the C—F couplings, and also, not less important, the more demanding from the experimental point of view requiring a dedicated equipment and special probe design. At the moment the single ^{1}H-decoupling appears uncompetitive with respect to the case where also the fluorine interactions are removed. The highest resolution on ^{13}C bonded to the ^{19}F nucleus achieved with ^{1}H TPPM is around 100 Hz against the 60-70 Hz obtained with triple channels experiments. Moreover we need take into account that the resolution of 100 Hz has been obtained in a particular mono-fluorinated compound, such as Flurbiprofen, where the overall effects owing to intermolecular F—F is approximately limited to a ^{19}F spin pair. The TPPM sequence, as many times was pointed out in our discussions, results dramatic ineffective in a sample like 3-fluoro-4-methyl-benzoic acid. The challenging is to find out ^{1}H-decoupling sequence capable to work in very fast spinning regime. As previously mentioned M. Ernst's sequence, XiX, [36, 37] could be a good candidate to give a considerable improvement in reducing line broadening in samples, such as 3-fluoro-4-methyl-benzoic acid. The requirement of the fast mechanical rotation is deeply connected with the homogeneous character ^{19}F Hamiltonian and with the fact that we want to resolve weak interactions such as J_{CF}-couplings in organic compounds.

The experiments were performed on a Chemagnetics CMX spectrometer operating at a proton Lamor frequency of 200.13 MHz, using a standard triple-resonance MAS probe HFX with a coil of 7.5 mm. Due the large volume of the coil the Q-factor of the resonant circuit results quite small (~100), for which a large amount of RF-power is necessary even with soft pulse excitation. As a consequence in order to achieve an effective double decoupling particular care was taken at tuning time. Moreover in order to avoid interference effects between ^{1}H and ^{19}F channels the trap circuit was tuned in high power obtaining isolation around –25dB. The inhomogeneous ^{13}C linewidth was measured on adamantine resulting around 5Hz.

5.8 Conclusion

Under MAS, as in static case, we have observed that the H—F dipolar interactions effectively govern the broadening mechanism for those ^{13}C's close to the ^{19}F site. As a result the ability to resolve, and hence to quantify C—F interactions depends critically on the efficiency of heteronuclear decoupling.

Through the simulations we proved that the H—F dipolar tensor behaves as an effective ^{1}H CSA tensor according to ^{19}F states. Unlike the static case, now the effects of H—F interactions cannot be seen as simple shift from the on-resonance condition of the α/β ^{13}C resonances. First order average Hamiltonian theory provides an explanation in terms of second order recoupling between an effective ^{1}H-CSA tensor due to the H—F and C—H dipolar. Using TPPM or SPINAL rather than CW decoupling largely remove these effects.

We found that misset of the magic angle results in asymmetric broadenings of the doublets component, which degrades and compromise the quantification of the J_{CF} interactions.

Nevertheless, unlike LC's, in solids the resolution of J couplings is not usually limited by decoupling efficiency, but by the residual broadening from lifetime of ^{19}F spin state. At the moment double decoupling appears the only way to restore good resolution across the entire spectral width.

References

1. A. Abragam: Principles of Nuclear Magnetism, *Oxford University Press* (1961), pp.530-533.
2. K. Takegoshi, J. Mizokami, T. Terao, *Chem. Phys. Lett.* **341**, 540-544 (2001).
3. Y. Yu, B. M. Fung, *J. Mag. Res.* **130**, 317-320 (1998).
4. B. M. Fung, A. K. Khitrin, K. Ermolaev, *J. Mag. Res.* **143**, 97-101 (2000).
5. J. Courtieu, J. P. Bayle, B. M. Fung, *Progress in NMR Spectroscopy* **26**, 141-169 (1994).
6. J. W. Emsley: Nuclear Magnetic Resonance of Liquid Crystals, *NATO ASI Series* (1987).
7. G. Antonioli, D. E. McMillan, P. Hodgkinson, *Chem. Phys. Lett.* **344**, 68-74 (2001).
8. M. Mehring: Principles of High Resolution NMR in Solids, *Springer-Verlag, Berlin* (1983), pp. 40-50.
9. M. M. Mariq, J. S. Waugh, *J. Chem. Phys.* **70**, 3300-3316 (1979).
10. D. Sakellariou, A. Lesage, P. Hodgkinson, L. Emsley, *Chem. Phys. Lett.* **319**, 253-260 (2000).
11. E. Vinogradov, P. K. Madhu, S. Vega, *Chem. Phys. Lett.* **314**, 430-450 (1999).
12. Z. Gan, R. R. Ernst, *Solid State Nuclear Mag Res* **8**, 153-159 (1997).
13. I. J. Lowe, *Phys. Rev. Lett.* **2 (7)**, 285-287 (1959).
14. M. Mehring, G. Sinning, *Phys. Rev. B* **15 (5)**, 2519-2532 (1977).
15. P. R. Levstein, G. Usaj, H. M. Pastawski, *J. Chem. Phys.* **113 (15)**, 6285-6287 (2000).
16. U. Haeberlen: High resolution NMR in solids: selective averaging, *Accademic Press, New york* (1976).
17. E. Ciampi *et al.*, *Liquid Crystals* **26**, 109-125 (1999).
18. U. Haeberlen, J. S. Waugh, *Phys Rev* **175**, 453 (1968).
19. W. Magnus, *Comm Pure Math* **7**, 649 (1954).
20. C. P. Slichter: Principles of Magnetic Resonance, *Springer-Verlag Berlin Heidelberg New York*, (1989), pp. 623-628.

21. E. Wab, *Ann Phys* **48**, 72 (1968).

22. M. Ernst, S. Bush, A. C. Kolbert, A. Pines, *J. Chem. Phys.* **105(9)**, 3387-3397 (1996).

23. M. Ernst, A. C. Kolbert, K. Schmtdh-Rohr, A. Pines, *J. Chem. Phys.* **104(21)**, 8258-8268 (1996).

24. M. E. Rose: Elementary of angular Momentum, *Wiley, New York* (1995), Chapter 5.

25. E. W. Hagaman, *J. Mag. Res.* **104**, 125-131 (1993).

26. S. A. Smith, W. E. Palke, J. T. Gerig, *J. Mag. Res.* **106**, 57-64 (1994).

27. Z. Luz, R. Poupko, S. Alexander, *J. Chem. Phys.* **99 (10)**, 7544-7553 (1993).

28. C. Filip, X. Filip, D. E.Demco, S. Hafner, *Molecular Physics* **92**, 757-771 (1997).

29. O. N. Antzutkin, *Progress in NMR Spectroscopy* **35**, 203-266 (1999).

30. R. K. Harris, K. J. Packer, A. M. Thayer, *J. Mag. Res.* **62**, 284-297 (1985).

31. R. Teeaar, M. Alla, E. Lippmaa, *Org. Magn. Reson.* **19(3)**, 134-137 (1982).

32. K. Takegoshi, K. Nomura, T. Terao, *Chem. Phys. Lett.* **232**, 424-428 (1995).

33. T. G. Oas, R. G. Griffin, M. H. Levitt, *J. Chem. Phys.* **89(2)**, 692-695 (1988).

34. M. Edén, Y. K. Lee, M. H. Levitt, *J. Mag. Res.* **120**, 56-71 (1996).

35. M. Ernst, A. Samoson, B. H. Meier, *Chem. Phys. Lett.* **348**, 293-302 (2001).

36. M. Ernst, *J. Magn. Res.* **162**, 1-34 (2003).

37. A. Detken, E. H. Hardy, M. Ernst, B. H. Meier, *Chem. Phys. Lett.* **356**, 298-304 (2002).

38. R. R. Ernest, G. Bodenhausen, A. Wokaun: Principles of Nuclear Magnetic Resonance in one and two dimensions, *Oxford University Press, London* (1987), pp. 19-24.

Chapter 6

Separated Local Field and off-resonance decoupling

6.1 Introduction

In Chapter 4 we have demonstrated that SPINAL decoupling provides good resolution over the entire ^{13}C bandwidth. This permits more accurate quantification of C—F dipolar couplings from 1D-spectra. On the other hand before this data can be used the assignment of the C—F splittings is required.

In contrast with ordinary liquid crystals, the ^{1}H-decoupled ^{13}C spectra of fluorinated liquid crystals is more complex since the C—F dipolar coupling causes each ^{13}C peak to split into doublet. Nevertheless pervious work on I35 sample, Ciampi *at al*, [1] have shown that using ^{1}H-decoupled ^{13}C spectra with Variable-Angle-Sample-Spinning (VASS) [2] it is possible to assign all the C—F splittings. The advantage of this method is that large dipolar interactions are scaled, resulting in a better performance of decoupling sequences. The drawbacks of this procedure are that the smaller long-range dipolar couplings are not detectable and specialized equipment is required. In order to substitute the VASS method, using conventional probes, we tried to setup a triple channel experiment in which the ^{13}C is observed and ^{1}H's are fully decoupled, while the fluorine nucleus is irradiated in a wide range of off-resonance frequencies. In principle the off-resonances irradiation should be equivalent to the VASS method in scaling the dipolar interactions. In the off-resonance irradiation the averaging process of the interactions occurs in the spin space instead of the real space as in the VASS case. In the first part of this chapter we shall show the experimental

results of off-resonance experiment. As we shall see, due to the strong overlapping of the peaks makes impossible to use these results to assign the C—F splittings.

In order to simplify the complex 1D spectra we tried to design a 2D procedure, which is called *Separated-Local-Field* (SLF). This experiment should reduce the peak overlapping since the C—F dipolar splittings and chemical shifts are separated in two different frequency axes. Once we have complete assignment of ^{13}C resonances for a fully ^{1}H and ^{19}F decoupled spectrum, it should be possible to assign the C—F splittings by using SLF spectra.

6.2 ^{19}F off-resonance decoupling experiment on I35 LC

As mentioned above, we are exploring different NMR methods for studying liquid crystals containing ^{19}F. By exploiting the fluorine atom as a probe nucleus we can hope to determine the order parameter and molecular conformation from a set of C—F interactions. Before this data can be used, however, the assignment of C—F splittings is required. We started with a simple experiment that involves ^{19}F off-resonance decoupling as method of assignment.

These experiments were performed with a HFX triple channel probe using a CMX spectrometer operating at the proton Larmor frequency of 200.13 MHz and 188.288 MHz for fluorine nucleus. A 7.5 mm rotor was filled with I35, and the temperature of the sample was set at 40°C (stabilized within the range of ±0.1°C), corresponding to the nematic mesophase.

The setup of HFX probe needs to be done carefully since this probe has a resonant circuit with a low Q-factor (Q<100) [3] and so a large amount of RF power is required for a given 90° pulse length. Moreover a lower Q-factor also gives a weaker NMR signal, with a corresponding reduction of the signal to noise ratio. Particular care was taken in tuning the individual channel of the probe, since even a slight misadjusting of resonant circuit can lead to an employment of extra RF power, which

would result in excessive heating of the sample and damage of the resonant circuit itself. As the Larmor frequencies of ^{1}H and ^{19}F nuclei are very close, the isolation of the corresponding ^{1}H and ^{19}F channels is crucial for the success of the experiment. In order to avoid interference between the ^{1}H and ^{19}F channels during simultaneous irradiation, the trap circuit was carefully tuned, obtaining an isolation of the ^{1}H and ^{19}F channels of about –26 dB.

In our experiment we used ~200 watts (corresponding to a 5 μs 90° pulse) for the ^{1}H decoupling, while for the ^{19}F decoupling we used ~180 W (5.5 μs). Given this high RF power deposited into the probe, it was important to reduce the acquisition time as much as possible. The achievable carbon resolution depends upon the appropriate combination of the decoupling power and acquisition time. Moreover the duty cycle must be long enough to limit RF heating effects. The ^{13}C spectra have been obtained implementing the sequence represented in Figure 6.1:

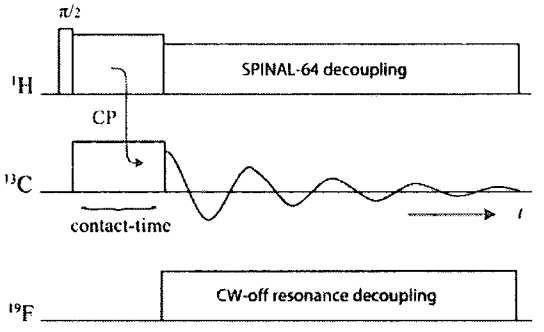

Figure 6.1 Schematic representation of a triple channels sequence used for the off-resonance decoupling experiment. After the cross polarisation from ^{1}H, the ^{13}C signal evolves under double decoupling: SPINAL-64 for ^{1}H and off-resonance CW for ^{19}F.

The experiment is very simple in principle; it consists of ^{1}H-decoupled ^{13}C spectra, while the C—F dipolar interactions are scaled by the off-resonance irradiation of the ^{19}F. The SPINAL-64 ^{1}H-decoupling was optimised in a separate experiment, recording the ^{13}C spectra without ^{19}F decoupling. The best performance was found adjusting the ^{1}H-transmitter position, of about 0.6 kHz from the zero ^{1}H offset, and

the optimum tip angle β of the ^{1}H magnetisation was about 170°. With these optimisations, the ^{13}C linewidths were in the range of 10-20 Hz for all the peaks. The off-resonance ^{19}F decoupling was accomplished using continuous wave irradiation (CW). Since the I35 contains only a ^{19}F atom in the molecule, no particularly sophisticated decoupling is needed to scale the C—F interactions.

As we have seen in Chapter 1 off-resonance decoupling results in a non-zero scaling factor χ of dipolar interactions. Under condition of strong decoupling fields this scaling factor χ is given by:

$$\chi = \left| \frac{\Omega_F}{\gamma_F B_{eff}} \right| \tag{6.1}$$

Where $\Omega_F = |\omega_2 - \omega_F|$ is the ^{19}F-offset and $B_{eff} = \sqrt{\Omega_F^2 + B_2^2}$. From Eq.(6.1), it is straightforward to see that by varying the frequency ω_2 of the decoupling field we can change the size of the scaling factor χ, consequently a simple correlation between the ^{13}C spectra and ^{19}F off-resonance irradiation can be established. This is shown in simulation of Figure 6.2.

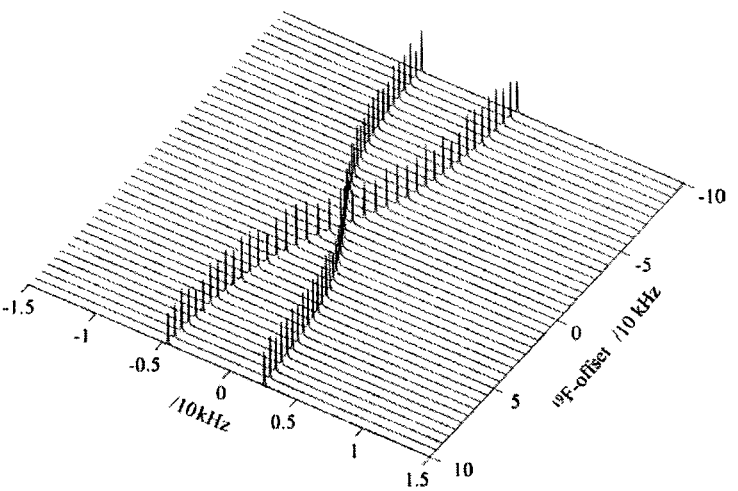

Figure 6.2 Simulation of ^{13}C splittings in a C—F spin system as a function of ^{19}F offset with CW decoupling.

Figure 6.3 shows the series of fully ^{1}H-decoupled ^{13}C spectra recorded as a function of the ^{19}F-offset.

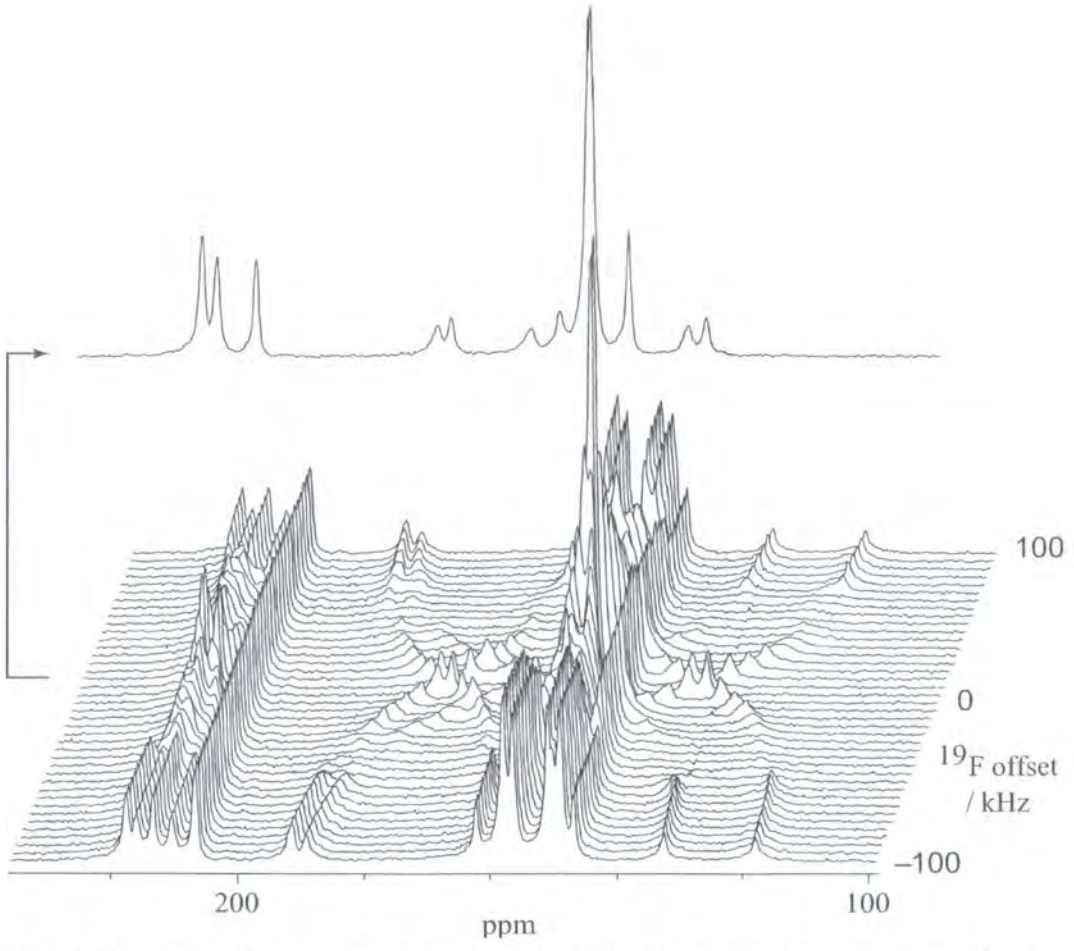

Figure 6.3 ^{13}C spectra of I35 in the nematic phase at 40° C. The spectra have been obtained with double decoupling using SPINAL-64 and CW respectively for ^{1}H and ^{19}F nuclei. The ^{1}H decoupling averages out the C—H interactions, while the C—F interactions are scaled by an off-resonance irradiation that varies within the range of offsets -100 kHz...100 kHz in steps of 5 kHz. This variable scaling of the C-F doublets is seen clearly for the larger C—F splittings, but is obscured by the strong overlap from the smaller splittings. At the top is shown a ^{13}C spectrum with zero ^{19}F-offset. This differs from the isotropic solution-state spectrum only by shifts of the peak positions due to the ^{13}C-CSA. Experimental parameters: CP contact time of 3 ms, 5 μs of spin-lock power, acquisition time, 81 ms, recycle delay, 7s, transient number, 2048, ^{1}H and ^{19}F decoupling power, 5.5 μs, 5 μs respectively.

6.2.1 Discussion

In principle the off-resonance decoupling could be a quite good method to assign the carbon atoms to the related C—F doublets. In fact once we have the complete assignment of the fully decoupled spectra, where the peak positions are determined only by the ^{13}C chemical shift, we can easily establish which C—F splitting corresponds to which carbon atom in the molecule. Indeed, in the same circumstances, in small molecules, off-resonance decoupling has been applied successfully [4]. Unfortunately it is not the case here due to the strong overlap of the peaks.

By varying the off-resonance frequencies in a wide range (-100 +100 kHz, step 5 kHz), we obtained a large modulation of the single C—F splitting. The experimental observations generally fit in well with the theory of off-resonance decoupling. But for particular ranges of ^{19}F offset, large broadenings of the scaled C—F splitting are observed. Full simulation of the C—H—F system as shown in Figure 6.4 successfully reproduces the experimental results. As seen in the simulations of Figure 6.4 the C—H interaction has no effects in broadening the components of the scaled C—F splitting. The observed C—F broadening is only restricted to the effects from ^{1}H and ^{19}F RF-fields and H—F dipolar interaction. However, unlike ^{19}F CW decoupling, the time dependence of C—H—F Hamiltonian from ^{1}H-decoupling (SPINAL-64,[5]) cannot be removed by any transformation into ^{1}H rotating frame [6, 7], so that a quantum mechanical analysis of these effects becomes very complicate and so no further investigation have been done on this problem.

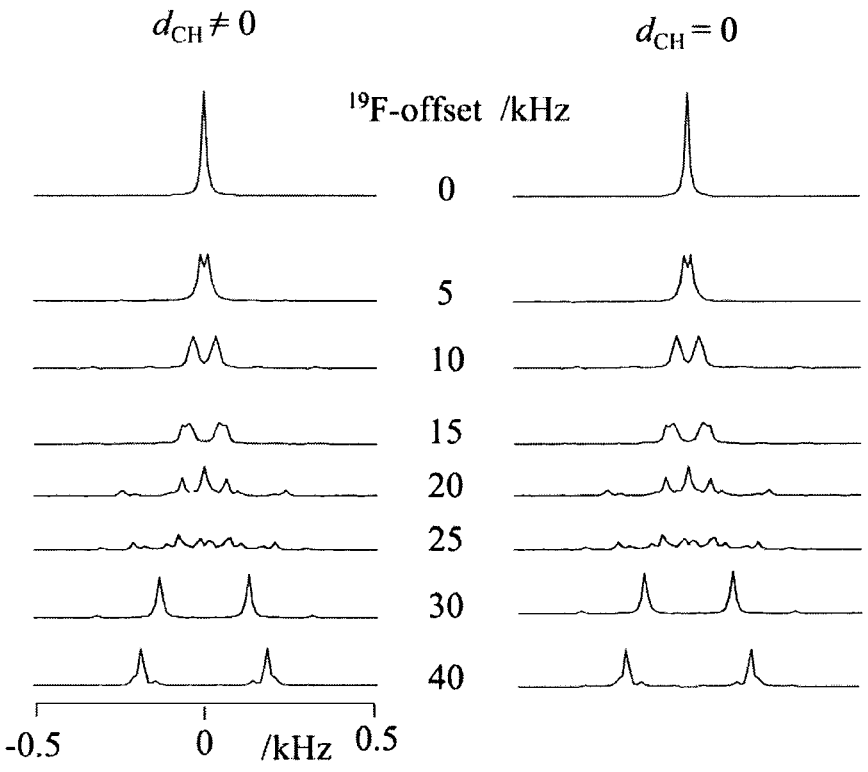

Figure 6.4 Simulations of ^{1}H-decoupled ^{13}C spectra as a function of ^{19}F off-resonance decoupling in a C—F—H spin system. The SPINAL-64 was employed for the ^{1}H-decoupling with a tip angle of 170°, and CW for the ^{19}F decoupling with a set of offset values as reported in Figure. Left: ^{13}C spectra with non-zero C—H dipolar coupling. Right: ^{13}C spectra with zero C—H dipolar coupling.

Since off-resonance decoupling has not proved to be very useful in obtaining the C—F assignments of I35, we tried to apply the Separated-Local-Field technique in order to overcome the peak-overlapping problem.

6.3 The Separated Local Field technique

6.3.1 Introduction

The application of off-resonance decoupling to I35 turns out to be strongly limited by peak overlap. As an alternative, a two-dimensional "Separated Local Field" (SLF)

experiment has been applied [8-12]. The SLF experiment enables the separation of the *IS*-heteronuclear interactions from the *S*-spin chemical shifts. This separation can be accomplished following the scheme represented in Figure 6.5.

After the *S*-signal has been prepared (preparation sequence block), the *S*-signal evolves in t_1-dimension under the heteronuclear Hamiltonian:

$$H = H_{ZS} + H_{IS} + H_{ZI} \tag{6.2}$$

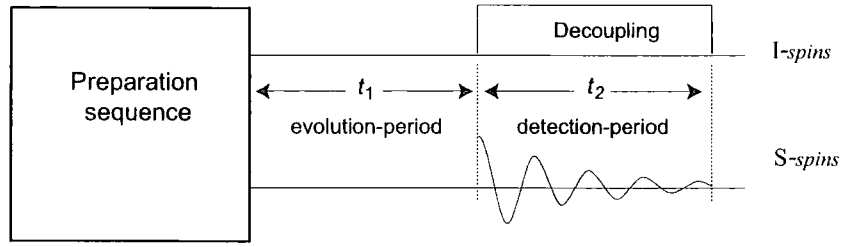

Figure 6.5 Simple scheme for the separation of *S* chemical shift and *IS* heteronuclear interactions. The preparation sequence serves to enhance S-spin polarisation. This can be achieved using, either heteronuclear polarisation transfer, or nuclear Overhauser effect (NOE) [13].

The term of Eq. (6.2), H_{ZS} and H_{ZI}, are the Zeeman interactions for the *S*-spins and *I*-spins while, H_{IS}, represents the *I*-*S* heteronuclear interactions. The explicit form of the heteronuclear Hamiltonian, H, is given by:

$$H = \delta_S I_Z^S - 2d_{IS} I_Z^S I_Z^I + \delta_I I_Z^I \tag{6.3}$$

Where δ_S and δ_I are the chemical shifts of *S* and *I* spins, while d_{IS} is the dipolar coupling.

In t_2-dimension (detection-period), a broadband decoupling is applied and so *I*-spins are decoupled. This implies that the *S*-signal evolves under an effective Hamiltonian, which is the *S*-spin term, H_{ZS}. In terms of the frequency domain, this corresponds to

multiplets, in ω_1-dimension. These multiplets are governed by the bilinear interactions H_{IS} and their barycentre are displaced by *S*-spin chemical shifts. In the ω_2-dimension the S-spin chemical shifts cause the separation of the various multiplets. It is worth nothing that, in some circumstances can be worthwhile to decouple during the evolution period, rather than in the detection one. This is because high resolution could not be necessary in *S*-shift dimension, while very high resolution can be required in the heteronuclear dimension.

In particular applications, such as in liquid crystals sample, an additional homonuclear decoupling between the abundant *I*-spins in t_1-dimension is applied. In this case the *S*-multiplet structure is only due to the *IS*-heteronuclear couplings without the influence of the homonuclear interactions.

6.3.2 Overview of 2D NMR

Before going into details of our 2D experiments, it is useful to give a brief description of how to obtain a doubly time-dependent NMR-signal $S(t_1,t_2)$ [14, 15]. As sketched in Figure 6.6, a 2D-experiment is divided in four distinct periods:

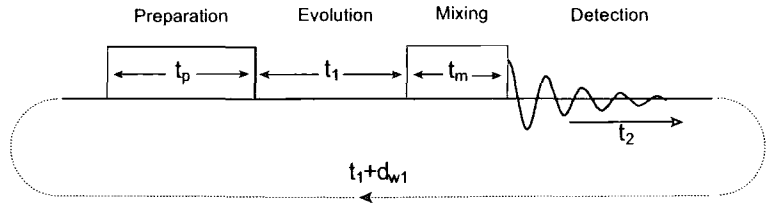

Figure 6.6 Schematic representation of 2D experiment. Four distinct intervals are shown: the preparation, t_p evolution period, t_1, mixing time, t_m and detection period, t_2. The two dimensional signal $S(t_1,t_2)$ is obtained by acquiring the FID in the t_2 -dimension as a function of the evolution period t_1 which is incremented by the dwell time d_{w1}

1. *The preparation period* t_p. This refers to the period immediately prior to t_1 evolution. This may be a single excitation pulse, techniques such as cross polarization to enhance the sensitivity of dilute spins with low γ, or excitation of multiple-quantum coherence, etc.

2. *The evolution period* t_1. Here the density matrix $\rho(\tau_p)$ evolves under a Hamiltonian $H^{(e)}$. This Hamiltonian can be modified by using, for instance, decoupling sequences, π-pulses to refocus the linear and heteronuclear interactions etc. In order to detect the resonances contained in the t_1-domain, a series of experiments are carried out increasing the evolution period at each experiment by the dwell time dw_1. The number of increments depends on both the strength of the Hamiltonian $H^{(e)}$, and the resolution we require. The combination of a high resolution with a good signal to noise ratio can be quite expensive in terms of spectrometer time, even for a nucleus with relatively short T_1.

3. *The mixing period* t_m. The nature of mixing period is highly variable, depending on the experiment involved. The length of the mixing period is usually held constant and during this time coupled spins exchange magnetization. The type of coupling that is observed in the spectrum depends on the experiment.

4. *The detection period* t_2. Here the final t_1-modulated NMR signal is acquired under the influence of the Hamiltonian $H^{(d)}$. As in the t_1-domain, this Hamiltonian can be modified e.g. by applying decoupling, sample spinning, etc.

The general form of 2D signal can be written:

$$S(t_1, t_2) = e^{i\tilde{\omega}_1 t_1} e^{i\tilde{\omega}_2 t_2} \tag{6.4}$$

where ω_1 and ω_2 are the oscillation frequencies of the signal in the t_1 and t_2 domains respectively. The evolution during the evolution period (t_1) is transferred into detection period as phase modulation of the t_2-signal. The double Fourier transform of the signal $S(t_1,t_2)$ gives the corresponding 2D-spectrum in the complex form:

$$\begin{aligned} F(\omega_1,\omega_2) &= FT_1\left[FT_2\left[S(t_1,t_2)\right]\right] = (A_1+iD_1)(A_2+iD_2) \\ &= (A_1A_2 - D_1D_2) + i(A_1D_2 + A_2D_1) \end{aligned} \tag{6.5}$$

Note how the real part of $F(\omega_1,\omega_2)$ contains a mixture of absorptive and dispersive components. Hence the 2D peaks have a "phase twist" lineshape, with a consequent loss of resolution compared to a pure absorption lineshape.

In order to obtain pure 2D absorption spectra we need to *amplitude* modulate the signal $S(t_1,t_2)$. Rewriting the signal of Eq. (6.4):

$$S(t_1,t_2) = (\cos\tilde{\omega}_1 t_1 + i\sin\tilde{\omega}_1 t_1)e^{i\tilde{\omega}_2 t_2} \tag{6.6}$$

we see that $S(t_1,t_2)$ can be considered in terms of two orthogonal components *cosine* and *sine* amplitude modulated signals:

$$\begin{aligned} S_C(t_1,t_2) &= \cos(\tilde{\omega}_1 t_1)e^{i\tilde{\omega}_2 t_2} \\ S_S(t_1,t_2) &= \sin(\tilde{\omega}_1 t_1)e^{i\tilde{\omega}_2 t_2} \end{aligned} \tag{6.7}$$

If we doubly Fourier transform the individual components S_C or S_S, we retrieve a pure absorption 2D-spectrum:

$$\begin{aligned} F_C &= \mathrm{Re}\left[FT_1\left[\mathrm{Re}\left[FT_2\left[\cos(\tilde{\omega}_1 t_1)e^{i\tilde{\omega}_2 t_2}\right]\right]\right]\right] \\ &= \frac{1}{2}\left[A_1(\tilde{\omega}_1) + A_1(-\tilde{\omega}_1)\right]A_2(\tilde{\omega}_2) \end{aligned} \tag{6.8}$$

for the S_S component we obtain a similar expression:

$$F_S = \frac{1}{2}\left[A_1(\tilde{\omega}_1) - A_1(-\tilde{\omega}_1)\right] A_2(\tilde{\omega}_2) \tag{6.9}$$

If the 2D-sequence provides the signal cosine or sine modulated we can obtain a pure absorption 2D-spectra. Using only one component, we cannot distinguish the sign of the frequencies. We can overcome this problem by hypercomplex acquisition, that is acquiring separately both S_C and S_S signals. Usually this is accomplished by change the phase of one or more RF-pulses in the sequence. Adding Fc and Fs gives a pure absorption line shape, with sign discrimination:

$$F_C + F_S = A_1(\tilde{\omega}_1) A_2(\tilde{\omega}_2) \tag{6.10}$$

6.4 SLF on ^{13}C-^{1}H-^{19}F spin system: basic sequences

We need to design a simple sequence to separate the C—F dipolar couplings from the carbon-13 chemical shifts. Since the heteronuclear separation is performed among three interacting nuclear spins (^{13}C, ^{19}F, ^{1}H), a triple channels sequence is required. As shown in Figure 6.7, two different schemes are possible:

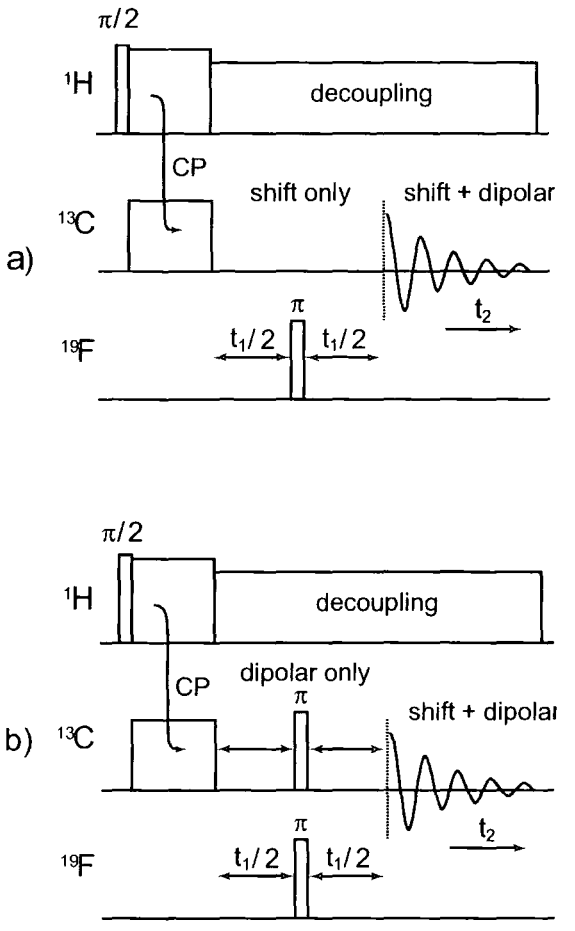

Figure 6.7 Schematic representation of two sequences to separate the C—F interactions from the ^{13}C chemical shifts. In both cases, the ^{13}C is cross-polarized and fully decoupled from the proton. a) In t_1-dimension, the C—F interactions are refocused by a ^{19}F π pulse applied in the middle of the evolution period, so that only the carbon chemical shift is preserved. In b), ^{19}F and ^{13}C π pulses are simultaneously applied in t1-dimesion, refocusing the ^{13}C shift evolution, while C—F interaction are left active.

In scheme (a), the t_2-signal is phase-modulated. This is because the ^{13}C density matrix, $\rho_C(0)$, after the cross-polarisation, evolves under an effective Hamiltonian given by the ^{13}C chemical shift. As a result, the magnetisation at the end of the evolution period contains both imaginary and real components i.e. is phase

modulated. In scheme (b), because the density matrix $\rho_C(0)$ is governed by an effective dipolar Hamiltonian, the t_1–signal is simply cosine (i.e. amplitude) modulated (see Eq.(6.7)).

6.5 The SLF experiment: preliminary results

The experiment has been carried out on a Varian InfinityPlus 500 MHz spectrometer. The sample used was I35 maintained in the nematic phase at the temperature of $40 \pm 0.1^{\circ}C$. The 2D ^{13}C spectrum was obtained by using a HFX triple channel probe with 4 mm coil, using the sequence given in Figure 6.7-b. One reason for this choice is that using scheme-a, the spectral width must be at least 50 kHz, due to the large range of the ^{13}C chemical shift resonances (~ 25 kHz). If we use scheme-b, because the biggest C—F dipolar coupling is around 4 kHz, the corresponding spectral width is reduced by an order of magnitude. Keeping the same resolution in both cases, the resulting experiment time is reduced by same factor.

The proton decoupling must be active over both the evolution and detection periods. This means that to achieve the same resolution as in 1D-spectra, the amount of the average RF power required is notably increased. So that to limit the effects related to an excess of decoupling power (arcing, heating the sample), it is necessary keep t_1 and t_2 as small as possible.

We tested the proton decoupling separately using SPINAL-64 (for details see Chapter 4). The best performance was found a tip angle of ~170° and shifting the ^1H-transmitter frequency of ~1 kHz away from a reference frequency, ν_{ref}, which is in this case 499.13 MHz. It is worth noting these are same optimal parameters as on 200 MHz spectrometer. Setting the decoupling power at 50 kHz (5us), and using 100 ms of acquisition time with the previous optimisation parameters, the best linewidth for the aliphatic carbons was ~20 Hz. By leaving the proton decoupler active for the same time as before (~100 ms), we set the maximum evolution period at ~42 ms and

the corresponding detection period at ~55 ms; with these settings, the resulting spectrum is slightly truncated in both dimensions. As we learned from 1D experiments on I35, the performance of the SPINAL64 degrades quite rapidly when the decoupling power is much less than 50 kHz. On the other hand, we also know that keeping high decoupling power for a long period (much greater 100 ms), apart the risk of arcing in the resonant circuit, causes problems in liquid crystals from RF heating. This is also why we did not use a more convenient scheme in which 19F decoupling is applied during t2. As previously explained this reduces spectral complexity, but the addition of the fluorine decoupling during the detection period would significantly increase the RF heating.

Simultaneous π-pulses are applied to the carbon and fluorine channels in t_1-domain. These pulses must be placed in the middle of the evolution period, and particular care has been taken in determining their exact position in order to start the acquisition on the t_2-dimension at the top of the echo (at t_1). If the t_1-echo is well calibrated, the t_2-signal is purely cosine amplitude modulated and the line shapes will be pure absorption. A shift of the t_2-aquisition from the top of the echo implies a non-perfect refocusing of the ^{13}C chemical shift interactions, resulting in a complicated mixture of phase and amplitude modulations. The resulting two-dimensional Fourier transformation will generate partially phase-twisted line shapes.

Imperfections of the π-pulses e.g. from RF inhomogeneity or off-resonance irradiation could also have a significant effect. In order to reduce those effects on the performance of π-pulses, an appropriate phase cycling on carbon π-pulse has been applied. No phase cycling was employed for the fluorine π-pulse. The proton decoupled fluorine spectrum of I35 in the nematic phase contains a single peak. By setting the fluorine transmitter on-resonance with this peak, the off-resonance effect on the π-pulse has been eliminated.

The performance of SLF experiment on I35 is shown in the figures below. Figure 6.8 includes an expansion of the 2D spectrum in the aromatic region, while Figure 6.9 displays an expansion of the aliphatic region.

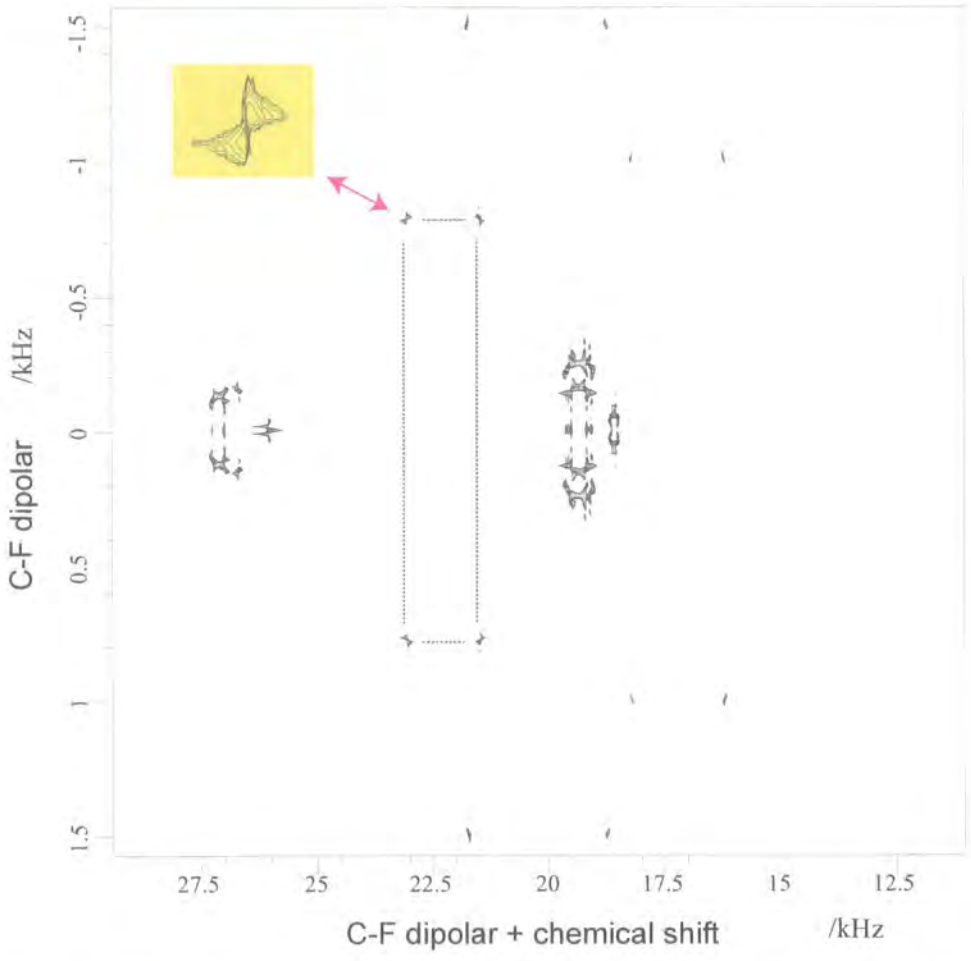

Figure 6.8 Separated-Local-Field experiment on I35 in the nematic phase, at 40° C. The figure shows an expansion of the aromatic region. The insert at the top shows the phase distortion of the 2D peaks. The data were acquired with 96 t_1 increments with 128 transients each. The data processing was performed by damping the FID with 15 Hz in the both dimensions and adding a zero filling of 4k points. To reduce the truncation in t_1-dimension the FID has been prolonged with 96 points using linear prediction. SPINAL-64 was optimised with a tip angle of 170° and ^{1}H-offset of 1 kHz. The decoupling power, 50 kHz and the pulse duration of π -pulses, 8 us and 9 us, respectively for ^{13}C and ^{19}F nuclei. The ^{13}C magnetisation was enhanced by proton cross-polarisation with a contact time of 3 ms, and the recycle delay 5 s.

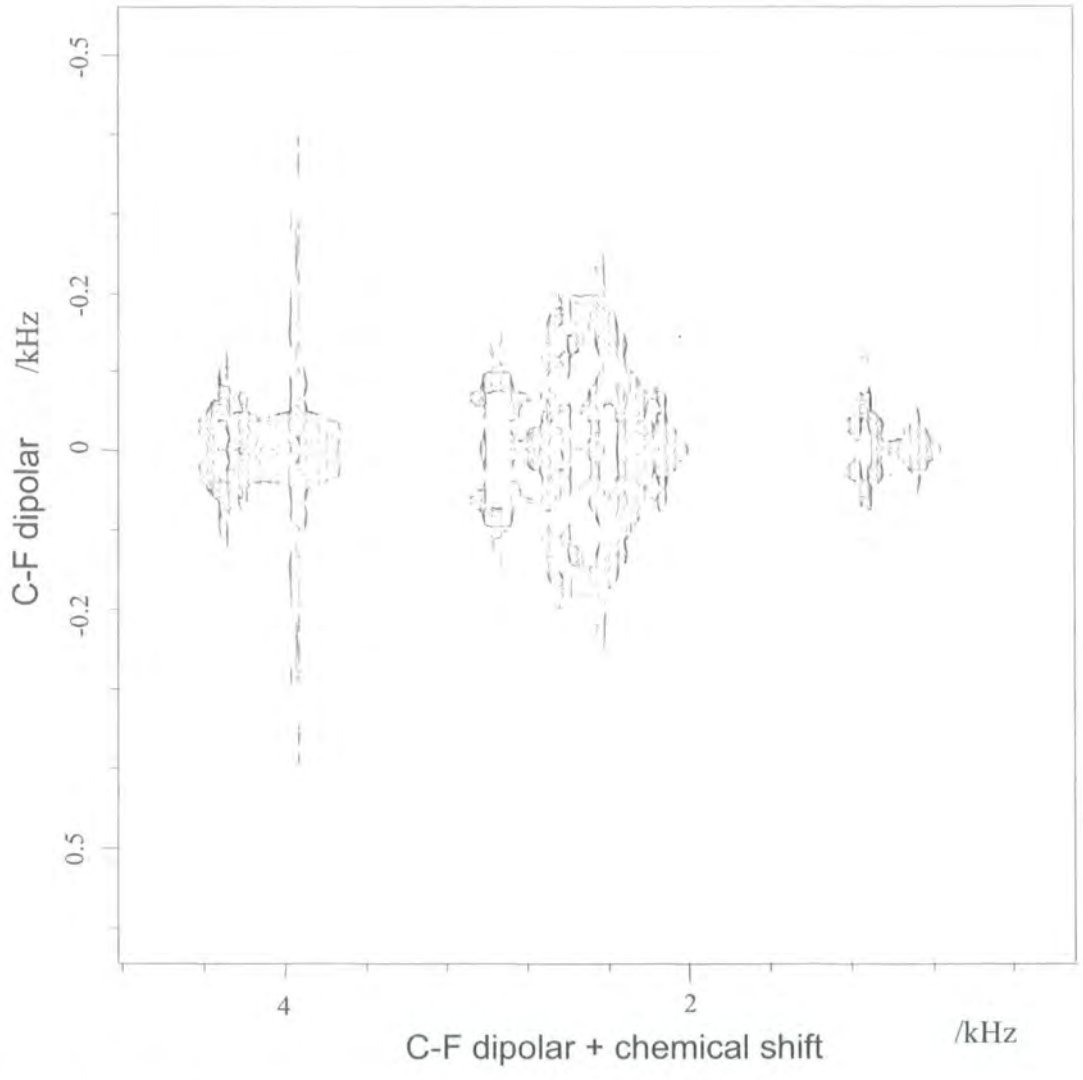

Figure 6.9 The Figure shows the corresponding expansion of the aliphatic region for I35.

6.6 Simulation of SLF experiment

In order to understand the experimental results, above shown, we simulated the SLF experiment according to the sequences illustrated in Figure 6.7.

The simulation is quite simple because the resulting SLF spectrum on I35 is given by a simple superposition of C—F splittings. This is because each ^{13}C is dipolar coupled to the single fluorine nucleus present in the molecule. In Figure 6.10 is sketched the simulation of SLF experiment for a C—F spin system according to the (b)-scheme, (Figure 6.7-b). The doubly time-dependent signal $S(t_1,t_2)$ has been obtained calculating the evolution of the carbon spin density matrix ρ_C:

$$\rho_C(0,0) = I_X^C \tag{6.11}$$

The evolution of the initial density matrix $\rho_C(0,0)$ in both time dimensions is simply given by the following expression:

$$\rho_C(n\Delta t_1, m\Delta t_2) = U_2(m\Delta t_2)U_1(n\Delta t_1)\rho_C(0,0)U_1^{\dagger}(n\Delta t_1)U_2^{\dagger}(m\Delta t_2) \tag{6.12}$$

The intervals, Δt_1, Δt_2 are the dwell times for the t_1 and t_2 dimensions, while n and m are variable integer numbers. The operators, U_1 and U_2 are the propagators for the t_1 and t_2 domains respectively:

$$U_1(n\Delta t_1) = e^{-iH_{dip}n\Delta t_1} \quad \text{and} \quad U_2(mt_2) = e^{-i(H_{dip}+H_{csa})mt_2} \tag{6.13}$$

where H_{dip} is the dipolar Hamiltonian and H_{csa} the chemical shift Hamiltonians. By calculating the trace of the product of the detection operator S_+ with the density operator given in Eq. (6.12), we obtain the carbon signal $S(n\Delta t_1, m\Delta t_2)$:

$$S(n\Delta t_1, m\Delta t_2) = Tr\{\rho_C(n\Delta t_1, m\Delta t_2)S_+\} \tag{6.14}$$

For each value of the number n by varying m within its entire range, the full signal in the t_2-dimension is calculated. In this way we build up a $N \times M$ complex matrix that

followed by the double Fourier transform (as shown in Eq.(6.8)) gives the absorption 2D-spectrum. Figure 6.10 shows the simulation of the experiment according to (b)-scheme (Figure 6.7). This simulation reproduces the peak distortion as experimentally observed (see Figure 6.8).

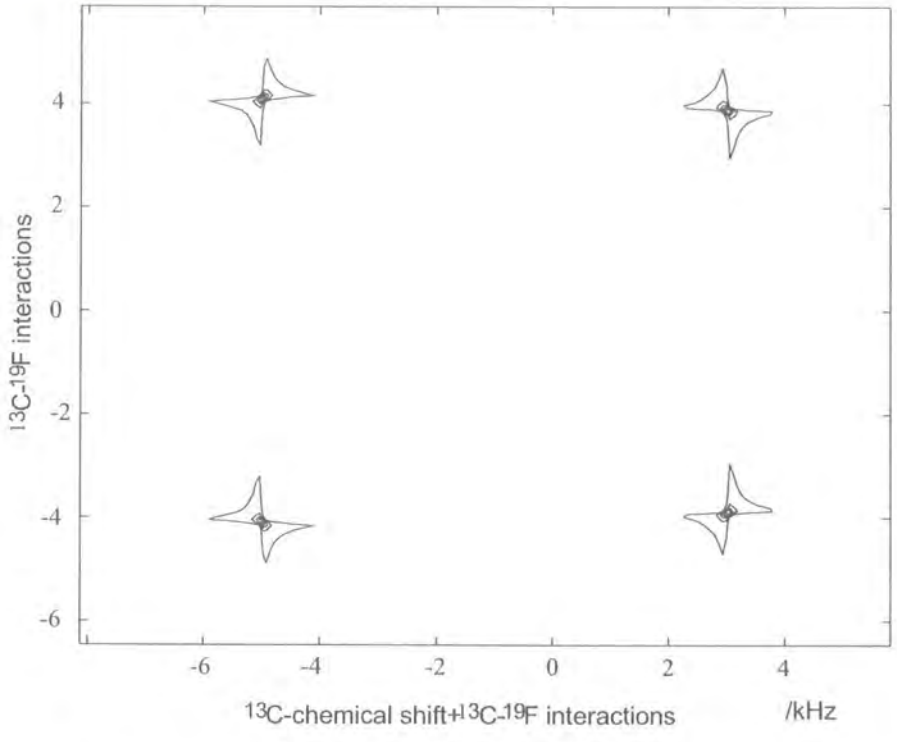

Figure 6.10 Simulation of the SLF experiment relatively to (b)-scheme. The simulation was performed in a C—F spin system with the following parameters: d_{CF} , 4 kHz, δ_C , 1 kHz . The phase distortion observed in the corresponding experiment is here well reproduced.

The lineshape distortion is caused by the effective spin interactions not completely separated in the two different time domains (t_1,t_2). Adding in SLF (b)-scheme ^{19}F decoupling during the acquisition time we obtain the complete separation of the interactions; in the t_1 domain the evolution is due to the C—F dipolar coupling, while in the t_2 domain only by the ^{13}C chemical shift. The simulation according to this

scheme is given in Figure 6.11, and as we can see the peak distortion has been entirely removed.

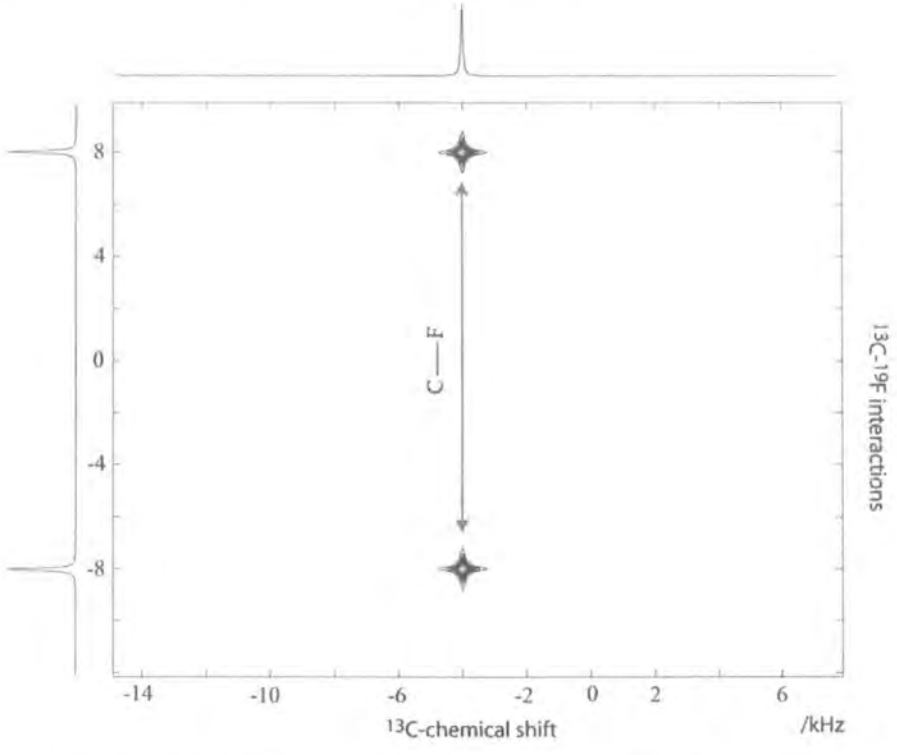

Figure 6.11 Simulation of SLF experiment based on the scheme-b but with ^{19}F decoupling during the detection period (t_2-dimesion). In this case the separation is C—F dipolar interaction *vs.* ^{13}C chemical shift. Since the interactions are cleanly separated, the peak distortion are now completely eliminate. The parameters of the simulation are: d_{CF}, 8 kHz, δ_C, - 4 kHz.

Moreover this scheme has the advantage of halving the number of peaks with respect to (b)-scheme (Figure 6.10). The resulting spectra could be better resolved for close peaks belonging to different doublets. The drawback in using this SLF sequence could be due to the RF heating effects, which are crucial in order to obtain high resolved spectra in liquid crystal samples. However we can avoid the decoupling in the ^{19}F channel modifying the (b)-scheme (Figure 6.7). The observed peak-shape

distortion employing can be eliminated by adding a 90° pulse on ^{13}C channel at the end of the evolution time t_1, as represented in Figure 6.12.

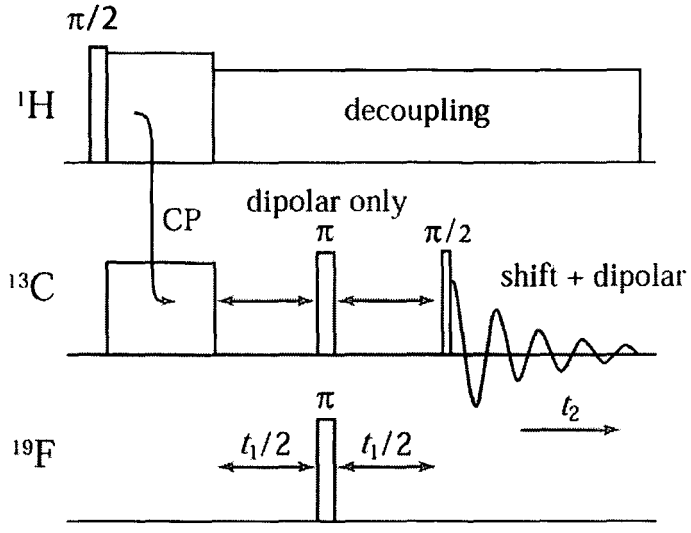

Figure 6.12 Schematic representation of SLF experiment based on the (b)-scheme (see Figure 6.7) with an additional 90° pulse on ^{13}C channel at the end of t_1-period.

The idea of adding a 90° pulse on ^{13}C stems from the density matrix calculation following the (b)-scheme. According to this scheme the ^{13}C signal in the t_1-dimension evolves by only C—F dipolar Hamiltonian, so that the initial density matrix $\rho_C(0) = I_x^C$ at time t_1 becomes:

$$\rho_C(t_1) = \exp(i2d_{CF}I_x^C t_1)I_x^C \exp(-i2d_{CF}I_x^C t_1) = I_x^C \cos(d_{CF}t_1) + \underline{I_y^C 2I_z^F \sin(d_{CF}t_1)} \tag{6.15}$$

The underlined term in Eq. (6.15) causes the peak distortion above observed. This would be clearer from an explicit density matrix calculation [16], however the peak distortion is caused by the time evolution of this term under dipolar Hamiltonian in the t_2-dimension. Applying at the end of t_1 period a $(90°)_x$ on carbon the density matrix becomes:

$$\tilde{\rho}(t_1) = U_{\pi/2}\rho(t_1)U_{\pi/2}^{\dagger} = \cos(d_{CF}t_1)I_x^C \underline{-2I_z^C I_z^F \sin(d_{CF}t_1)} \qquad (6.16)$$

Where $U_{\pi/2}$ is the propagator associated to the 90° pulse [17]. As it will be seen only the underlined term is affected by 90° pulse, which now commutes with the dipolar and chemical shift interactions. As a result this term is not evolving in t_2-dimension and the peak distortion should be eliminated. Simulations of SLF experiment according to the modified (b)-scheme (see Figure 6.12) confirm these theoretical results. Figure 6.13 shows the simulation results.

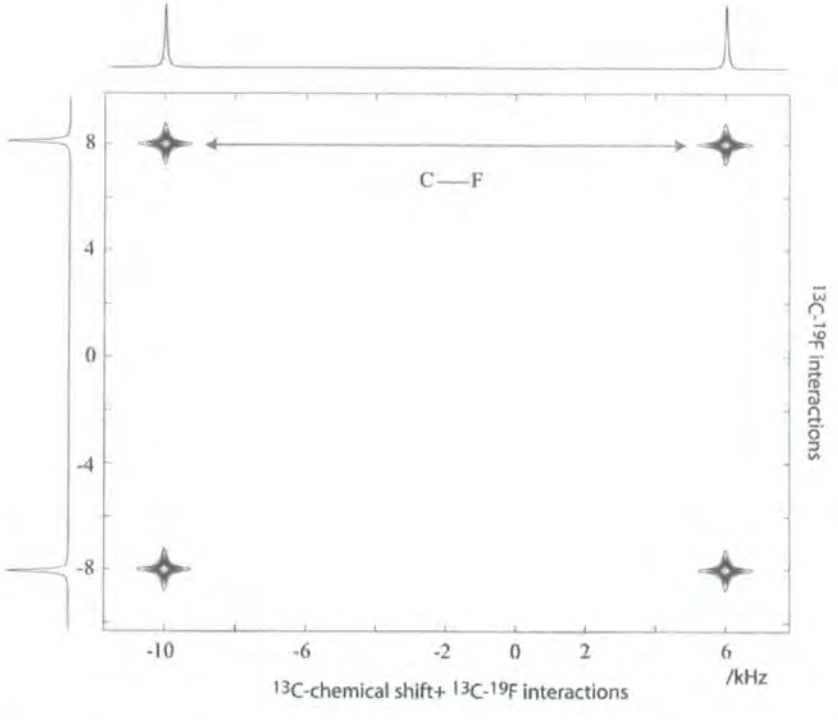

Figure 6.13 Simulation of SLF experiment according to the sequence of Figure 6.12. The additional 90° on ^{13}C at the end of t_1-period effectively removes the peak distortion. The simulation has been performed in a C—F spin system with the following simulation parameters: d_{CF}, 8 kHz, δ_C, -2 kHz.

6.7 SLF experiment with the modified (b)-scheme

The experiment has been carried out under the same condition as the previous experiment. The only difference between these two experiments is the presence of an additional 90° pulse on carbon (see Figure 6.12). As it will be seen in Figure 6.14 the theoretical predictions shown above are confirmed by the experiment.

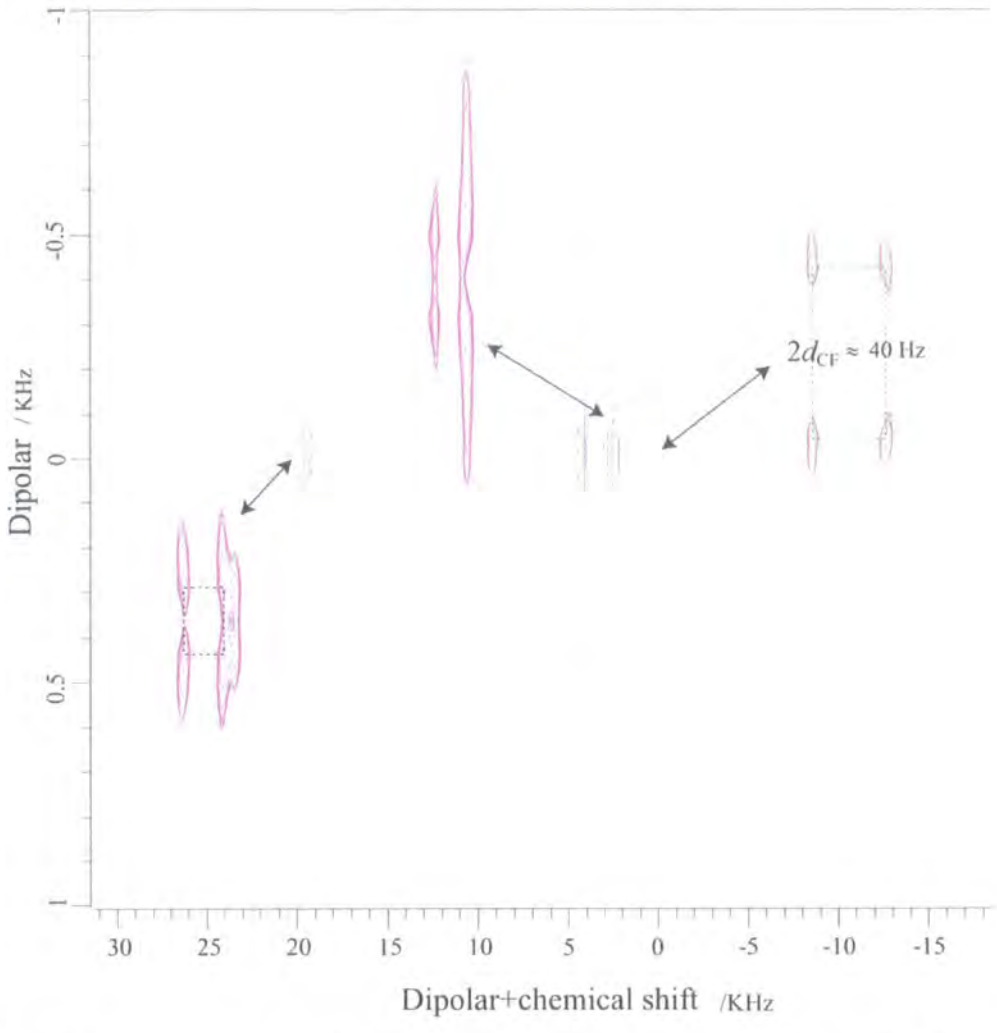

Figure 6.14 Separated-Local-Field experiment according to the scheme of Figure 6.12. The experiment was performed on I35 in the nematic phase, at 40° C. The inserts in the figure show pure absorption 2D-peaks of C—F doublets. The experimental parameters were the same as in the previously experiments; only the spectral width in t_1-dimension was reduced from 3 kHz to 2kHz.

6.8 Discussion and conclusion

Off-resonance experiment has not demonstrated to be a useful method for the assignment of C—F doublets. The major problems encountered in this experiments was the peak overlapping, even in a relatively small molecule such as I35. To overcome this problem we resorted to 2D-NMR methods using the SLF experiment. Although this experiment can be useful as a tool for the doublet assignment it can also give more accurate measurement of C—F dipolar couplings.

SLF spectra of Figure 6.8 and Figure 6.9 are relatively poorly resolved. One of the reasons of this is that the FID is truncated in both dimensions, particularly in t_1-dimension. The aromatic spectrum is much better resolved than the crowded aliphatic spectrum, but as seen in the yellow insert of Figure 6.8, the individual peaks are affected by a severe peak-shape distortion. Through the theoretical analysis and numerical simulation we found that these peak-shape distortion were caused by a not complete separation of the interactions in both dimensions (t_1, t_2). This is clearly demonstrated through the simulation of SLF experiment in which the t_1-period is governed by the dipolar Hamiltonian and the evolution period t_2 by the chemical shift Hamiltonian. The resulting spectra are pure absorption 2D-spectra. This SLF scheme has the advantage of halving the number of peaks with respect to (b)-scheme, however the drawback is that it requires ^{19}F and ^{1}H decoupling during the acquisition time, which can lead to the heating of the sample.

However ^{19}F decoupling can be avoided just adopting the modified (b)-scheme (see Figure 6.12). The experimental results shown in Figure 6.14 demonstrate that the peak-shape distortion can be eliminated, even if the interactions in both are not entirely separated. Figure 6.14 shows the smallest C—F splitting observed of about ~40 Hz, however with carefully optimisation of the experimental parameters even better resolution can be achieved. This optimisation regards an optimum combination of the total time $t_1 + t_2$ the decoupler power and recycle delay in order to achieve good decoupling without broadening the lines because of sample heating. This is

vital in order to resolve long-range dipolar splittings. The presence of π-pulse on carbon in the middle point of t_1-period has the advantage of refocusing effects from inhomogeneity of the static magnetic field, on the other side effects from pulse imperfection can lead to phasing problems and corresponding loss of resolution. For example off-resonance ^{13}C π-pulse produce a non-perfect spin population inversion ($I_Z \overset{\pi}{\rightarrow} -I_Z$), [18] giving rise to a non-perfect refocusing of ^{13}C chemical shift, which results in a 2D-signal with amplitude and phase modulations. Fortunately appropriate phase cycling is usually able to minimize or even eliminate such effects. Summarizing we can say that Off-resonance decoupling cannot substitute VASS method to assign C—F doublets. We have shown that SLF experiment works and potentially can be applied for assignment and accurate quantification of C—F doublets. Form the results here shown it is clear that further experimental optimisation is necessary and probably aliphatic and aromatic carbon splitting need to be resolved in two separated experiments.

References

1. E. Ciampi *et al.*, *Liquid Crystals* **26**, 109-125 (1999).
2. J. Courtieu, J. P. Bayle, B. M. Fung, *Progress in NMR Spectroscopy* **26**, 141-169 (1994).
3. B. C. Gerstein, C. R. Dybowski: Transient techniques in NMR of solids, *Academic Press INC* (1985.
4. R. R. Ernest, G. Bodenhausen, A. Wokaun: Principles of Nuclear Magnetic Resonance in one and two dimensions, *Oxford University Press, London* (1987), pp. 234-236.
5. B. M. Fung, A. K. Khitrin, K. Ermolaev, *J. Mag. Res.* **143**, 97-101 (2000).
6. W. A. Anderson, R. Freeman, *J. Chem. Phys.* **37**, 85 (1962).
7. C. P. Slichter: Principles of Magnetic Resonance, *Springer-Verlag Berlin Heidelberg New York*, (1989), pp. 29-30.
8. M. Mehring, V.A.Weberruβ: Object-Oriented Magnetic Resonance *Academic Press INC* (2001), pp. 405-408.
9. A. Ramamoorthy, C. H. Wu, S. J. Opella, *J. Mag. Res.* **140**, 131-140 (1999).
10. B. S. A. Kumar, S. J. Opella, *J. Mag. Res.* **101**, 333-336 (1993).
11. E. F. Rybaczewski, B. L. Neff, J. S. Waugh, J. S. Sherfinski, *J. Chem. Phys.* **67 (3)**, 1231-1236 (1977).
12. V. W. Miner, P. M. Tyrrel, and, J. H. Prestegard, *J. of Magn Res* **55**, 438-452 (1983).
13. C. P. Slichter: Principles of Magnetic Resonance, *Springer-Verlag Berlin Heidelberg New York*, (1989), pp. 254-264.
14. A. Bax: Two Dimensional Nuclear Magnetic Resonance in Liquids, *Reidel, Boston* (1982).
15. K. Schmidt-Rohr, H. W. Spiess: Multidimensional Solid-State NMR and Polymers, *Academic Press, London* (1994), Chapter 6.
16. J. P. Grivet, *J. Mag. Res.* **62**, 269-283 (1985).
17. M. H. Levitt: Spin Dynamics, *John Wiley* (2001), Chapter 12.
18. M. H. Levitt, *Progress in NMR Spectroscopy* **18**, 61-122 (1986).

Appendix

2-spin system with spin bath

This function calculates the NMR signal for 2-spins system interacting with spin bath. The spin diffusion superoperator given in Chapter 5 describes the spin bath.

(*This program is written in* MATLAB, *Version 6.1.0.450 Release 12.1*)

```
clear all
dosym=0;
dosub=1;

if dosym~=0
    syms d k dt
else
    d=250;
    k=570;
    dt=1/2000;
end

sys=[1/2 1/2];
NC=1;
NH=2;
Nobs=NC;

Hdip= d*S(sys,1,'z')*S(sys,2,'z');%Spin Hamiltonian
rho0=S(sys,Nobs,'+');

sigma0flat=reshape(rho0,16,1);

id=eye(4);
Hsuper= kron( Hdip,id) - kron(id,Hdip.');

R=k*(doublecom(S(sys,NH,'x'))+doublecom(S(sys,NH,'y'))+
doublecom(S(sys,NH,'z')));

L=-2*pi*i*Hsuper-R;

if dosym==0
    whichnz=find(abs(sigma0flat)>1e-2);
else
    if Nobs==NH
        whichnz=[5 15];
    else
        whichnz=[9 14];
    end
end
```

```
if dosub~=0
    sigma0flat=sigma0flat(whichnz);
    L=L(whichnz,whichnz);
end

[V,D]=eig(L);
E=exp(diag(D)*dt);

freqs=log(E)/(-2*pi*i*dt);

rho0t=inv(V)*sigma0flat;
detflat=sigma0flat.';
dett=detflat*V;
A0=dett.' .* rho0t;

if dosym~=0
    stop;
end

cycles=4096*2.0; % number of observations

signal=zeros(1,cycles);

sigma=sigma0flat;
A=A0;
for j=1:cycles
    signal(j)=sum(A);
    A=A .* E;
end

tscale=[0:cycles-1]*dt*1e3;
%plot(tscale,real(signal));

%axis([0 tscale(cycles) 0 2.2]);
xlabel('time / ms');

whichn=find(abs(A0)>1e-2);
disp('Dominant eigenvalues');
disp([ whichn A0(whichn) freqs(whichn)]);

signal(1)=1/2.0*signal(1);
sw1=1/dt;
f1=[0:cycles-1]*sw1/cycles-sw1/2;
spec=real(fftshift(fft(signal)));
figure(1)
plot(f1,spec,'r')
%axis([-500 500 0 25])
hold on


y = [f1; spec];
fid = fopen('exp.txt','w');
```

```
fprintf(fid,'%6.2f %12.8f\n',y);
fclose(fid)
```

Calculation of the propagator U for a 6-spin system

This function calculates the S-spectrum for a SI_5 spin system with different decoupling schemes. The total propagator U_T at the end of the cycle time τ is calculated by the cumulative time ordered product of individual propagators $U_k = e^{-iH_k\tau_k}$.

(*This program is written in* MATLAB, *Version 6.1.0.450 Release 12.1*)

```
Clear all
csH1=2.0e3;                              %Coupling constants
csH2=2.0e3;
csH3=6.0e3;
csH4=3.0e3;

dH1F=4.0e3;
dH2F=5.0e3;
dH3F=5.0e3;
dH4F=4.0e3;

dCH1=1.5e3;
dCH2=2.0e3;
dCH3=3.0e3;
dCH4=2.2e3;

dCF=3.0e3;

dH1H2=6.0e3;
dH1H3=5.0e3;
dH1H4=5.0e3;
dH2H3=6.0e3;
dH2H4=4.0e3;
dH3H4=5.0e3;

Wrf=50e3;                                % Strength of decoupling
                                         % field
sys=[1/2,1/2,1/2,1/2,1/2,1/2,1/2];       % spin system

Ihx1=s(sys,1,'x');                       % Spin operators
Ihy1=s(sys,1,'y');
Ihz1=s(sys,1,'z');

Ihx2=s(sys,2,'x');
Ihy2=s(sys,2,'y');
Ihz2=s(sys,2,'z');

Ihx3=s(sys,3,'x');
```

```
Ihy3=s(sys,3,'y');
Ihz3=s(sys,3,'z');

Ihx4=s(sys,4,'x');
Ihy4=s(sys,4,'y');
Ihz4=s(sys,4,'z');

Icx5=s(sys,5,'x');
Icy5=s(sys,5,'y');
Icz5=s(sys,5,'z');

Ifx6=s(sys,6,'x');
Ify6=s(sys,6,'y');
Ifz6=s(sys,6,'z');

Cplus=s(sys,5,'+');                    %Detection operator

sequence='cw';


switch(sequence)

case 'cw'
    seq=[0];

case 'tppm'
    seq=(pi/180)*[-10,10];

case 'sparc16'
    fi=(pi/180)*[10];
    fin=(pi/180)*[-10];

seq=[fi,fin,fin,fi,fin,fi,fi,fin,fi,fi,fin,fi,fin,fin,fi,fin]
;

case 'spinal64'
    fi=(pi/180)*[10,-10,15,-15,20,-20,15,-15];
    fin=(pi/180)*[-10,10,-15,15,-20,20,-15,15];
    seq=[fi,fin,fin,fi,fin,fi,fi,fin];


case 'spinal128'
    fi=(pi/180)*[10,-10,15,-15,20,-20,15,-15];
    fin=(pi/180)*[-10,10,-15,15,-20,20,-15,15];

seq=[fi,fin,fin,fi,fin,fi,fi,fin,fi,fi,fin,fi,fin,fin,fi,fin]
;
otherwise
end

tipangle=(175/180)*pi;                 %tip angle
steptip=tipangle/(2*pi*Wrf);           %pulse duration
```

```
numsamp=2048;                                   %number of sampling
                                                %points
numsubint=2;                                    %number sub-interval
numsupint=1;                                    %number sup-interval

if numsupint==1 & numsubint>1
    numcyc=numsamp/(numsubint*length(seq));
    dt=steptip/numsubint;
end

if numsubint==1 & numsupint>=1
    numcyc=numsamp*numsupint/length(seq);
    dt=steptip*numsubint;
end



if numcyc<1
    disp('error:numcyc<1')
    break
end

if numsupint>1 & numsubint>1
    disp('error:if numsupint>1==>numsubint=1')
    break
end

FID=zeros(1,numsamp);

Hchf=Icz5*[-2*dCH1*Ihz1-2*dCH2*Ihz2-2*dCH3*Ihz3-2*dCH4*Ihz4-
2*dCF*Ifz6]+...
Ifz6*[-2*dH1F*Ihz1-2*dH2F*Ihz2-2*dH3F*Ihz3-2*dH4F*Ihz4];

Hii=dH1H2*(2*Ihz1*Ihz2-Ihx1*Ihx2-
Ihy1*Ihy2)+dH1H3*(2*Ihz1*Ihz3-Ihx1*Ihx3-Ihy1*Ihy3)+...
    dH1H4*(2*Ihz1*Ihz4-Ihx1*Ihx4-
Ihy1*Ihy4)+dH2H3*(2*Ihz2*Ihz3-Ihx2*Ihx3-Ihy2*Ihy3)+...
    dH2H4*(2*Ihz2*Ihz4-Ihx2*Ihx4-
Ihy2*Ihy4)+dH3H4*(2*Ihz3*Ihz4-Ihx3*Ihx4-Ihy3*Ihy4);


Hsys=csH1*Ihz1+csH2*Ihz2+csH3*Ihz3+csH4*Ihz4+Hchf+Hii;

subcount=1;
supcount=1;

sigma=Icx5;                         %Initial density matrix

for u=1:numcyc
    for v=1:length(seq)
```

```
Hrf=(Ihx  Ihx  Ihx  Ihx    rf    (   (    (Ih   Ih   Ih   Ih
    rf    (   (
        H =Hrf H
        f r  =
             f          ==
                 I (         = r   (

             f
                 f           ==                    ==
                     I (          = r   (
                           =
                           =


             = x  (         H
                  =
                     =
```

```
 f
       =                                  spectral width
    dw1=1/sw1;
else
    sw1=1/(numsupint*dt);
    dw1=1/sw1;
end

timestep=0:dt:(numsamp-1)*dt;
dampt=numsamp*dw1/4;                      %line broadening
f1=[0:numsamp-1]*sw1/numsamp-sw1/2;
FID=FID.*exp(-timestep/dampt);
spec=fft(FID);
realspec=real(fftshift(spec));

hold on
subplot(2,1,1)
plot(f1,normrealspec)

axis([-20e3 20e3 0 1])
text(5e3,0.6,{'cw'})
subplot(212)
plot(f1,realspec,'k')
```

Calculation of the second moment M_2

This function calculates the second moment M_2 of S-spectra in a SI_2 spin system with various I-decoupling schemes. Both dipolar couplings d_{IS} and I-offset have been arrayed.

(*This program is written in* MATLAB, *Version 6.1.0.450 Release 12.1*)

```
max_off=6e3;
off_steps=18;
offsets=-maxoff+[0:off_steps-1]*(2*maxoff/(off_steps-1));

max_dCH=4e3;
dCH_steps=10;
array_dCH=[1:dCH_steps]*max_dCH/dCH_steps;

matrix_M2=zeros(dCH_steps,off_steps);

for m=1:dCH_steps
    for k=1:off_steps
        [M2,f1,period]=dechhalfbet(offsets(k),array_dCH(m));
        matrix_M2(m,k)=M2;
    end
end
[C,h]=contour(offsets,array_dCH, matrix_M2)
clabel(C,h);


function [M2,spec,f1,period]=dechhalfbet(off,dCH)

onlymain=0;         % Selection of the principal transitions
dH1H2=18e3;
dCH1=dCH;
dCH2=dCH;
csH1=1.0e3;
csH2=-3.0e3;
cs13C=0e3;

wrf=50e3;

numbersampling=1024;
tip_angle=(170/180)*pi;              %Nutation angle

if wrf
    step=tip_angle/(2*pi*wrf);
else
    step=100e-5;
end

B=zeros(4,4);
```

```
sys=[1/2,1/2];

Ix1=s(sys,1,'x');                    %Spin operators
Iy1=s(sys,1,'y');
Iz1=s(sys,1,'z');

Ix2=s(sys,2,'x');
Iy2=s(sys,2,'y');
Iz2=s(sys,2,'z');


FID=zeros(1,numbersampling);

sequence='spinal64';


switch(sequence)

case 'cw'
    seq=[0];

case 'tppm'
    seq=(pi/180)*[-10,10];

case 'sparc16'
    fi=(pi/180)*[10];
    fin=(pi/180)*[-10];

seq=[fi,fin,fin,fi,fin,fi,fi,fin,fi,fi,fin,fi,fin,fin,fi,fin]
;
case 'comp_pulse'
    fi=(pi/180)*[0 180 90 270 90 180 0];
    seq=fi;
    step_seq=[336 246 10 74 10 246 336]*(1/360)*(1/wrf);

case 'spinal64'
    fi=(pi/180)*[10,-10,15,-15,20,-20,15,-15];
    fin=(pi/180)*[-10,10,-15,15,-20,20,-15,15];
    seq=[fi,fin,fin,fi,fin,fi,fi,fin];

case 'spinal128'
    fi=(pi/180)*[10,-10,15,-15,20,-20,15,-15];
    fin=(pi/180)*[-10,10,-15,15,-20,20,-15,15];

seq=[fi,fin,fin,fi,fin,fi,fi,fin,fi,fi,fin,fi,fin,fin,fi,fin]
;
otherwise
end


if strcmp(sequence,'comp_pulse')
    step=sum(step_seq);
```

```
    period=step;
    freq=1/period;
else
    period=length(seq)*step;
    freq=1/period;
end


Up=eye(4);
Um=eye(4);
ide=eye(4);

%Spin Hamiltonian
Hsysp=0.5*ide*cs13C+(dCH1+csH1+off)*Iz1+(csH2+dCH2+off)*Iz2-
dH1H2*(2*Iz1*Iz2-Ix1*Ix2-Iy1*Iy2);
Hsysm=-0.5*ide*cs13C+(-dCH1+csH1+off)*Iz1+(-
dCH2+csH2+off)*Iz2-dH1H2*(2*Iz1*Iz2-Ix1*Ix2-Iy1*Iy2);

for j=1:length(seq)

Hrf=(Ix1+Ix2)*(wrf*cos(seq(j)))+(Iy1+Iy2)*(wrf*sin(seq(j)));

    if strcmp(sequence,'comp_pulse')
        step=step_seq(j);
    end
    Hp=Hrf+Hsysp;
    Up=expm(-2*pi*i*Hp*step)*Up;
    Hm=Hrf+Hsysm;
    Um=expm(-2*pi*i*Hm*step)*Um;
end


[Vp,Dp]=eig(Up);%Diagonalization of the Hamiltonian α or β
staes
[Vm,Dm]=eig(Um);%
lambdap=-angle(diag(Dp))*freq/(2*pi);
lambdam=-angle(diag(Dm))*freq/(2*pi);

V=Vp'*Vm;
A2=V.*conj(V);
M2=0;
for u=1:4
    for v=1:4
        diff=mod(lambdap(u)-lambdam(v),freq);
        if diff>freq/2
            diff=diff-freq;
        end
        f(u,v)=diff;
    end
end

for u=1:4
```

```
    if onlymain
        [maxv,maxi]=max(A2(u,:));
        M2=M2+A2(u,maxi)*f(u,maxi)^2;

    else
        for v=1:4
            M2=M2+A2(u,v)*f(u,v)^2;
        end
    end
end

for ss=1:numbersampling
    for u=1:4
        for v=1:4
            B(u,v)=A2(u,v)*exp(2*pi*f(u,v)*i*(ss-1)*step);
%period
        end
    end
    FID(ss)=(1/2)*sum(sum(B));
end

sw1=1/step;%bandwidth

dampt=numbersampling*step/4;
f1=[0:numbersampling-1]*sw1/numbersampling-sw1/2;
steps=0:step:(numbersampling-1)*step;
FID=FID.*exp(-2*pi*steps/dampt);
FFT1=fft(FID);
spec=real(fftshift(FFT1));
```

Calculation of the propagator for a 3-spin system under MAS

This function calculates the A-spectrum for A —X—Y spin system with various X decoupling schemes under MAS.

(*This program is written in* C++)

```
#include "NMR.h"
#include "ListList.h"
#include "matlabio.h"
#include "powder.h"
#include "space_T.h"
#include "ttyio.h"
#include "spin_system.h"

using namespace std;
using namespace libcmatrix;
```

```
const double deg_to_rad=M_PI/180.0;
int main(int argc, const char *argv[])
{
int count=1;
spin_system sys(1);
// sys(0).isotope("13C");
sys(0).isotope("1H");
// sys(1).isotope("19F");


double csHiso=-4e3;            //Input parameters
double csHan=2.0e3;
double cs13C=0.0e3;
double cs13Can=0.0e3;
double dCH=2e3;
double dHF=5.0e3;
double dCF=4e3;
double JCF=-25;
double JCH=160;


double vR;                  //spinning speed
double vrf=50.0e3;          //decoupling power
double sw=25e3;
int numsampling=2048;       //number data points
double dwell=1/sw;          //dwell-time

int gammasteps=5;           //number gamma steps
double gamma=2*M_PI;
double d_gamma=gamma/gammasteps;  //gamma steps
vR=getfloat(argc,argv,count," spin_rate[Hz]:",0.0);
if(vR==0) {
gammasteps=1;
}

List<complex> FIDtot(numsampling,0.0);
List<complex> FIDalpha(numsampling,0.0);
List<complex> FIDbeta(numsampling,0.0);


//const cmatrix ICz=F(sys,"13C",'z');
//const cmatrix IFz=F(sys,"19F",'z');
const cmatrix IHx=F(sys,"1H",'x');
const cmatrix IHy=F(sys,"1H",'y');
const cmatrix IHz=F(sys,"1H",'z');

cout<<"IHx:" << IHx <<endl;

//const cmatrix ICx=F(sys,"13C",'x');
//const cmatrix ICy=F(sys,"13C",'y');
//const cmatrix ICz=F(sys,"13C",'z');
```

```
//const cmatrix IFx=F(sys,"19F",'x');
//const cmatrix IFy=F(sys,"19F",'y');
//const cmatrix IFz=F(sys,"19F",'z');


// const cmatrix detect=F(sys,"13C",'+');

//input file name
char fname[128];
getstring(argc,argv,count,"Output file :",fname,128);

int pulses;
double tip_angle;

double phasediff=14.0*deg_to_rad; //TPPM phase angle angle

enum {CW, TPPM, SPINAL64};
cout<<"C - CW\nT - TPPM\nS - SPINAL64\n";
const size_t rfscheme=getoption(argc,argv,count,"RF
scheme:","CTS",CW);

//which RF scheme

switch(rfscheme){
case CW: pulses=1;
break;
case TPPM:
pulses=2;
tip_angle=(M_PI/180.0)*getfloat(argc,argv,count,"tipangle
:",165);
dwell=tip_angle/(2*M_PI*vrf);//pulse duration
break;
case SPINAL64:
pulses=64;
tip_angle=(M_PI/180.0)*getfloat(argc,argv,count,"tipangle
:",165);
dwell=tip_angle/(2*M_PI*vrf);//pulse duration
break;
}

List<double> phasevals(1,0.0);
List<size_t> indphases(pulses,size_t(0));//vedre come
funziona la size_t
const size_t Q[8]={0,1,2,3,4,5,2,3 };
const size_t Qbar[8]={1,0,3,2,5,4,3,2 };

switch(rfscheme){
case TPPM:
phasevals.create(2);
phasevals(0)= phasediff/2.0;
phasevals(1)= -phasediff/2.0;
```

```
indphases(0)= 0;
indphases(1)= 1;
break;
case SPINAL64:
phasevals.create(6);
phasevals(0)=  10.0;
phasevals(1)= -10.0;
phasevals(2)=  15.0;
phasevals(3)= -15.0;
phasevals(4)=  20.0;
phasevals(5)= -20.0;
phasevals*=  deg_to_rad;

indphases(slice(0,8)) = Q;
indphases(slice(8,8)) = Qbar;
indphases(slice(16,8))= Qbar;
indphases(slice(24,8))= Q;
indphases(slice(32,8))= Qbar;
indphases(slice(40,8))= Q;
indphases(slice(48,8))= Q;
indphases(slice(56,8))= Qbar;
break;
}
const double MAGIC_ANGLE=acos(1/sqrt(3));


//Angles for the system 13C bonded to the 19F and coupled to
the 1H
/* Euler PAS_csH_to_PASCH(0.0,0.0,0.0);
Euler PAS_HF_to_PASCH(0.0,32.2*deg_to_rad,0.0);
Euler PAS_CF_to_PASCH(0.0,93*deg_to_rad,0.0);*/

/*Angles for the system 13C bonded to the 19F and coupled to
the 1H
in the phenil group*/
Euler PAS_cs13C_to_PASCH(0.0,0.0,0.0);
Euler PAS_csH_to_PASCH(0.0,0.0,0.0);
Euler PAS_HF_to_PASCH(0.0,0.0*deg_to_rad,0.0);
Euler PAS_CF_to_PASCH(0.0,0.0,0.0);

//Angles to RF to LF

Euler RF_to_LF(0.0,MAGIC_ANGLE,0.0);
Euler PASCH_to_RF(0.0,0.0,0.0);

//Spatial tensor in the relative PAS
space_T CSA_13C_PAS=spatial_tensor(cs13Can);
space_T CSA_H_PAS=spatial_tensor(csHiso,csHan,0);
space_T dCH_PAS=spatial_tensor(dCH);
space_T dCF_PAS=spatial_tensor(dCF);
space_T dHF_PAS=spatial_tensor(dHF);
```

```
// cout<<"dHF_PAS:" << dHF_PAS <<endl;
cout<<"dwell:" << dwell <<'\t'<<"tipangle:"<< tip_angle
<<endl;

space_T dCF_PAS_to_dCH_PAS=rotate(dCF_PAS,PAS_CF_to_PASCH);
space_T dHF_PAS_to_dCH_PAS=rotate(dHF_PAS,PAS_HF_to_PASCH);
space_T
CSA_H_PAS_to_dCH_PAS=rotate(CSA_H_PAS,PAS_csH_to_PASCH);
space_T
CSA_13C_PAS_to_dCH_PAS=rotate(CSA_13C_PAS,PAS_cs13C_to_PASCH)
;

cmatrix Hrf;
Euler powder(0,0,0);
double weight;


PlanarZCW  powdmethod(12); //powder method
cout << "Orientations: " << powdmethod.orientations() <<
'\n';

double dCH_RF_LF;
double dCF_RF_LF;
double dHF_RF_LF;
double CSA_H_RF_LF;
double CSA_13C_RF_LF;
List<double> aphases=phasevals(indphases);
int size_seq=aphases.length();
int numcyc=numsampling/size_seq;
// cout<<"aphases:" << size_seq <<endl;

//Powder loop
cmatrix Hsys_falpha_p;
cmatrix Hsys_falpha_m;
cmatrix Hsys_fbeta_p;
cmatrix Hsys_fbeta_m;
cmatrix Ualpha_p, Ualpha_m;
cmatrix Ubeta_p, Ubeta_m;
cmatrix Ide;
Ide.identity(2);

while(powdmethod.next(powder,weight)) {

space_T  dCH_RF=rotate( dCH_PAS,powder);
space_T  dCF_RF=rotate(
dCF_PAS_to_dCH_PAS,powder);//controllare
space_T  dHF_RF=rotate( dHF_PAS_to_dCH_PAS,powder);
space_T  CSA_H_RF=rotate( CSA_H_PAS_to_dCH_PAS,powder);
space_T  CSA_13C_RF=rotate( CSA_13C_PAS_to_dCH_PAS,powder);
//cout<<"dCF_RF:" << dCF_RF <<endl;
//loop su tstep e poi su gamma
```

```
for(int gcount=0 ;gcount<gammasteps; gcount++) {
Ualpha_p=Ide;
Ualpha_m=Ide;
Ubeta_p=Ide;
Ubeta_m=Ide;
// cout<< "sigma0:" << sigma0 <<endl;
int fcount=0;
for(int u=0 ;u<numcyc; u++){
        for(int k=0 ;k<size_seq; k++) {
fcount=fcount+1;

Hrf=(vrf*cos(aphases(k)))*IHx+(vrf*sin(aphases(k)))*IHy;

if(vR==0) {
                        dCH_RF_LF=real(rotate(
dCH_PAS,2,0,powder));
                        dCF_RF_LF=real(rotate(
dCF_PAS,2,0,powder));
                        dHF_RF_LF=real(rotate(
dHF_PAS,2,0,powder));
                        CSA_H_RF_LF=real(rotate(
CSA_H_PAS,2,0,powder));
                        CSA_13C_RF_LF=real(rotate(
CSA_13C_PAS,2,0,powder));

}
else {

RF_to_LF.alpha=2*M_PI*vR*(fcount)*dwell+gcount*d_gamma;

dCH_RF_LF=real(rotate( dCH_RF,2,0, RF_to_LF));

dCF_RF_LF=real(rotate( dCF_RF,2,0, RF_to_LF));

HF_RF_LF=real(rotate( dHF_RF,2,0, RF_to_LF));

CSA_H_RF_LF=real(rotate( CSA_H_RF,2,0,RF_to_LF));
CSA_13C_RF_LF=real(rotate( CSA_13C_RF,2,0,RF_to_LF));
                    }
                    Hsys_falpha_p=(-JCF/4.0-dCF_RF_LF/2.0-
cs13C/2.0-CSA_13C_RF_LF/2.0)*Ide+
                    (csHiso+CSA_H_RF_LF-dHF_RF_LF-dCH_RF_LF-
JCH/2.0)*IHz+Hrf;


Hsys_falpha_m=(JCF/4.0+dCF_RF_LF/2.0+cs13C/2.0+CSA_13C_RF_LF/
2.0)*Ide+
                    (csHiso+CSA_H_RF_LF-
dHF_RF_LF+dCH_RF_LF+JCH/2.0)*IHz+Hrf;
```

```
                    Hsys_fbeta_p=(JCF/4.0+dCF_RF_LF/2.0-
cs13C/2.0-CSA_13C_RF_LF/2.0)*Ide+
                    (csHiso+CSA_H_RF_LF+dHF_RF_LF-dCH_RF_LF-
JCH/2.0)*IHz+Hrf;

                    Hsys_fbeta_m=(-JCF/4.0-
dCF_RF_LF/2.0+cs13C/2.0+CSA_13C_RF_LF/2.0)*Ide+

(csHiso+CSA_H_RF_LF+dHF_RF_LF+dCH_RF_LF+JCH/2.0)*IHz+Hrf;

                    // cout<<"aphases:" << aphases(k) << "seq
"<< size_seq <<endl;
                    // cout<< "Hrf:" << Hrf <<endl;

                    FIDalpha(fcount-
1)+=trace(Ualpha_p,conj_transpose(Ualpha_m))*weight;
                    FIDbeta(fcount-
1)+=trace(Ubeta_p,conj_transpose(Ubeta_m))*weight ;
                    FIDtot(fcount-1)=FIDalpha(fcount-
1)+FIDbeta(fcount-1);

                    Ualpha_p=
propagator(Hsys_falpha_p,dwell)*Ualpha_p;
                    Ualpha_m=
propagator(Hsys_falpha_m,dwell)*Ualpha_m;
                    Ubeta_p=
propagator(Hsys_fbeta_p,dwell)*Ubeta_p;
                    Ubeta_m=
propagator(Hsys_fbeta_m,dwell)*Ubeta_m;

// cout<<"H_falpha:" << S <<endl;
                }
            }

        }
    }
    //cout<<"powder:" << U  <<endl;
    WriteMATLAB(fname,FIDtot);
    return 0;
}
```

Simulation of Separate-Local-Field experiment

This function calculates the 2D-spectrum using SLF sequences given in Chapter 6

(*This program is written in* MATLAB, *Version 6.1.0.450 Release 12.1*)

```
cs=[1000 2000];          % Chemical shifts
d=[4000 2000];           % Dipolar couplings
npt1=256;                % Number sampling in t1
npt2=256;                % Number sampling in t2
```

```
sw1=20000;                % Spectral width in t1
sw2=20000;                % Spectral width in t2

dw1=1/sw1;
dw2=1/sw2;

t1=0:dw1:dw1*(npt1-1);      %t1 axis
t2=0:dw2:dw2*(npt2-1);      %t2 axis

dampt2=npt2*dw2/6;
dampt1=npt1*dw1/6;

Iz1=s([1/2,1/2],1,'z');     %Spin operators
Iz2=s([1/2,1/2],2,'z');
Ix1=s([1/2,1/2],1,'x');
Iy1=s([1/2,1/2],1,'y');

Iplus=s([1/2,1/2],1,'+');   %Detection operator

Fid=zeros(npt1,npt2);
theta=0.0;%pi/2.0;          %p/2 pulse on X-nucleus
Up=expm(i*Ix1*theta);


for nuc=1:2

    His=-2*d(nuc)*Iz1*Iz2;      %Dipolar Hamiltonian
    Hcs=cs(nuc)*Iz1;            %Chemical shift Hamiltonian

    Hev=His;                    %Hamiltonian during t1
    Hdec=His+Hcs;               %Hamiltonian during t2

    U1=expm(-2*pi*i*dw1*Hev);
    U2=expm(-2*pi*i*dw2*Hdec);


    sigt1=Ix1;                  %Initial density matrix
    resigt1=sigt1;

    for k=1:npt1
        %sigt2=sigt1;
        sigt2=resigt1;

        for j=1:npt2

            Fid(k,j)=Fid(k,j)+sum(sum(Iplus.*sigt2));
            sigt2=U2*sigt2*U2';

        end
        sigt1=U1*sigt1*U1';
        resigt1=Up*sigt1*Up';
```

```
    end
end

damp=exp(-t2/dampt2);

for k=1:npt1
    a=exp(-t1(k)/dampt1);
    Fid(k,:)=Fid(k,:) .* (a*damp);
end


%----------------------------------%
%         PROCESSING               %
%----------------------------------%
f1=[0:npt1-1]*sw1/npt1-sw1/2;
f2=[0:npt2-1]*sw2/npt2-sw2/2;

S_1_2=Fid;


    for k=1:npt1
        S_1_2(k,1)=S_1_2(k,1)/2.0;
        S1_FT2(k,:)=real(fftshift(fft(S_1_2(k,:))));

    end

    for j=1:npt2
        S1_FT2(1,j)= S1_FT2(1,j)/2.0;
        S_FT1_FT2(:,j)=real(fftshift(fft(S1_FT2(:,j))));

    end


%f1=[0:npt1-1]*sw1/npt1;
%f2=[0:npt2-1]*sw2/npt2;
%contour(f2,f1,ft2)
%plot(f1,sdi(10,:).')
%plot(t1,Fid(12,:))

%-------------plot--------------%
contour(f2,f1,S_FT1_FT2,10)
%surf1(f2,f1,sdfi)
title('SLF')
%shading interp
%colormap(cool);
%-------------plot--------------%
```

Acknowledgements

I would like to express my deep gratitude to Paul Hodgkinson, my supervisor, for his encouragements and support. Many thanks to R. K. Harris for his interesting questions and stimulating discussions. I would like to acknowledge J. W. Emsley for his help with Liquid Crystals and his hospitality.

A special thanks to my friends who shared with me NMR laboratory:

Alessia, Aom, Debbie, Diane, Ian, Mattew, Paolo, Paul, Philip, Phuong, Romain, Thomas and Veni.

Thanks to Giusy and Marco too to have made my time in Durham enjoyable.

A special thanks to my family for encouragements in all the period I've spent in England.